Pacific Northwest
NATIONAL LABORATORY

PNNL-37700

Mitigate Stress Corrosion Cracking (SCC) in High-strength Al Castings (CRADA 508) Final Report

April 2025

Matthew Olszta
Robert Seffens
Timothy Roosendaal
Karen Kruska
Gabrielle Schuler
Venkateshkumar Prabhakaran
Alan Schemer-Kohrn
Mayur Pole
David Weiss
Aashish Rohatgi

U.S. DEPARTMENT OF
ENERGY

Prepared for the U.S. Department of Energy
under Contract DE-AC05-76RL01830

DISCLAIMER

This report was prepared as an account of work sponsored by an agency of the United States Government. Neither the United States Government nor any agency thereof, nor Battelle Memorial Institute, nor any of their employees, makes **any warranty, express or implied, or assumes any legal liability or responsibility for the accuracy, completeness, or usefulness of any information, apparatus, product, or process disclosed, or represents that its use would not infringe privately owned rights**. Reference herein to any specific commercial product, process, or service by trade name, trademark, manufacturer, or otherwise does not necessarily constitute or imply its endorsement, recommendation, or favoring by the United States Government or any agency thereof, or Battelle Memorial Institute. The views and opinions of authors expressed herein do not necessarily state or reflect those of the United States Government or any agency thereof.

PACIFIC NORTHWEST NATIONAL LABORATORY
operated by
BATTELLE
for the
UNITED STATES DEPARTMENT OF ENERGY
under Contract DE-AC05-76RL01830

Printed in the United States of America

Available to DOE and DOE contractors from
the Office of Scientific and Technical Information,
P.O. Box 62, Oak Ridge, TN 37831-0062
www.osti.gov
ph: (865) 576-8401
fox: (865) 576-5728
email: reports@osti.gov

Available to the public from the National Technical Information Service
5301 Shawnee Rd., Alexandria, VA 22312
ph: (800) 553-NTIS (6847)
or (703) 605-6000
email: info@ntis.gov
Online ordering: http://www.ntis.gov

PNNL-37700

Mitigate Stress Corrosion Cracking (SCC) in High-strength Al Castings (CRADA 508) Final Report

April 2025

Matthew Olszta
Robert Seffens
Timothy Roosendaal
Karen Kruska
Gabrielle Schuler
Venkateshkumar Prabhakaran
Alan Schemer-Kohrn
Mayur Pole
David Weiss
Aashish Rohatgi

Prepared for
the U.S. Department of Energy
under Contract DE-AC05-76RL01830

Pacific Northwest National Laboratory
Richland, Washington 99354

Cooperative Research and Development Agreement (CRADA) Final Report

April 2025

In accordance with Requirements set forth in the terms of the CRADA, this document is the CRADA Final Report, including a list of Subject Inventions, to be provided to PNNL Information Release who will forward to the DOE Office of Scientific and Technical Information as part of the commitment to the public to demonstrate results of federally funded research.

Parties to the Agreement: Eck Industries and Pacific Northwest National Laboratory

CRADA number: **508**

CRADA Title: **Mitigate Stress Corrosion Cracking (SCC) in High-strength Al Castings**

Responsible Technical Contact at DOE Lab: Aashish Rohatgi

Name and Email Address of POC at Company: David Weiss, david.weiss@eckindustries.com

DOE Program Office: Vehicle Technologies Office

Joint Work Statement Funding Table showing DOE funding commitment:

Funding (USD)	**Project Year 1**	**Project Year 2**	**TOTALS**
Government			
DOE	250	250	500
Other	-	-	-
Total Govt.	250	250	500
Participant			
In-Kind	250	250	500
Funds-In	-	-	-
FAC			
Total Participant	250	250	500
TOTAL CRADA Value	500	500	1,000

Acknowledgments

The authors gratefully acknowledge support from Lightweight Materials Consortium (LightMAT), sponsored by the Vehicle Technologies Office, Office of Energy Efficiency and Renewable Energy, U.S. Department of Energy. The authors would like to acknowledge PNNL staff Drs. Rajib Kalsar and Julian Escobar Atehortua, for assistance with SECCM sample preparation during the initial stages of the project and review of this report, respectively.

Executive Summary

Development of high strength, corrosion resistant, aluminum alloys is important to a number of industries, including automotive, aerospace, power, etc. Understanding how processing methods such as casting, chemistry, additives and recycle content affect an alloy's microstructure and performance in real world environments is crucial to their implementation. One major concern is how the repeated exposure to saline solutions can be detrimental to the structural integrity of aluminum alloy components. This study was undertaken as a collaboration between Eck Industries and PNNL to investigate the stress corrosion cracking (SCC) and corrosion behavior of aluminum alloys.

This work examines the SCC response of three different materials set. First is cast A206 Al alloy produced by three different casting techniques (i.e., permanent mold, and sand casting with and without chill) and with or without nano forming additives as potential grain refiners. The second materials set comprises Al alloy tubes extruded by PNNL's ShAPE process and produced using raw material with three different ratios of twitch and pre-consumer Al 6061 scrap. Finally, the third materials set comprises two Al-Si-Mg-Fe alloys with controlled Si% and Fe% to mimic recycle grade Al alloys. The corrosion behavior of these materials was characterized using SCC testing and scanning electrochemical cell microscopy (SECCM) technique; mechanical behavior was characterized using tensile testing, and microstructure was characterized using optical and electron microscopy techniques.

Of the A206 Al alloys, the samples with nano forming additives performed poorly compared to those without. The best SCC performance (i.e. least degradation in mechanical properties) was demonstrated by A206 alloy sand cast with chill while the permanent mold sample showed the worst SCC performance. The SECCM was performed on A206 alloy sand cast with chill to understand the effect of microstructure and determine the location-dependent corrosion properties on grain boundaries (GB) and inside grains (IG) on the sample. The corrosion potential and current measured on GB and IG at various points on the sample established that the GB locations are more cathodic and corrosive than the IG locations. Further work needs to be conducted to investigate the mechanisms behind the observed dependence of SCC on casting technique and nano forming additives. Among the ShAPE extruded tubes, SECCM data suggests the decreasing order of tendency to corrode as follows: 100% twitch > 75% twitch > 50% twitch. Finally, both variants of the Al-Si-Mg-Fe alloys showed a large volume fraction of Fe- and Si-containing intermetallics and additional work is needed to discern differences in their respective corrosion responses.

In summary, correlating local electrochemical behavior (e.g. via SECCM) with micro/nanostructure, in conjunction with bulk mechanical behavior, can help identify the right fabrication method and alloy chemistry to minimize SCC issues in Al alloys.

Table of Contents

1.0 Introduction

Maximizing fuel efficiency and minimizing carbon emissions have long been major goals in the automotive industry [1-4]. Replacing steel structural components with lightweight, high-strength cast and wrought aluminum versions has been a crucial step in achieving this goal. Although the next step in offsetting carbon emissions is arguably the transition from internal gas combustion to hybrid and fully electric engines [5-7], the need for lighter, more energy-efficient components is still pressing. Regardless of the engine type and energy-efficiency requirements, next-generation components (e.g., steering knuckles) will be exposed to environmental conditions in local climates (such as varying temperatures, precipitation, chemicals, and dirt) and, thus, potentially rapid environmental degradation. Understanding and controlling the performance-degrading effects of the environment on aluminum alloys is not uniquely beneficial to the automotive industry. Al alloys are also frequently utilized for aerospace and marine applications and even in biomedical components, where a failure mechanism like stress corrosion cracking (SCC) would threaten to increase mortality [8].

SCC is one of the most devastating failure mechanisms of aluminum structural components. Beyond aluminum alloys, SCC can also gravely affect a wide range of materials systems in various applications, from stainless steels and Ni-base alloys in the nuclear industry [9, 10] to Cu alloys in heat exchanger tubes used in chemical processing plants, marine environments, desalination plants, and HVAC systems [11]. Depending on the alloy, SCC can manifest itself in different forms, with each type controlled by various mechanisms [12-14].

Al alloys containing a high concentration of soluble alloying elements such as Cu, Mg, Si and Zn, are susceptible to SCC. For example, cast alloy series containing Cu (2xx) and the wrought alloy series containing Cu (2xxx), Mg (5xxx), and Cu and Zn (7xxx)) are highly susceptible [13-16] where SCC is most often observed as intergranular (IG) failure [13]. Two mechanisms have been proposed to explain IGSCC, anodic dissolution and hydrogen embrittlement at grain boundaries. These particular alloys are precipitation-hardened through the addition of Mg, Cu, Si, and Zn. Grain boundaries lined with a high density of precipitates and the adjoining solute-depleted area are believed to be more anodic than the surrounding aluminum matrix. The resulting galvanic coupling between the grain boundary and the matrix regions causes dissolution and localized corrosion at the grain boundary crack propagation along the anodic path is aided by stress concentrations at the crevice and locally altered chemistry of the corrosive environment to facilitate more rapid dissolution. The mechanism surrounding hydrogen embrittlement causing SCC is still less clear and broader, as it has been described through at least three categories: 1) hydrogen induced decohesion, 2) hydrogen enhanced localized plasticity, and 3) cleavage of hydrides formed at the crack tip. The introduction of Mg in these alloys is thought to increase localized activity at grain boundaries, hence increasing hydrogen entry [13]. Brittle hydrides can form on Mg rich hydrides on the incoherent portion of the grain boundary, thereby weakening it as localized stresses are applied.

While there has been considerable work on SCC of 2xxx-7xxx series (wrought) alloys, there have been fewer studies on 2xx series (cast) alloys. The 2xx series alloys (e.g., A206) are more modern cast alloys containing ~4 wt. % Cu; they are significantly stronger than other cast Al alloys [17] but tend to suffer from SCC and hot tearing [17-19]. Grain refinement [18] , and more recently, the introduction of nanoparticles to casting formulations have been shown to reduce hot tearing [20-23]. Metal matrix nanocomposites (MMNC) have led to improved mechanical, thermal, and structural properties of cast Al alloys, but only if the nanoparticle phase was homogeneously dispersed after processing [23]. A wide range of nanoparticles, from Al_2O_3

oxides to carbides and nitrides, have been incorporated into lightweight cast alloys such as Al and Mg [22, 24]. If the SCC problem (and corrosion in general) in Al 2xx alloy can be mitigated, it would allow the automotive industry to cast high-strength lightweight aluminum structural components as a replacement for heavier ferrous/cast iron components. Therefore, this project examined the influence of the cast microstructure via the casting process (cooling rate) and the presence/absence of nanoparticles on the SCC behavior of the 2xx Al alloy A206.

In order to investigate the SCC susceptibility of Al alloys a wide range of testing methods, from quality assurance testing (dip testing) [25], to slow strain rate testing (SSR) [26], to breaking load methods [27, 28], to automated stress corrosion ring testing (ASCOR) [29], have been proposed. Each test methodology has advantages and disadvantages. Dip testing following ASTM G44 is a simple pass-fail test where samples are first immersed in a 3.5% NaCl (salt water) solution for a specific amount of time before being dried and then re-immersed. After immersion testing, the samples are strained until failure to determine the failure load. More complex methods, such as SSR and ASCOR, accelerate the failure of the tested alloy in solution, thereby providing rapid results.

This work centers on the use of the ASTM G44-99 and G139-5 test methods in combination with high-resolution analytical characterization to understand SCC susceptibility in three different sets of Al alloys: (i) Cast A206 Al alloys (with and without nanoparticles) in the T6 temper condition, (ii) wrought tubes made of twitch and pre-consumer Al 6061 scrap that were extruded via PNNL’s ShAPE process, and (iii) cast Al-Si-Mg-Fe alloys that mimic recycle grade Al alloys. Microstructural examinations were performed to help elucidate failure mechanisms in corrosion tested samples. Microchemical analysis methods were also applied to help understand how the alloys reacted to electrochemical stimulus at the micrometer level.

2.0 Experimental

2.1 Samples

A series of aluminum alloy A206 tensile (dog bone) specimens were cast at Eck Industries using different conditions. Nanoparticle additives were added to one group of samples for each casting condition for grain-size refinement and potential nano-strengthening. Three different types of molds (sand mold with chill, sand mold without chill and permanent mold), with and without nanoparticle additions to the melt, were used to produce six different casting conditions and their corresponding microstructures in the castings. Stress corrosion testing and microstructural characterization of the test coupons were conducted at PNNL. Table 1 lists the sample IDs corresponding to casting conditions and presence/absence of nanoparticle addition. Table 1 lists the sample IDs corresponding to casting conditions and presence/absence of nanoparticle addition. Various combinations of labeling will be utilized throughout the report, with Table 1 being utilized as a reference guide.

Table 1: List of Samples Provided by Eck Industries for SCC Testing

Eck Industries Sample Label	PNNL Label	Casting Type	Nanoparticle Additive
A206-T6 Sand Cast With Chill	A	Sand Cast -With Chill	No
A206N-T6 Sand Cast With Chill	D	Sand Cast- With Chill	Yes
A206-T6 Sand Cast No Chill	B	Sand Cast-No chill	No
A206N-T6 Sand Cast No Chill	E	Sand Cast- No Chill	Yes
A206-T6 PM	C	Permanent Mold	No
A206N-T6 PM	F	Permanent Mold	Yes

Figure 1 shows examples of the dog bone-shaped tensile samples received from Eck Industries, including at least 11 samples for each condition. An inventory of the remaining samples sets can be seen in the Appendix Figures 74 and 75. The as-received samples were documented and 5 random samples from each set were arranged on a plastic mesh in a plastic container (Figure 2) for subsequent SCC testing with PNNL labeling corresponding to Table 1.

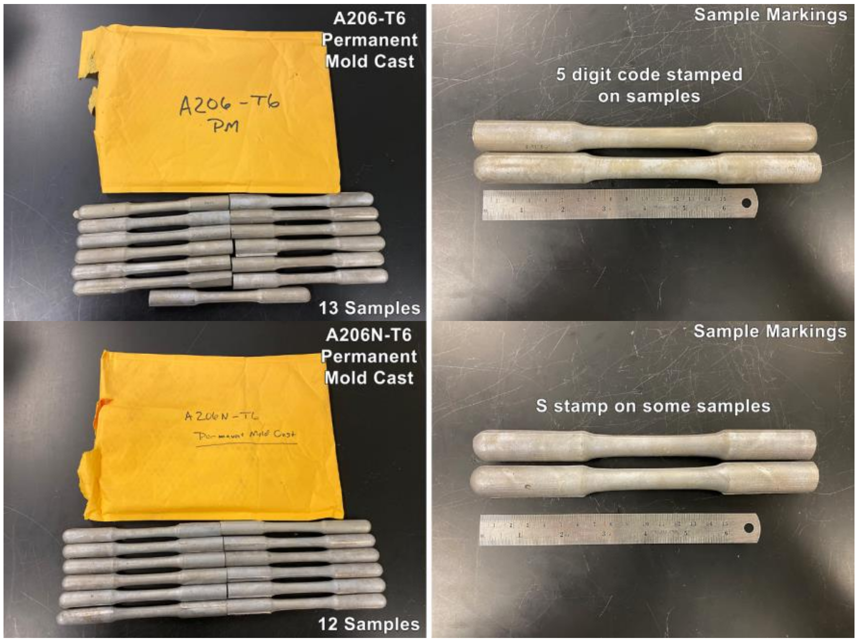

Figure 1: A206-T6 samples cast in a Permanent Mold (with A206N containing nanoparticles). The A206-T6 sample bag contained 13 samples.

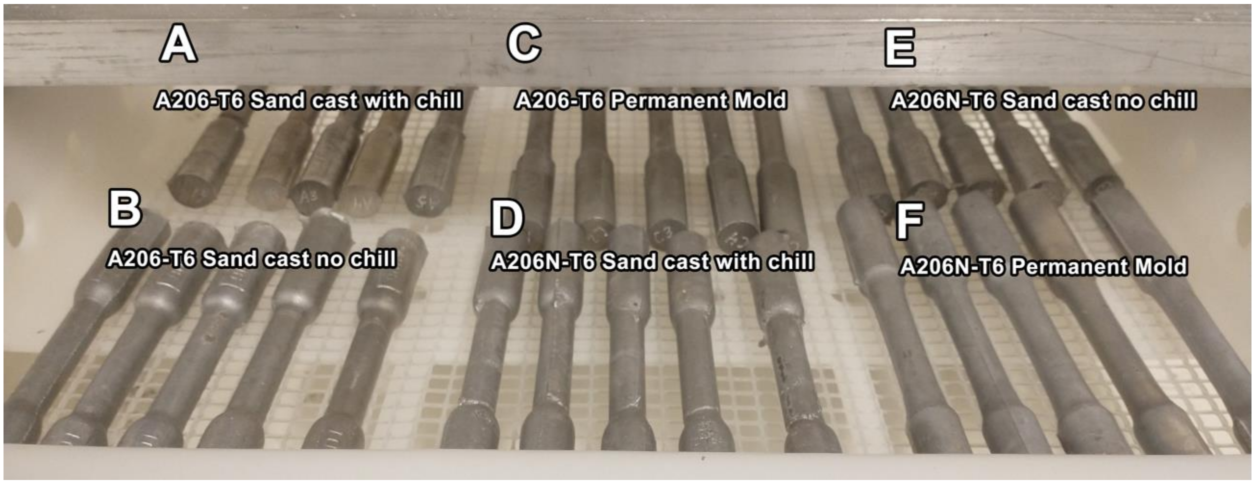

Figure 2: Photograph showing the orientation of the samples laid out on a plastic mesh that allowed free flow of saltwater solution around the samples during testing. Labels A-F are PNNL designations for sample tracking (Table 1).

2.2 SCC Testing Setup

In order to perform stress corrosion cracking (SCC) testing on the various A206 samples, an alternate immersion test described in ASTM standards G44-99 and G139-5 were performed [25, 28]. Residual stresses from casting and the subsequent T6 heat treatment together with the 3.5% NaCl solution cause the SCC response. Tests were performed in a *Singleton* environmental chamber (Figure 3a) that digitally monitors and controls the temperature and relative humidity (RH) (Figure 3b). The temperature and RH were additionally independently tracked with an *Autopilot* monitor. An automated pneumatically controlled frame and plastic tray (Figure 3a) were built to hold 30 samples and dip them on a timed scheduled using a timer controller (Figure 3c) on the pneumatic system. This setup was custom-built and programmed at PNNL.

The test utilizes a 1-hour cycle that includes a 10-minute specimen immersion period in an aqueous solution of 3.5% sodium chloride followed by a 50-minute specimen drying period during which the specimens are elevated out of the solution. This 1-hour cycle is continued 24 h/day for 30 days (i.e. 720 hours) in the present work. The 3.5% NaCl bath was prepared using >99% pure sodium chloride (NaCl) from *Spectrum Chemicals* in quadruple demineralized filtered distilled (DI) water prepared by agitation mixing. A peristaltic pump replenished the water that evaporated from the bath over the course of the experiment (which would otherwise cause changes in salt concentration and bath volume) at a constant rate.

An example of the corroded sample surfaces during testing is shown in Figure 4.

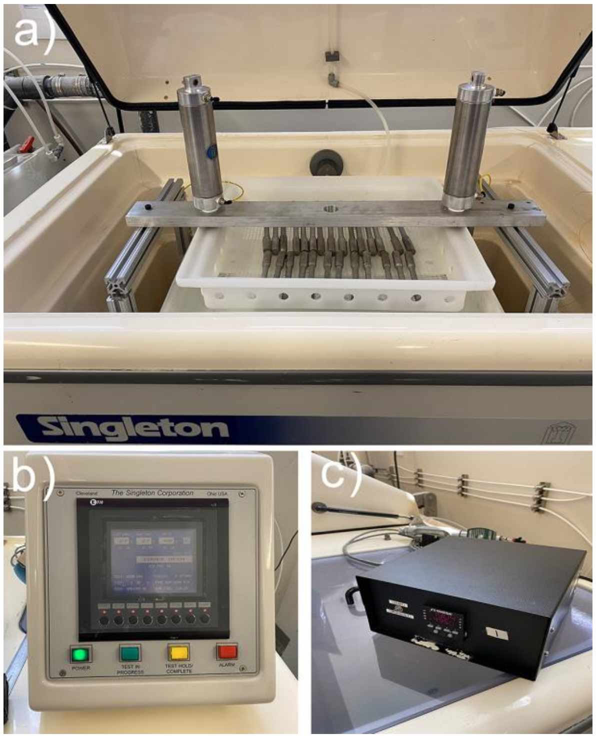

Figure 3: Photographs illustrating the SCC setup placed within the modified *Singleton* environmental chamber. a) Plastic sample tray (with holes on the side walls) and pneumatic actuation mechanism to move the samples in and out of the salt solution at periodic intervals. b) Singleton controller showing the current temperature of the container. c) Controller box with a counter to record the number of immersion + drying cycles during the test duration.

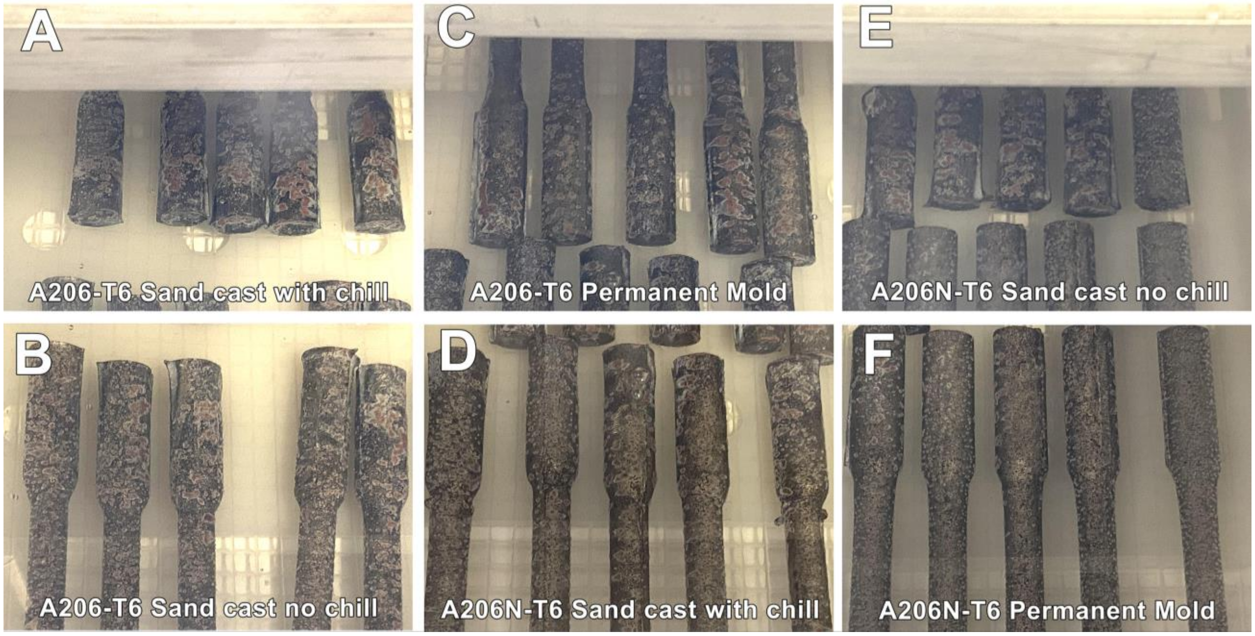

Figure 4: Photograph showing corroded samples at the half-way mark (~360 h) during testing.

2.3 Tensile Testing

To assess the influence of corrosive attack on the tensile strength of the materials, un-corroded as-received specimens and those subjected to 720 h of exposure in the alternate immersion test were tensile tested to fracture. Some of the flash was filed off the ends of the tabs to make the end of the specimen fit in the grips of the test rig, but this was done far from the gauge section. No additional modifications were made to remove casting marks or straighten bent samples. Specimen diameters were measured at four locations along the length of the gauge; two measurements were taken at each location perpendicular to each other. The average of the eight measurements was reported as the specimen diameter.

Tensile testing was performed on an *Instron 8801* servohydraulic testing system. Data was collected from a 100 kN load cell and strain was measured with a *3542-0200-100-LT* 2” extensometer. Tests were conducted at an extension rate of 12.7 mm/min and data were collected at 200 Hz. Calculations were made within the *Instron Bluehill Universal* controlling software to determine Young’s modulus, yield strength (0.2% offset), ultimate tensile strength and elongation at break.

2.4 Metallurgical Preparation

Sample cross-sections were prepared for microstructural evaluation (i.e., optical and electron microscopy) from both untested and corroded samples. Cross-sections were prepared from the middle of the gauge section using a slow-speed saw and subsequently potted in epoxy. The mounted samples were then polished using successively finer grits and ending with a final colloidal silica polish. Some samples were treated with a gentle acid etch to reveal grain contrast for grain size analysis by optical microscopy.

The acid etch procedure entailed preparing a sodium hydroxide solution (12 g of NaOH in 100 mL of distilled (DI) water) heated to ~45-55°C. The freshly polished samples were dipped into the etching solution for 10 seconds and immediately rinsed by immersion and stirring in room-temperature DI water for another 10-15 seconds. Final rinsing was performed with ethanol before drying in a stream of air.

2.5 Optical Microscopy

Cross-section samples (un-tested) that had been lightly etched were analyzed using an *Olympus BX51* optical microscope in polarized light mode to record the microstructure and grain size distribution. The line intercept method was utilized to determine the average grain size from the optical microscopy images.

Pore size and precipitate analysis were automatically performed in a manner similar to the Image J analyses of the optical images.

2.6 Electron Microscopy

Cross-sections of the gauge regions of both un-tested and SCC-tested samples were prepared using metallographic preparation, as noted above. The epoxy on all epoxy-mounted samples was either masked off using thin copper tape, or the entire metallography mount was coated with a thin layer of carbon to ensure conductivity in the scanning electron microscope (SEM) and focused ion beam (FIB) milling instruments.

SEM analysis was performed on a *JEOL IT800 SEM* at variable accelerating voltages ranging from 5-20 kV, depending on the analysis type. Energy dispersive spectroscopy (EDS) analysis was performed at 20 kV using an *Oxford 120* mm^2 *X-Max* detector, and electron backscatter diffraction (EBSD) was collected at a step size of 100 nm using an *Oxford Symmetry* detector.

Backscatter electron analysis (BSE) was collected to illustrate the microstructure down to the hundreds of nanometers as well as the fine scale analysis of the corrosion pathways. Electron backscatter analysis was done to compare to the line intercept method in optical analysis. Lastly, as noted above, energy dispersive spectroscopy (EDS) was applied to provide an indication of both the general grain chemistry, inclusion identification, and oxide chemistry.

Transmission electron microscopy (TEM) samples were prepared using a dual-beam *FEI Quanta 3D* FIB. Site-specific regions of interest (i.e., grain boundaries and crack tips) were selected and extracted to TEM grids with a standard lift-out procedure and thinned to electron transparency using successively smaller ion beam currents.

TEM, while a much more localized technique, allows insight into the grain boundary chemistry and crystallography of precipitates and base metal grains. Line-scans collected across grain boundaries provide insight as to how they might respond to a corrosion environment.

Once prepared, samples were analyzed in both transmission and scanning transmission modes (S/TEM) using a *JEOL ARM 200CF* aberration (C_S) corrected microscope equipped with a *Centurio* EDS detector with a 0.9 sR solid collection angle.

2.7 Scanning Electrochemical Cell Microscopy (SECCM)

Scanning electrochemical cell microscopy (SECCM) is a versatile technique for understanding corrosion mechanisms in alloys due to its ability to obtain localized electrochemical measurements. SECCM allows direct voltammetric-amperometric measurements at the target position at the sample surface. SECCM probes corrosion processes at the (sub)micron-scale to enable an understanding of the influence of microstructural factors (grains, grain boundaries, inclusions, etc.) on the electrochemical stability (corrosion susceptibility, pitting, passivity) of the metal surfaces. For example, SECCM can be used to measure the time-dependent open circuit potential (OCP) and Tafel polarization curves. The OCP is a resting or equilibrium potential when metal meets the solution and is used to determine corrosion susceptibility. Lower (more negative OCP values indicate less noble (anodic/more corrosive) surfaces, and higher (more positive) OCP values indicate more noble (cathodic/less corrosive) metal surfaces. Tafel polarization curves provide a gauge for the current response. Scanning potential sweeps between ±100 mV vs. OCP reveal the characteristics of the corrosion behavior defined by corrosion potential (E_{corr}) and corrosion current (I_{corr}). The comparison of OCP, E_{corr} and I_{corr} determined using SECCM performed on selected locations on the surface (i.e., at grain boundaries (GB), inside grain (IG)) will enable us to identify the unique corrosion properties of these microstructural features.

To facilitate such site-specific measurements, SECCM employs the use of a small laser-pulled theta capillary tube with a ~3-5 µm tip diameter (see Figure 5). The capillary tube was filled with 0.01 M NaCl electrolyte solution using a micro syringe, causing a droplet to form at the end of the capillary. A dual-barrel SECCM probe was used for the examinations. An AgCl wire of 0.25 mm diameter inserted into one barrel acted as a quasi-reference electrode, and a Pt wire of 0.25 mm diameter inserted into the other barrel acted as the counter electrode. This theta capillary probe, including the counter (CE) and reference electrodes (RE), was mounted on a Z-piezoelectric positioner.

Careful and precise positioning of the theta probe on a sample surface is required to avoid probe breaking or damage. A bias potential of ~20 mV was applied to the alloy (acting as the working electrode [WE]), and the feedback current on the WE was continuously monitored (Figure 6). The droplet formed at the end of the theta probe was brought into contact with the working electrode using the following “tip-down procedure.”

When the probe is in air, there is no contact between the droplet meniscus and the surface; thus, the DC conductance current is null. The theta probe was slowly moved towards the WE in the Z-direction at a speed of 0.2 µm/S. The controller was programmed to automatically stop the Z-movement of the probe as soon as a spike of 3 pA in the feedback current was detected. This spike signaled the landing of the droplet on the WE. It is important to note that the glass body of the probe never touches the WE, only the droplet formed at the end of the probe is in contact with the surface. Once the theta probe had successfully approached the WE and the droplet was in contact with the WE at a particular location, a sequence of calibration OCP and Tafel polarization measurements were performed (Figure 7). The corrosion kinetic measurements on a Mg single crystal and polycrystalline Mg with known susceptibilities were compared to assess the reliability of the set-up. An OCP measurement was performed until a constant potential region was reached after 2 mins. Subsequently, Tafel polarization was performed from cathodic to anodic direction within ± 100 mV at a sweep rate of 20 mV/s.

With the use of high-resolution optical microscopy, individual grains and grain boundaries can be targeted depending on the grain size (Figure 6). Initially, a 10 µm tip was employed for targeted landing on isolated grains. However, post-testing optical microscopy examination of the surface evaluated with the 10 µm tip indicated that the NaCl solution used during SECCM testing spread on the surface, and the NaCl crystallized when the solution dried (Figure 8). The solution spreading and wetting of a larger testing area significantly limited the lateral resolution of the SECCM technique. To improve resolution, the tip size was reduced to ~3 µm in subsequent experiments. Testing with ~3 µm tip did not appear to cause liquid spreading or salt crystallization over a larger sample area. Each SECCM data point includes measurements from landing the tip inside a grain and at a grain boundary. These measurements were repeated for 25 intragranular locations and 25 grain boundaries to obtain statistically significant data.

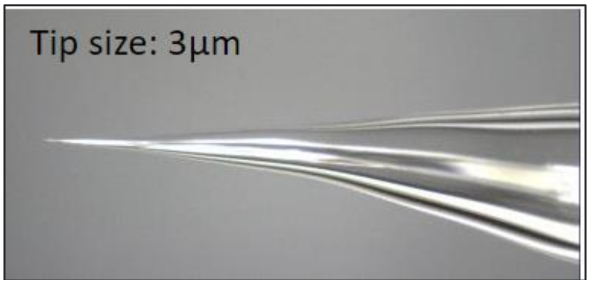

Figure 5: Theta capillary tip (~3 µm in diameter) used in SECCM testing to probe local corrosion measurement of the alloys.

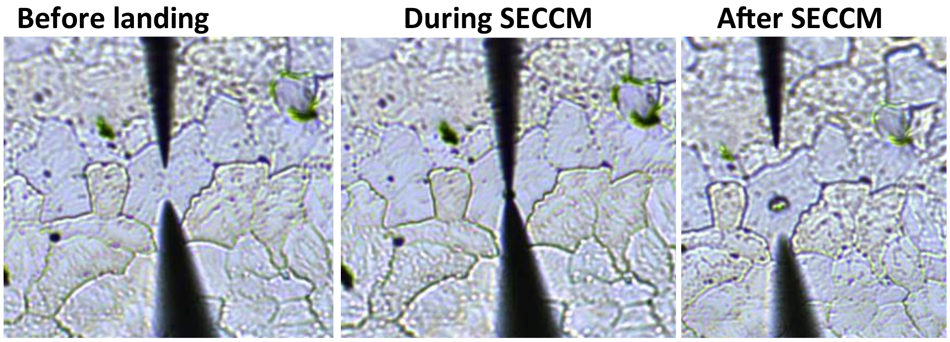

Figure 6: Optical micrographs illustrating how the SECCM technique is performed on an alloy with grains on the order of 10's of micrometers. In this example, the probe is utilized to land inside a single grain and measure the electrochemical corrosion potential (OCP). The dark conical feature on the top is the probe tip while the bottom conical feature is the tip reflection in the polished sample.

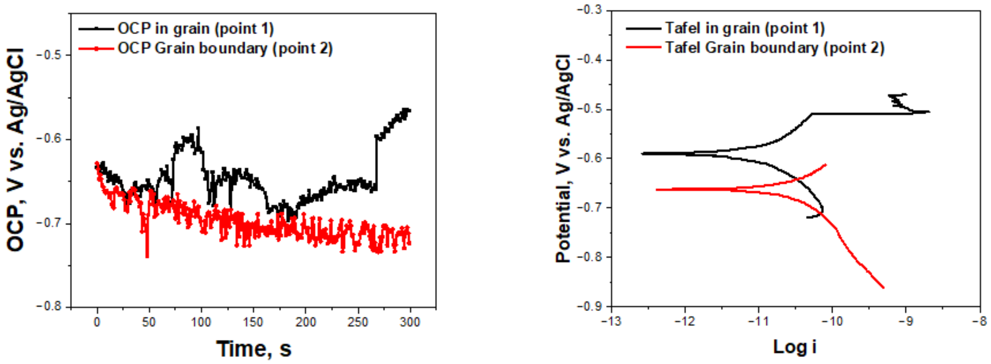

Figure 7: Electrochemical plots collected in the SECCM analysis. OCP versus time and Potential versus Log I using a 10 µm tip.

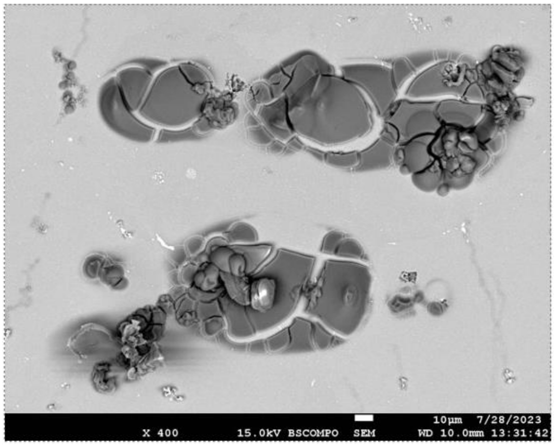

Figure 8: SEM(BSE) micrograph showing the deposited salt solution post SECCM testing when using a 10 µm tip.

3.0 Results

3.1 SCC Testing

The SCC testing was conducted over 30 days, during which data logging was performed (Figure 9). The ASTM acceptable tolerances for RH (± 10%) and temperature (± 1°C) are shown in the orange and blue solid filled boxes, respectively. The external controller and Singleton measurements indicated that the RH was within the acceptable range. The temperature, which has a much tighter tolerance of only 2°C, varied slightly (less than 0.5°C) from the tolerance interval on two occasions during the experiment. The minimal deviations are not believed to have caused significant concerns during the experiment. Whereas the Singleton controller was in good agreement with the external controller for the RH measurements, the utilization of a calibrated external controller for temperature was particularly beneficial as the Singleton controller (which is more difficult to calibrate) measured consistently a few degrees higher and out of range of the ASTM specification.

The data presented in this section, 3.1, and the following section, 3.2, satisfy Milestone 1 for completing SCC testing of A206-T6 alloys with two different grain sizes.

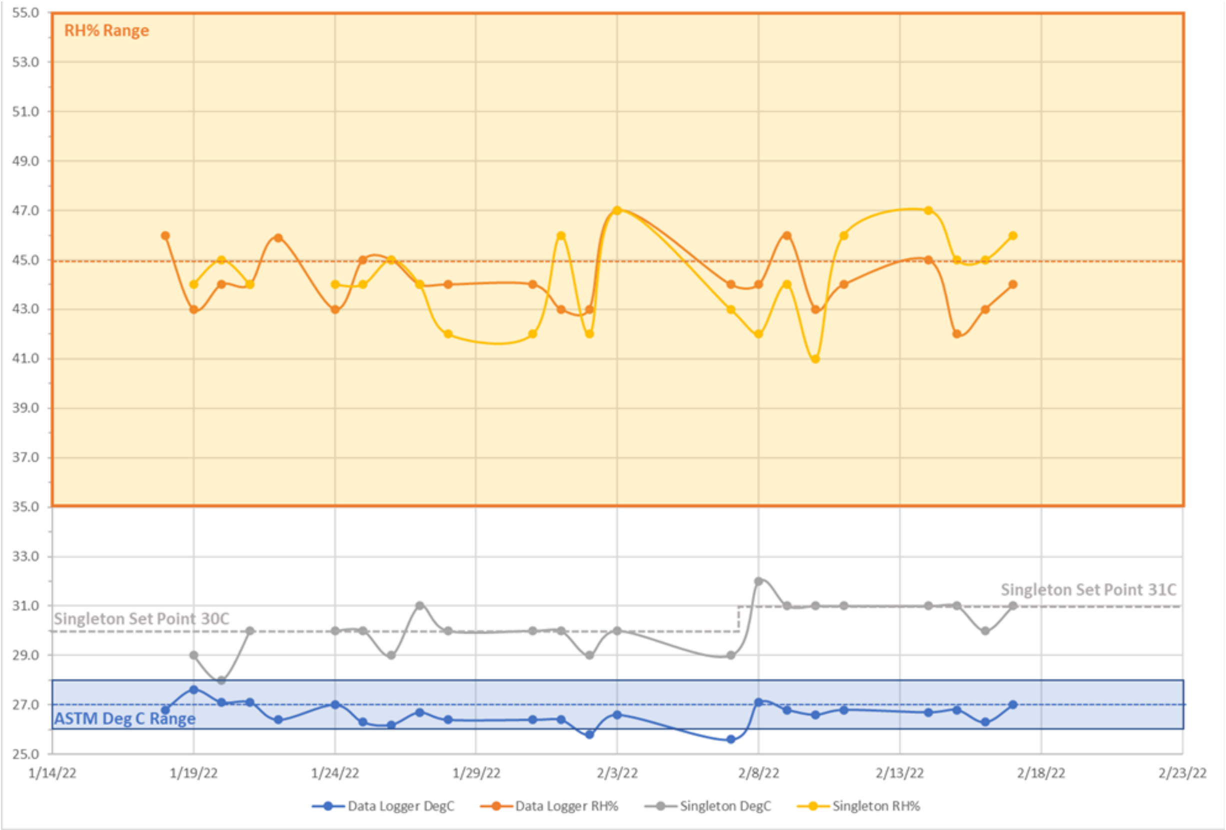

Figure 9: Environmental data collected during SCC testing.

3.2 Tensile Testing

At least five samples of each A206-T6 material were tested in the as-received and corroded state, with representative images shown in Figure 10. The red arrows indicate white fiduciary markers for the optical extensometer. Representative corrosion surfaces for these materials are also shown in Figure 10. The rough exterior and mottled contrast provided challenges in using the optical extensometry set up because lines could not be drawn as uniformly as in the as-received samples. For this reason, both optical and mechanical extensometer data were collected for all samples. However, only the mechanical extensometer data is presented.

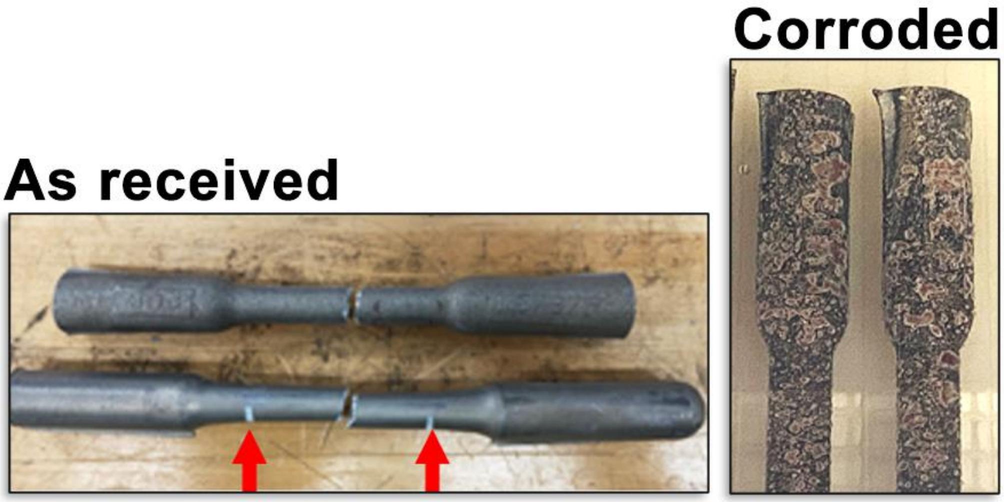

Figure 10: Photographs of two representative as-received tensile samples after pulling to failure (left) and two representative samples after corrosion (right). Note: failure occurred in the center of the gauge section. Red arrows in the left image indicate white lines drawn on the sample for optical extensometer readings (note that due to inconsistent readings, optical extensometry readings were not used). The right image shows the rough speckled surfaces on the corroded samples, which affected the optical extensometer data.

Representative engineering tensile testing data is presented in Figures 11 and 12 for the permanent mold samples, cast without and with nanoparticle addition, respectively. Similar engineering stress-strain plots for the sand cast with and without chill, cast without and with nanoparticle addition, are plotted in Figures 76 through 79 in the Appendix. A summary of the tensile testing data for all samples is shown in plots (Figures 13-15) and in tabular form (Table 2). Error bars were calculated and included in Figures 13-15. Samples in Figures 13-15 are labeled as PM (permanent mold), SC-C (Sand cast with chill) and SC-NC (Sand cast no chill) with either an O or an N designation for original (without nanoparticles) and with nanoparticles, respectively.

In the majority of cases, the corroded samples exhibited strain at break lower than the corresponding uncorroded as received samples, and in almost all cases showed ultimate tensile stresses lower than the uncorroded as-received samples. When the optical extensometer did not produce correct reading, only the mechanical extensometer data was utilized.

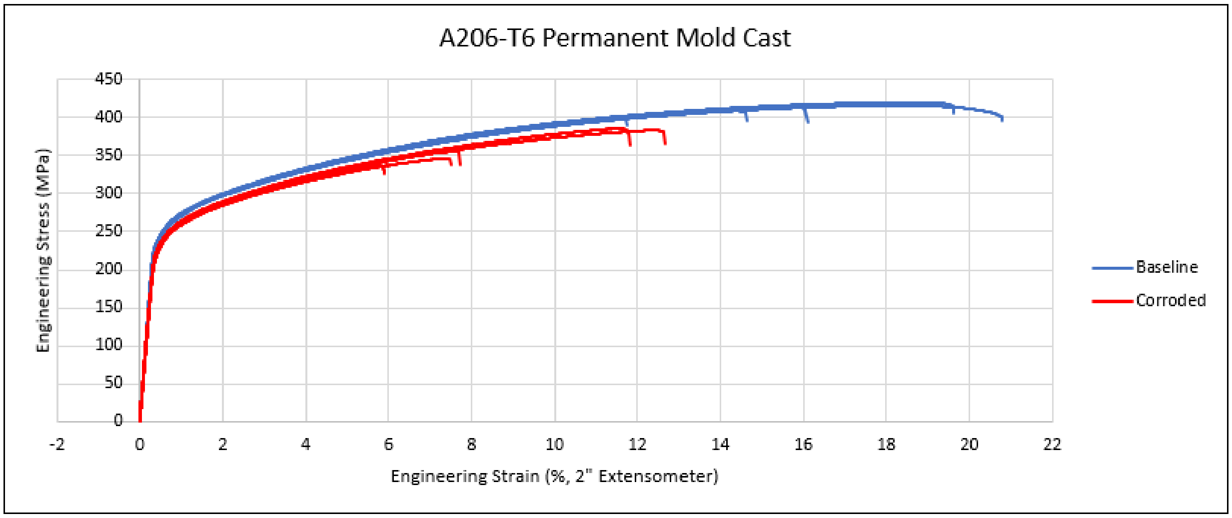

Figure 11: Plot of engineering stress (MPa) versus engineering strain (%) (using a 2” mechanical extensometer) for the A206-T6 permanent mold (C) samples. Baseline refers to the uncorroded, as-received samples.

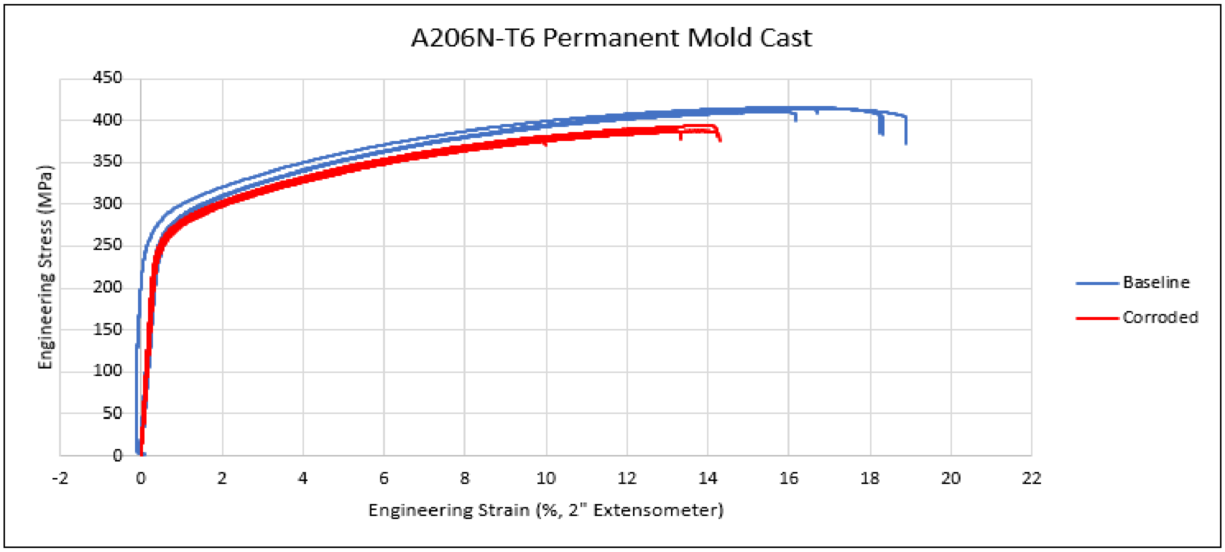

Figure 12: Plot of engineering stress (MPa) versus engineering strain (%) (using a 2” mechanical extensometer) for the A206-T6 permanent mold:nano (F) samples. Baseline refers to the uncorroded, as-received samples.

The yield stress (calculated by the 0.2% offset method) indicated that in each case, the samples with nanoparticles were stronger than their counterparts without nanoparticles. The yield stress increased in the order: permanent mold < sand cast with chill < sand cast no chill (Figure 13 and Table 2). The sample that was sand cast, no chill and with nanoparticles (SC-N-NC) exhibited the highest yield stress of all the samples tested in this work. Comparing the corroded samples to the uncorroded (as-received samples), there was statistically no significant difference in any of the sets and no consistent trend across all casting conditions. In some cases, the average yield stress was higher (e.g., PM-O, SC-N-C, and SC-O-NC) in the corroded samples. In other cases, the yield stress was lower in the uncorroded samples (e.g., PM-N, SC-O-C, and SC-N-NC). No clear trend for as-received (uncorroded) as compared to corroded could be observed.

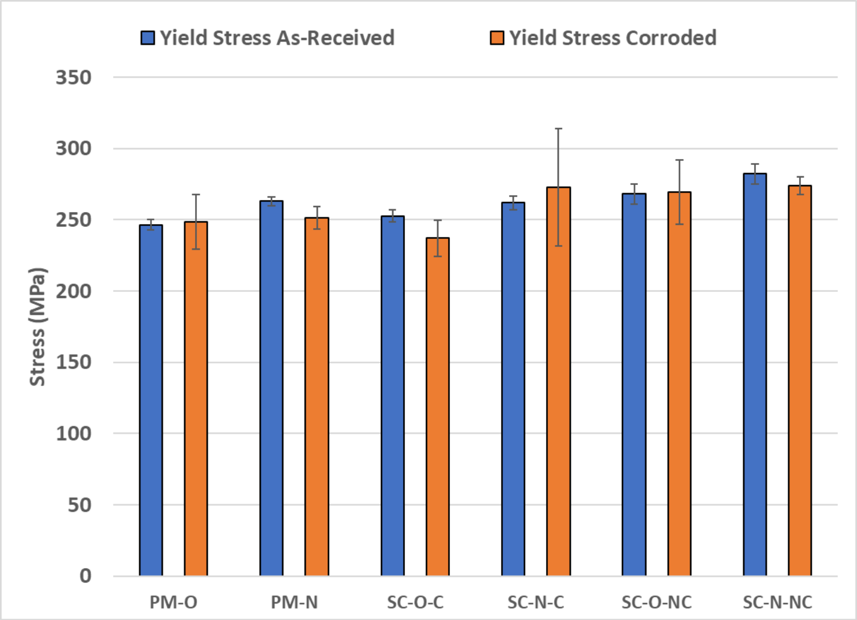

Figure 13: Plot of the average yield stress for the as-received and corroded samples.

However, Figure 14 illustrates that for each casting type the corroded samples failed at lower ultimate tensile strength (UTS) than the uncorroded, as-received samples. Only for the SC-O-C and SC-O-NC conditions the standard deviations for the UTS of the corroded/uncorroded samples overlapped (Table 2). Comparing the as-received, uncorroded samples against one another, there appeared to be little to no difference between each designation. Slight variations among the corroded samples were noted, with the SC-O-NC corroded sample exhibiting the highest UTS, this was also one of the samples with the least degradation of UTS as a result of corrosion.

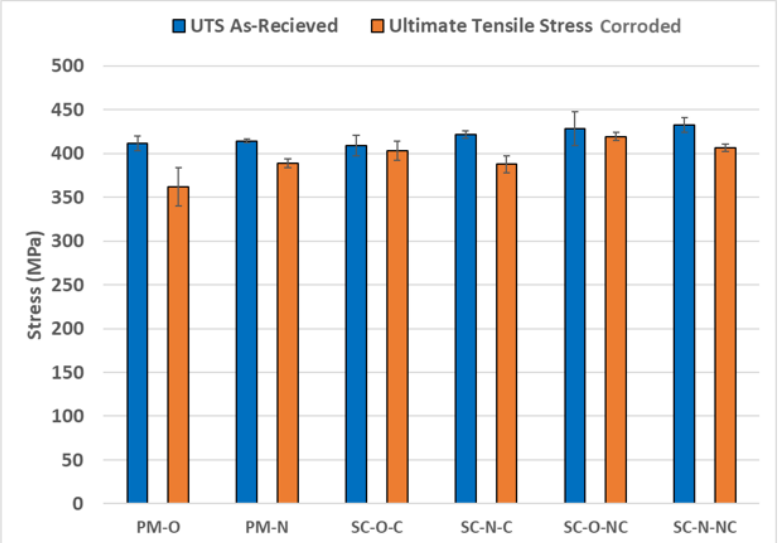

Figure 14: Plot of the average utlimate tensile strength (UTS) for the as-received uncorroded and corroded samples.

Lastly, the average strain at break for each set of samples is provide in Figure 15 and Table 2 and showed that in all cases the corroded samples failed at a lower strain than the original (as-received, uncorroded) samples (except in the case of the SC-O in both the chilled and no chill cases, the data was within a standard deviation with some samples expressing large error bars). Between each of various types of as-received samples there was no statistical difference in the strain at break, although in the corroded state the PM-O and SC-N-C showed the lowest strains at break.

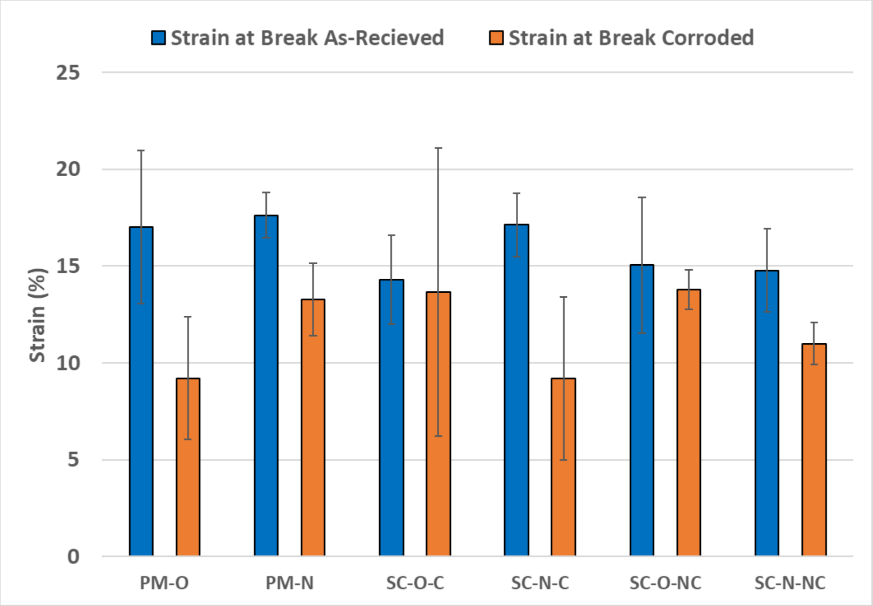

Figure 15: Plot of the average strain at break for the as-received uncorroded and corroded samples.

Table 2 provides the tensile testing data for the as-received and corroded samples. Additionally, of the tested samples, an indication of where the samples failed within the length of each sample was noted. Three different indications of failure were denoted; in the gauge, at the extensometer, and at/outside the extensometer (if there was a mixture of failure locations within the batch). Table 2 is color coded for rapid identification in terms of failure, with green being majority inside the gauge section, yellow at/outside the extensometer, and light yellow for a mixture of in the gauge and at/outside the extensometer. These indicators correlate strongly with the permanent mold and the sand cast without chill samples (both with and without nano) failing in the gauge section and the Sand Cast with chill (both with and without nano) failing with the majority at or outside the extensometer.

Table 2: Summary of Tensile Testing for Uncorroded and Corroded Samples.

Sample Type	Yield Stress (MPa)	UTS (MPa)	Strain at Break (Physical) %	Notes on failure location
Permanent Mold	249.6 ± 1.8 (Ext.)	411.5 ± 8.2	16.5 ± 3.7	3/5 Broke in gauge
Permanent Mold Corroded	238.8 ± 2.2 (Ext.)	361.9 ± 21.7	9.1 ± 2.9	4/5 Broke in gauge
Permanent Mold Nano	266.3 ± 1.8 (Ext.)	414.2 ± 2.1	16.8 ± 0.9	5/5 Broke in gauge
Permanent Mold Nano Corroded	256.5 ± 5.6 (Ext.)	388.7 ± 5.0	12.9 ± 1.7	5/5 Broke in gauge
Sand Cast Chill	244.5 ± 4.6 (Ext.)	409.1 ± 11.8	15.4 ± 1.8	5/5 Broke at extensometer
Sand Cast Chill Corroded	239.3 ± 5.0 (Ext.)	403.1 ± 11.0	16.7 ± 3.5	2/5 Broke in gauge, 3 outside/at ext.
Sand Cast Chill Nano	258.4 ± 2.0 (Ext.)	421.4 ± 4.2	14.3 ± 7.6	5/5 Broke at/ outside extensometer
Sand Cast Chill Nano Corroded	255.1 ± 9 (Ext.)	387.8 ± 9.6	11.7 ± 2.5	2/5 Broke in gauge, 3 outside
Sand Cast w/o-Chill	271.0 ± 4.4(Ext.)	428.4 ± 19.3	15.1 ± 3.5	3/5 broke in gage, 2 at ext.
Sand Cast w/o-Chill Corroded	264.8 ± 2.5 (Ext.)	419.1 ± 4.5	13.6 ± 0.9	5/5 broke in gage
Sand Cast w/o-Chill Nano	281.8 ± 5.4 (Ext.)	432.6 ± 8.5	12.7 ± 4.7	3/5 Broke in gauge
Sand Cast w/o-Chill Nano Corroded	274.2 ± 2.2(Ext.)	406.3 ± 4.3	10.8 ± 1.0	5/5 Broke in gauge

3.3 Microstructural Analysis

Samples were analyzed using both optical and electron microscopy analysis techniques to assess and compare the capabilities of each technique in helping understand mechanical (tensile testing) and electrochemical (measured using scanning electrochemical cell microscopy (SECCM)) responses. As noted in Section 2, samples were cross sectioned at the gauge, potted in epoxy, and then polished to a colloidal silica finish, with a certain set of samples being lightly etched for optical analysis. Correlative microscopy studies such as these are performed to better understand how to optimize the analysis techniques for each sample to maximize research impact.

While not explicitly described as part of an individual Milestone, this work was performed to compliment the three other Milestones to help elucidate the results. Although the addition of this section adds considerable length to this report, it is intended to provide deeper insight into the overall project.

3.3.1 Optical Microscopy Analysis

An optical micrograph (reflection mode) of cross-section of the Permanent Mold sample (Sample F) is shown in Figure 16 in addition to an Image J software-implemented mask to delineate voids only (and mask the remainder microstructure) within the sample. Contrast thresholding was utilized by which the dark contrast voids were selected in the program until all voids were counted. The remainder of the optical data from the additional samples is provided in the Appendix, Figure 82. The void analysis from each of the Image J analyses across a 5x5 mm^2 area in the center of the samples was recorded and tabulated in Table 3. In the sand cast with chill sample, the pore density in the non-nano and nano samples was similar. From these results, it seems that nano additions affect the pore density in both the sand cast without chill and the permanent mold samples.

At higher magnification, differential image contrast (DIC) images for each sample type are provided in Figure 17. DIC imaging utilizes scattering of polarized light due to crystallographic orientation to delineate the grain structure. The linear intercept method was then applied to each of the samples to assess the average grain size. The tabulated data for the grain size measurements is provided in Table 3. The processing route (i.e. casting technique) is expected to affect the grain size, not only due to the different cooling rates in each technique, but also due to the addition of nanoparticles. As expected, the metallic mold used to fabricate the permanent mold sample exhibited the smallest grain sizes amongst the three casting conditions. Of the sand cast samples, the sand cast samples with chill exhibited the smallest grain size of the two as expected due to the rapid cooling rates.

With regards to the addition of nano particle forming additives, in both the sand cast samples, the nano samples did exhibit smaller average grain sizes than their non-nano counterparts, but statistically the standard deviation suggests there is not much of a difference. The images in Figure 17 (which are all at the same magnification) would suggest that the grains in the nano samples are smaller, but a number of grains much smaller than the average grain size are noted throughout the microstructure. This contrasts with the nano sample micrographs where the grain sizes appear very uniform. This is also corroborated by the data in Table 3 where the standard deviation in the samples without nano have larger standard deviations. Comparing the sand cast samples with nano additives demonstrates that the use of nano additives appears to outweigh the cooling rate, as both samples D and E showed nearly similar grain sizes, as compared to the samples without nano that showed a slightly larger difference.

Lastly, the use of nano additives in the permanent mold samples had opposite effect as compared to the sand cast samples.

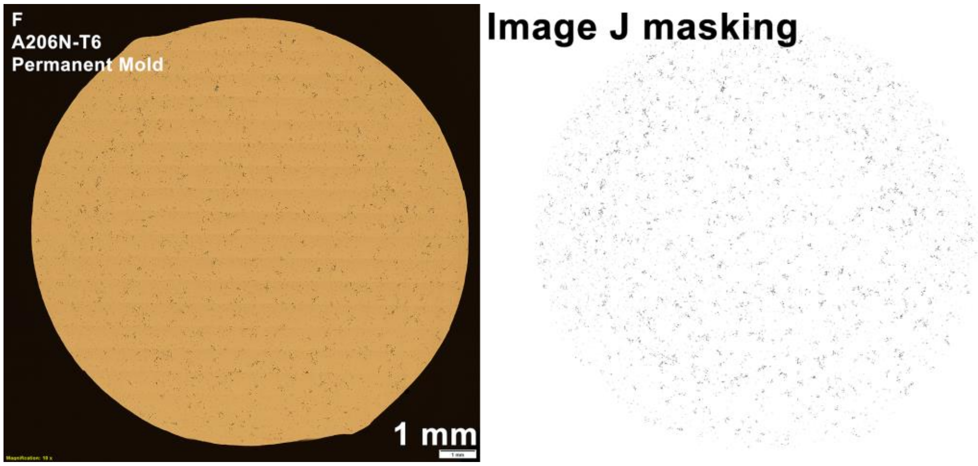

Figure 16: Optical montage micrograph of the cross-section of the Permanent Mold sample F and corresponding Image J-software analysis showing only the pores (black dots).

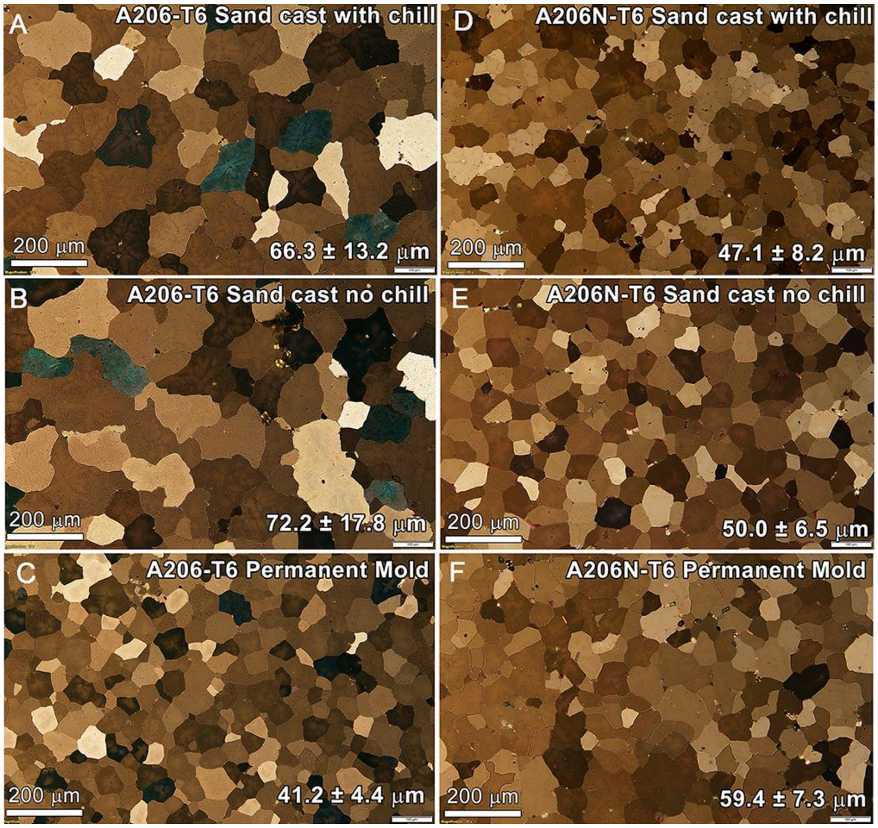

Figure 17: Representative optical micrographs of all the samples. The grain size listed in each micrograph was measured via the linear intercept method.

Table 3: List of the grain size and pore density of each of the untested samples.

Eck Industries Sample Label	PNNL Label	Grain Size (µm)	Pore Areal Density (%)
A206-T6 Sand Cast With Chill	A	66.3 ± 13.2	0.30
A206N-T6 Sand Cast With Chill	D	47.1 ± 8.2	0.27
A206-T6 Sand Cast No Chill	B	72.2 ± 17.8	0.76
A206N-T6 Sand Cast No Chill	E	50.0 ± 6.5	0.28
A206-T6 PM	C	41.2 ± 4.4	0.41
A206N-T6 PM	F	59.4 ± 7.3	0.75

3.3.2 SEM Microstructural Analysis of Base Materials

Providing a thorough analysis of the base (uncorroded) microstructure is key to understanding both the mechanical and SCC response of these materials. Key features to be analyzed are the grain size, precipitate chemistry/density/microstructure, and grain boundary chemistry.

As all of the samples were of the same A206 alloy in the T6 condition, representative data analysis will be focused on a selected sample set (Permanent Mold) with the remainder of the data sets being referenced in an Appendix. Where applicable and directly comparable (e.g., grain size analysis from EBSD) data from all data sets will be provided.

3.3.2.1 Chemistry, Grain size analysis (EBSD), and Pore/Particle Analysis

Comparisons between each of the six samples for average chemistry, grain size and pore/particle analysis were performed using the Oxford AZtec program. EDS quantification of chemical maps across areas of 0.25 mm^2 representative regions was performed for each sample. EBSD was collected across representative areas in each sample to understand the grain size and orientation, whereas thresholding was used to calculate the areal densities of pores/precipitates within the material.

The A206 alloy is an Al-Cu alloy with Ti, Mn, Zn, and Fe comprising the remainder. The tensile bars were made from production baths whose chemistry was certified to meet the alloy specification. SEM-EDS suggested Zn concentration above the specification limit in each of the nano-containing samples, presumably from the manufacturing process used to produce the nano particles. The Ti, Mn, and Fe are primarily present in minor inclusions observed throughout the material, which will be demonstrated in detail later in this section. These observations illustrate there are no major compositional differences in these alloys except for the presence of relatively higher Zn in the nano samples.

EBSD analysis (Figure 18) is shown for all six A206-T6 samples, with tabulated average grain size provided in Table 4. The advantage of EBSD analysis (as compared to optical) is that the grain size is digitized based on the orientation of the grains and therefore is much more objective than would optical linear intercept method. For the sand cast samples (A, D, B and E) the presence of nano forming additives reduced the average grain size of the castings, although only the sand cast without chill samples were within a standard deviation of one another. The large standard deviation in the non-nano samples can be explained through the observation of a low density of much smaller grains noted throughout the alloy. Comparing the effect of the chill during the sand casting, the as received samples with chill exhibited smaller grains as would be expected due to the rapid cooling as compared to the sample cast without a chill. This difference in grain size is in contrast to the samples with nano additives where the average grain sizes were nearly identical.

As expected, the as-received permanent mold sample exhibited the smallest grain size, approximately 40% smaller than the average grain size of the sand cast samples, due to the rapid cooling rate in the metallic mold. Interestingly, the presence of nano forming additives did not have the intended effect of further reduction in grain size and the grains with nano particles were larger than in the sample cast without nano particles. It will be shown in the subsequent section on chemistry that this apparently opposite effect of nano particles is not an artifact. This suggests that for the nano additives, at a rapid enough cooling rate, the additives do not play a large role in controlling grain growth as compared to cooling rate. However, it is still unclear as to the mechanism of why the grains are larger with the nano addition.

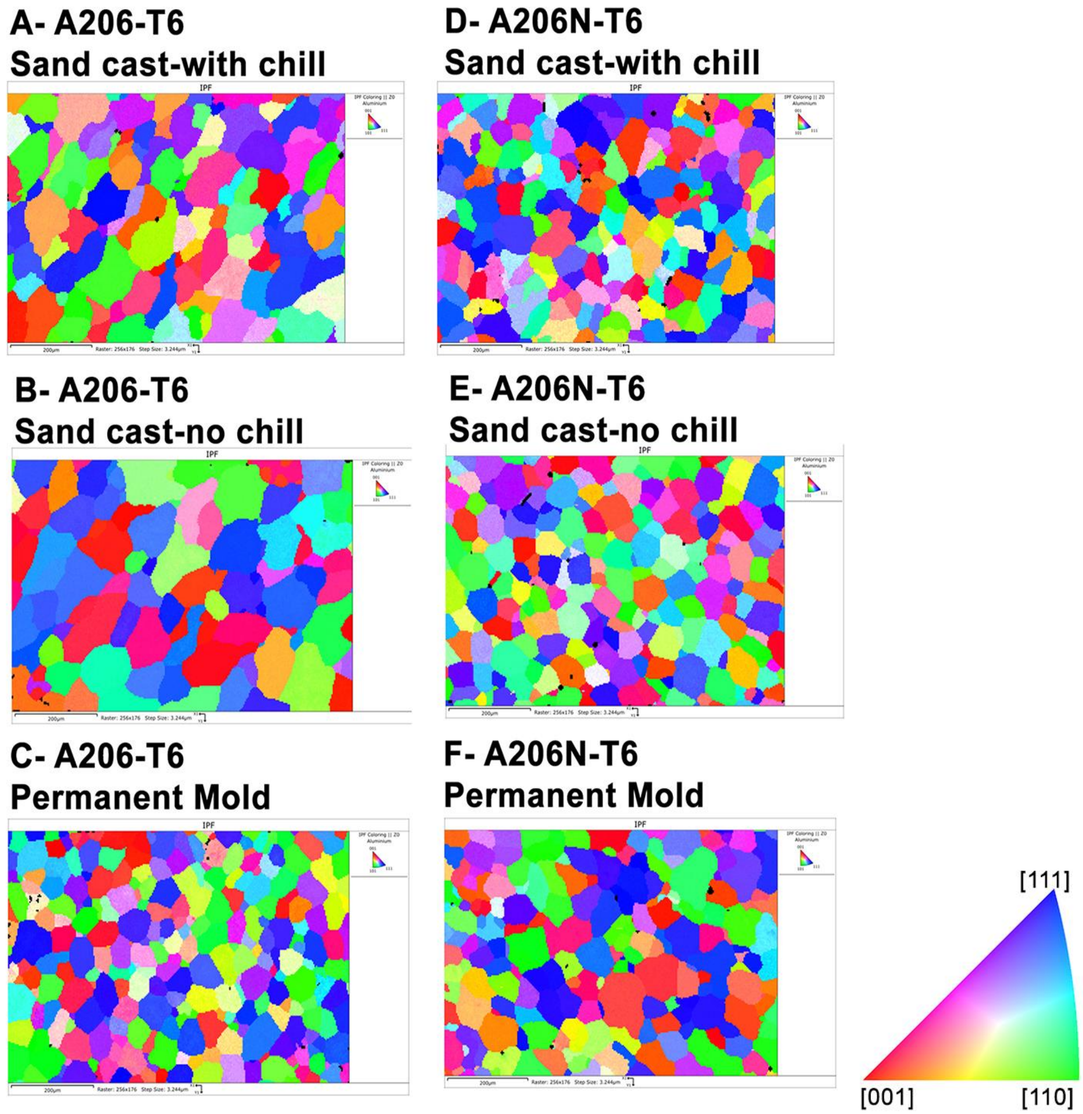

A- A206-T6
Sand cast-with chill

D- A206N-T6
Sand cast-with chill

B- A206-T6
Sand cast-no chill

E- A206N-T6
Sand cast-no chill

C- A206-T6
Permanent Mold

F- A206N-T6
Permanent Mold

Figure 18: EBSD analysis of untested samples. Grain size measurements are calculated from these data. The colors represent grain orientation, as indicated by the stereographic triangle.

Optical microscopy analysis of the samples, using Image J software, was utilized to understand the pore size as a result of the various casting conditions and nano additions. The Oxford AZtec software included on the JEOL IT800 can also perform similar analysis utilizing image contrast thresholding techniques such as in backscatter image or montage (Figure 19). Voids (red highlights in Figure 19) and precipitates (not shown) can be delineated from the surrounding matrix depending on the magnifications and SEM settings utilized. Due to voids' size being on the order of 100's of micrometers, a lower magnification was used for data collection in conjunction with an ~5 mm^2 collection area (Figures 20 and 22). For grain boundary precipitates (on the order of 10's of micrometers), a higher magnification/resolution was used with a collection area of ~1 mm^2 (Figures 20 and 22). Finally, for transgranular precipitation (on the order of micrometers) images were collected at the highest magnification across a few grains (Figures 21 and 23). The remainder of the data for the sand cast samples, with and without chill, are provided in the Appendix Figures 83-94. Data summarizing the pore and precipitate sizes (both grain boundary and transgranular) is presented in Tables 4 and 5.

The pore density and size increased in the presence of nano additives (Table 4), whereas the average pore size increased in the presence of nano additives for only the sand cast with chill and permanent mold samples. The sand cast without chill sample exhibited the largest pore size, which is visually corroborated by the global appearance of the pores in cross-section using optical microscopy (Appendix Figure 82). Pore size measurements were collected by both optical microscopy (lower resolution but larger analyzed area) and SEM (higher resolution but smaller analyzed area) to better understand the comparisons of both measurement techniques. Comparing the data in Table 3 and 4, the higher resolution of the SEM data can elucidate the actual pore size. For example, it demonstrates that in all cases, in the presence of nano additives, the pore areal density increases. Future work should concentrate on larger data sets collected in the SEM instead of utilizing more rapid optical microscopy data collections.

SEM analysis was also utilized to examine precipitate density as a function of sample type (Table 5). The areal density and average size of grain boundary precipitates for each of the casting types increased in the presence of nano additives. In contrast, the areal density of transgranular precipitates decreased in the presence of nano additives for all casting types. The average size of the transgranular precipitates was approximately the same across all casting types, with and without nano additives. Figures 21 and 23 indicate that the centers of the grains often show a deficit of transgranular precipitates commensurate with a measurably brighter matrix contrast. The contrast often has a dendritic morphology (e.g., Figure 23). Brighter contrast in BSE imaging (Figure 24) suggests chemical segregation and the dendritic morphology indicates a cooling rate effect. Chemical mapping of this feature indicates that an enrichment of Ti (Figure 25) which prohibits the nucleation of the fine, transgranular Al_2Cu. Quantification of these grain interiors as compared to the regions with Al_2Cu precipitates shows that there is ~1 wt.% Ti in the regions without precipitates (bright central regions) as compared to absence of Ti in the regions with precipitates.

These data suggest that while the incorporation of nano additives affects the areal density of both grain boundary and transgranular precipitates, it only affects the size of grain boundary precipitates. This is intuitive because the size of the precipitates formed in the grain interiors is dictated by the local chemistry and nucleate out of the matrix, whereas the formation of grain boundary precipitates is greatly affected by grain size and grain growth during casting.

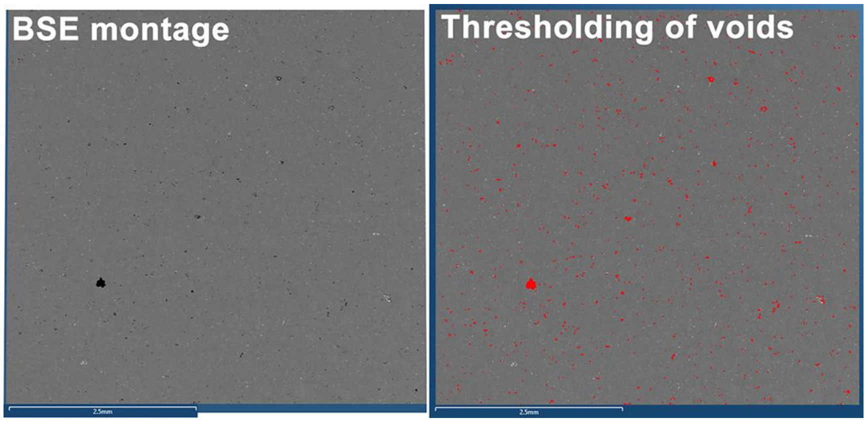

Figure 19: Example SEM data demonstrating how Feature analysis operates by utilizing thresholding operations to determine void density. An areal density of the red areas can then be calculated to determine the characteristic of the desire feature (e.g., voids, precipitates).

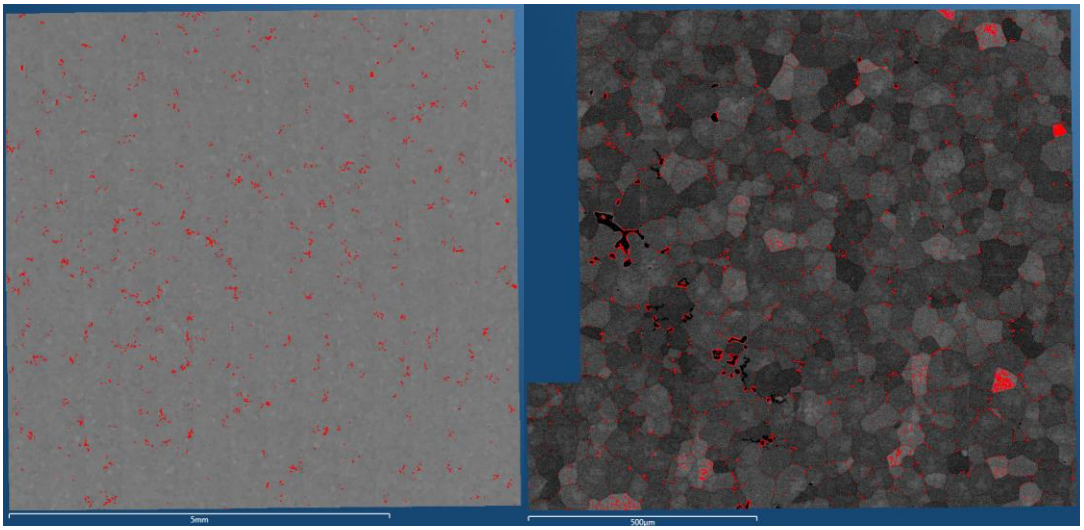

Figure 20: SEM(BSE) void (left) and grain boundary precipitate (right) Feature analysis of the permanent mold sample. Thresholding of the contrast indicates desired features in the sample (red areas).

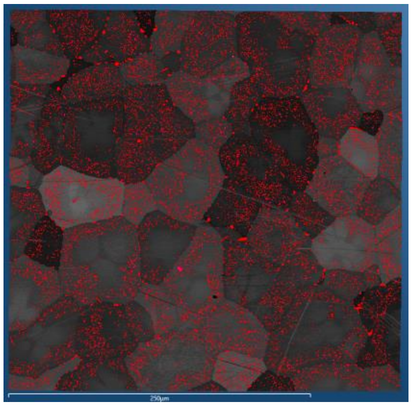

Figure 21: SEM(BSE) transgranular precipitate feature analysis of the permanent mold sample. Thresholding of the contrast indicates transgranular precipitates in the sample (red areas). Note how most of the grain interiors are devoid of precipitates.

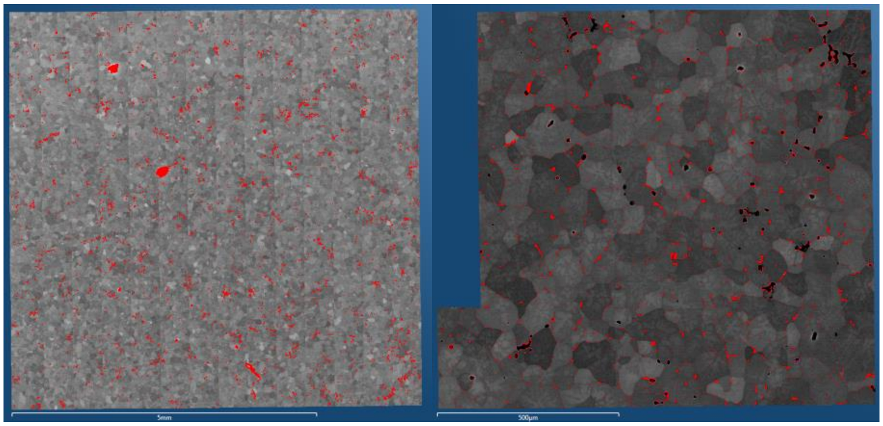

Figure 22: SEM(BSE) void (left) and grain boundary precipitate (right) feature analysis of the permanent mold nano sample. Thresholding of the contrast indicates desired features in the sample (red areas).

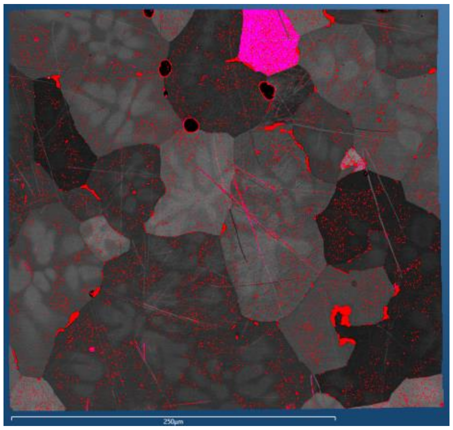

Figure 23: SEM(BSE) transgranular precipitate feature analysis of the permanent mold nano sample. Thresholding of the contrast indicates transgranular precipitates in the sample (red areas). Large magenta area (top) is where orientation contrast (bright grain contrast) was automatically collected as part of the thresholding. These areas that were not counted are part of the precipitate statistics.

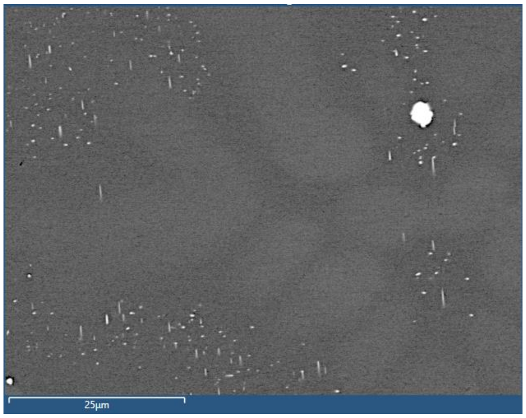

Figure 24: SEM(BSE) of the grain interior of the permanent mold nano sample showing chemical partitioning (faint bright areas) in the center of the grain with the absence of transgranular Al_2Cu. This suggests the higher Z material in this region prohibits nucleation.

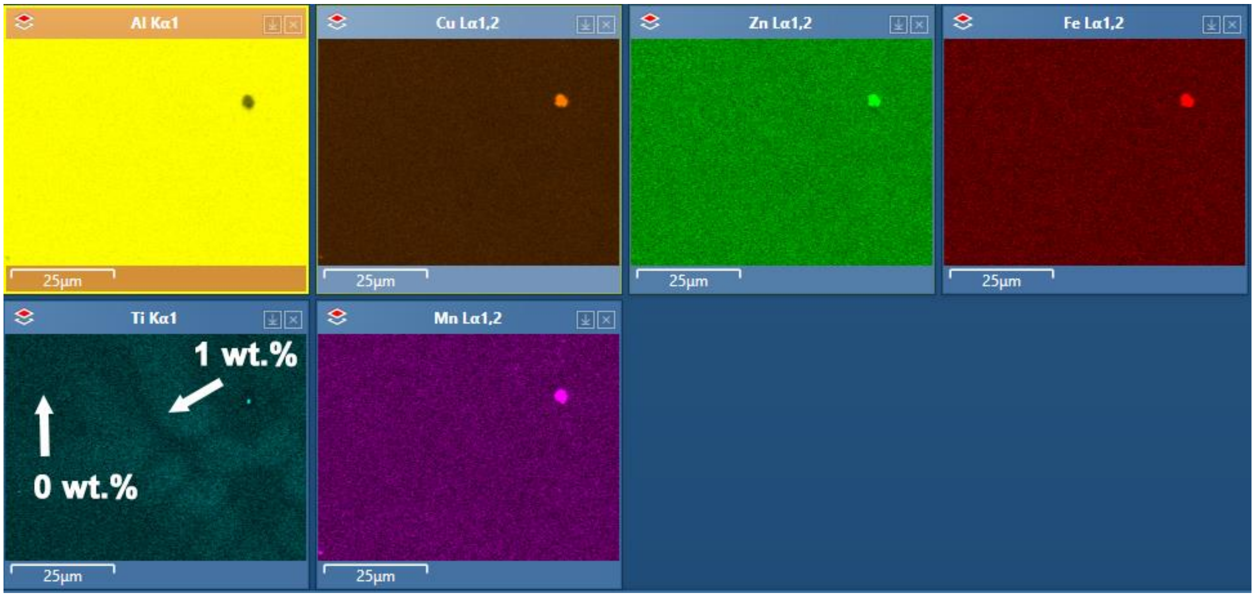

Figure 25: SEM(EDS) elemental maps of the region provided in Figure 24 highlighting the bright regions in the grain interior are Ti rich. Note that the resolution and accelerating voltage (10 kV) used for mapping precludes the identification of the transgranular Al_2Cu (which are observed as small, linear features in Figure 24).

Table 4: List of the grain size and pore characteristics of each sample measured by SEM.

Eck Industries Sample Label	**PNNL Label**	**Grain Size (µm) EBSD**	**Pore Areal Density (%)**	**# pores**	**Average pore area (um^2)**
A206-T6 Sand Cast With Chill	A	63.3 ± 13.3	0.19	1879	44.1
A206N-T6 Sand Cast With Chill	D	48.3 ± 2.4	0.40	2430	74.8
A206-T6 Sand Cast No Chill	B	74.1 ± 14.2	0.45	1628	123.5
A206N-T6 Sand Cast No Chill	E	47.5 ± 2.1	0.73	3191	102.5
A206-T6 PM	C	43.4 ± 6.0	0.30	1587	84.6
A206N-T6 PM	F	55.3 ± 3.0	0.85	3384	110.9

Table 5: List of the grain boundary (GB) and transgranular precipitate characteristics of each sample measured by SEM.

Eck Industries Sample Label	**PNNL Label**	**GB Precipitate Areal Density (%)**	**GB Precipitate Average Size (um^2)**	**Transgranular Precipitate Areal Density (%)**	**Transgranular Precipitate Average Area (um^2)**
A206-T6 Sand Cast With Chill	A	0.37	0.77	0.66	0.05
A206N-T6 Sand Cast With Chill	D	0.40	1.56	0.27	0.04
A206-T6 Sand Cast No Chill	B	0.43	1.08	0.51	0.04
A206N-T6 Sand Cast No Chill	E	1.01	2.70	0.42	0.04
A206-T6 PM	C	0.16	1.07	1.26	0.05
A206N-T6 PM	F	0.54	2.45	0.28	0.04

3.3.2.2 SEM: Permanent Mold (C,F)

SEM microstructural examinations were performed for all six sample conditions, with the detailed data analysis from the permanent mold samples being presented in Figures 26-31 and the remaining data layups from the additional four samples presented in the Appendix Figures 95-114. As noted in the previous section, the densities of both the inter- and transgranular precipitates can vary among samples due to different casting conditions. Since the types and appearance are inherent to the A206 alloy in the T6 condition, only the permanent mold samples will be highlighted in detail. These examinations will detail the overall microstructure as it relates to precipitate size, morphology, and chemistry, focusing on the differences between the nano and non-nano samples in the as-received condition.

The overall chemistry of the matrix can be observed in Figures 27 (non-nano) and 30 (nano additive). The chemistry across the matrix appears to be uniform for each sample except for the appearance of clustering of the Ti signal in small domains on the order of 10s of micrometers in both the non-nano and nano samples. Higher magnification of these clusters is shown in Figures 28 (non-nano) and Figure 31 (nano additives), of which the Ti signal appears as partially round domains within each grain. These domains were not expressed within any BSE images, suggesting that they are in solid solution with the matrix and are not fine precipitates.

Varying magnifications (from lowest to highest) were collected for both the non-nano PM sample (Figure 26) and the PM with nano additives (Figure 29). In both samples there appear to be long and thin precipitates on the grain boundaries exhibiting high aspect ratios. Chemical analysis of these precipitates shows that they are comprised of mainly Al, Mn, Fe, and Cu in the non-nano sample (Figure 28) and in the nano additives sample (Figure 31) the same elements are present plus the addition of Zn. This observation is consistent across the remaining four sand cast samples as shown in the Appendix Figures 95-114.

At higher magnifications, populations of transgranular, oriented precipitates are noted throughout the matrix of each cast sample. The orientation relationship with the matrix can be most easily noted in Figure 26 at higher magnifications where the small, platelike precipitates on the order of 100’s of nm are oriented at 90° to one another with the same matrix. It is important to note that depending on the orientation of the grain and the expressed cross-sectional plane, these precipitates might not always appear in projection with orthogonal orientations but are still oriented. Again, as noted in the previous section where more detailed statistics were collected on population densities and areal coverage, comparing Figures 26 and 29 it suggests that for the PM nano additives sample there is a lower density of transgranular precipitates. The dimensions of these precipitates prohibit chemical analysis at this length scale and will be highlighted in subsequent TEM sections.

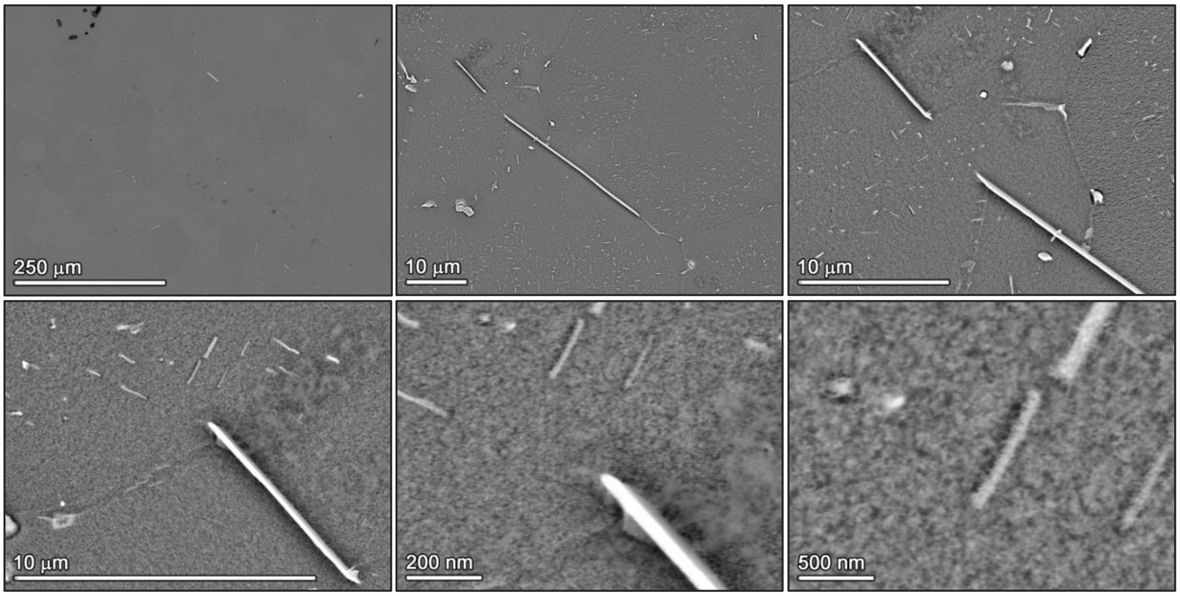

Figure 26: SEM(BSE) images of the representative microstrucuture of the PM sample at succcesively higher magnifications.

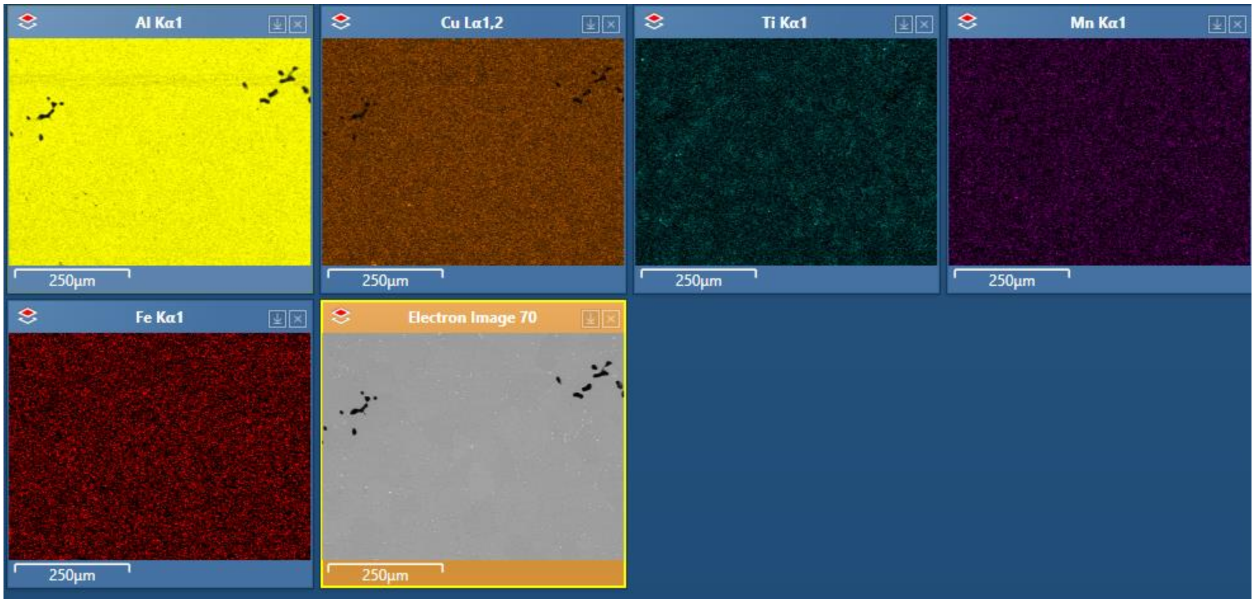

Figure 27: SEM(BSE) image and EDS elemental maps of the representative microstrucuture of the PM sample.

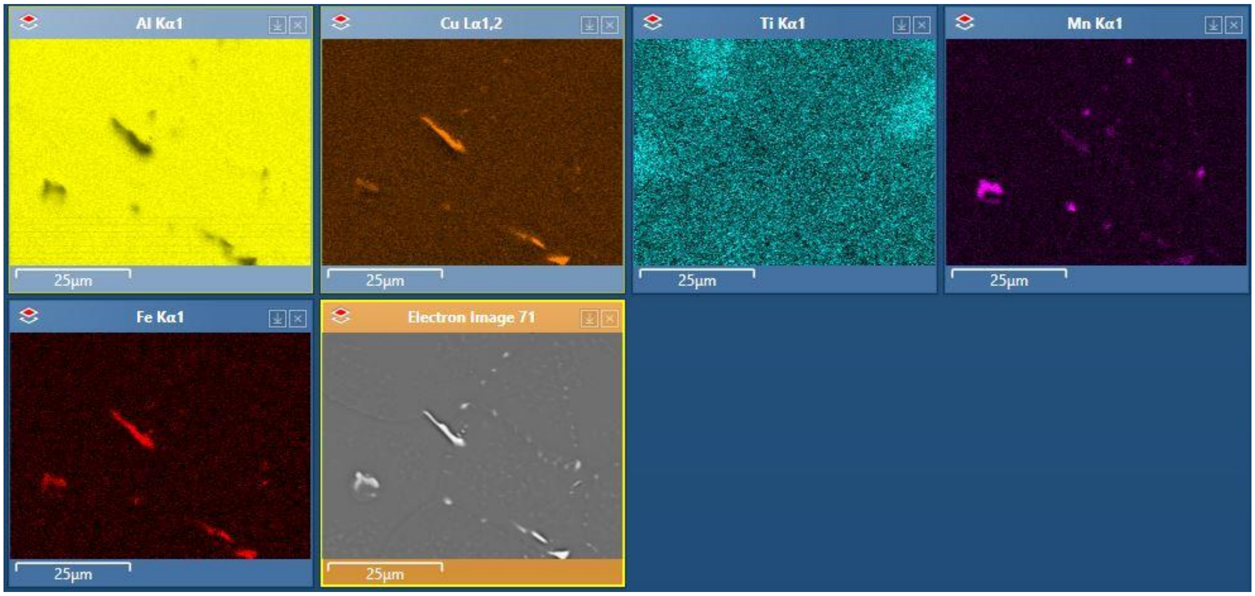

Figure 28: SEM(BSE) image and EDS elemental maps of the representative microstrucuture of the PM sample.

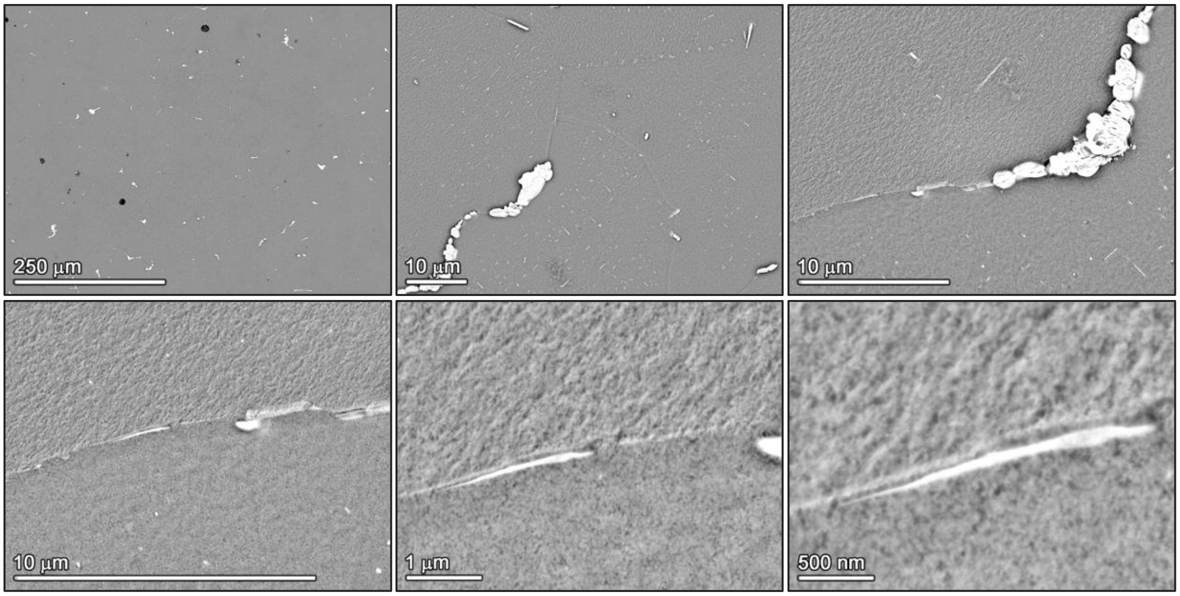

Figure 29: SEM(BSE) images of the representative microstrucuture of the PM nano sample.

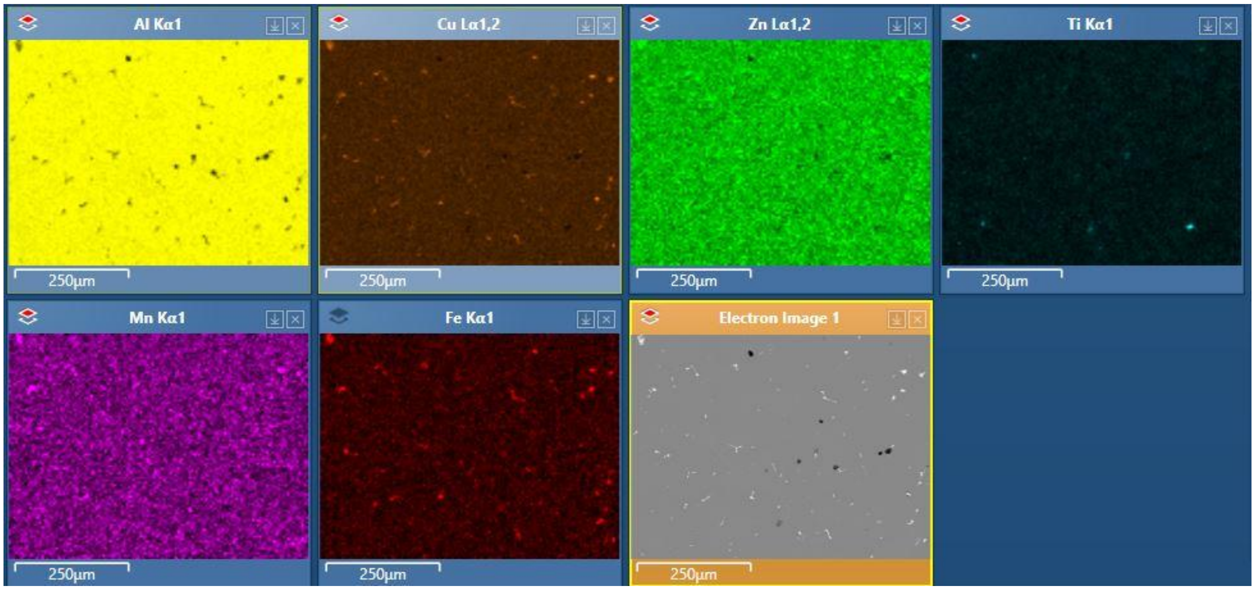

Figure 30: SEM(BSE) image and EDS elemental maps of the representative microstrucuture of the PM nano sample.

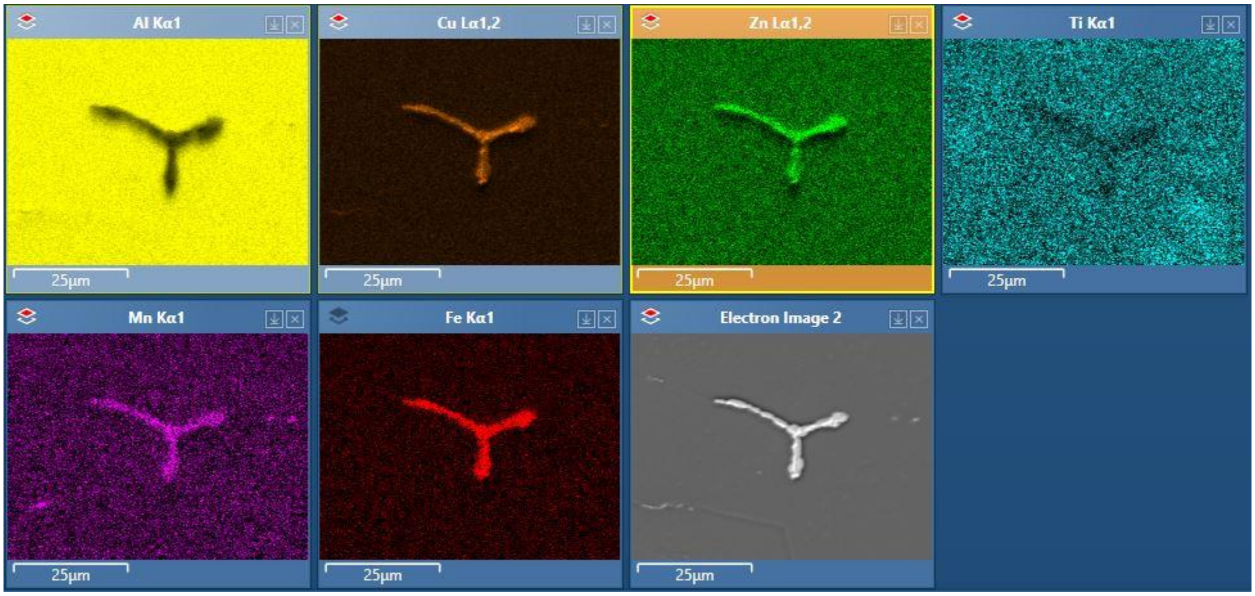

Figure 31: SEM(BSE) image and EDS elemental maps of the representative microstrucuture of the PM nano sample.

3.3.2.3 Scanning Transmission Electron Microscopy (S/TEM): Permanent Mold (C,F)

S/TEM analysis was performed on all six sample conditions. Detailed analysis of the permanent mold specimens (C-as received and F-nano) is presented below.

Figure 32 shows a grain boundary in each of the PM cast samples. It is immediately discernable that both GB precipitates and transgranular precipitates have a finer dispersion in the PM nano specimen. The image of the PM nano sample (Figure 32b) in particular highlights that precipitate distributions are not homogenous throughout the sample. A similar trend can be observed for all casting conditions.

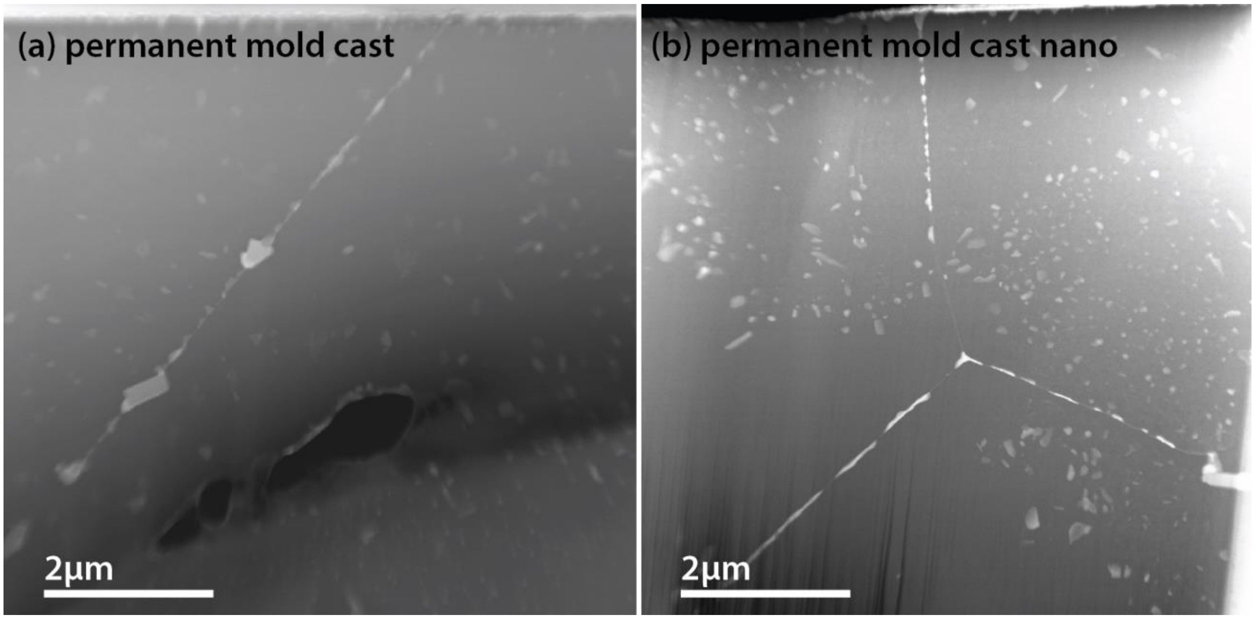

Figure 32: High-angle annular dark field (HAADF) images of (a) permanent mold cast (sample C) and (b) permanent mold cast nano (sample F) samples.

STEM EDS data for the as-received sample (sample C) is shown in Figure 33 and Figure 35. Figure 33 shows GB precipitates containing Ti, Mn, Fe, and Cu. All specimens exhibited Cu precipitates with 2 different compositions at the GB. However, the sand cast sample with chill additionally only shows one Ti-rich precipitate in the analysis region and the sand cast sample with chill had one, albeit rather large (~800 nm), Fe-Mn-Cu-precipitate at the grain boundary in the analysis region.

Figure 35 illustrates precipitates are 100-200 nm in the PM cast sample. The largest particle is a Fe-Mn-Cu-precipitate surrounded by Cu-rich precipitates of two distinctly different compositions. A Ti-rich precipitate is also detected. This precipitate appears to be free of Cu and Al. The EDS data suggests a metallic Ti precipitate, no significant N or C signal was detected.

Figure 34 shows a line profile across the GB region. While it was attempted to observe a precipitate-free region of the GB, however the GB appeared to be lined with nano Cu-rich precipitates between larger ones, resulting in the double peak in the Cu signal in the line profile. Unique to this sample is a striking narrow enrichment of Mg in the GB region.

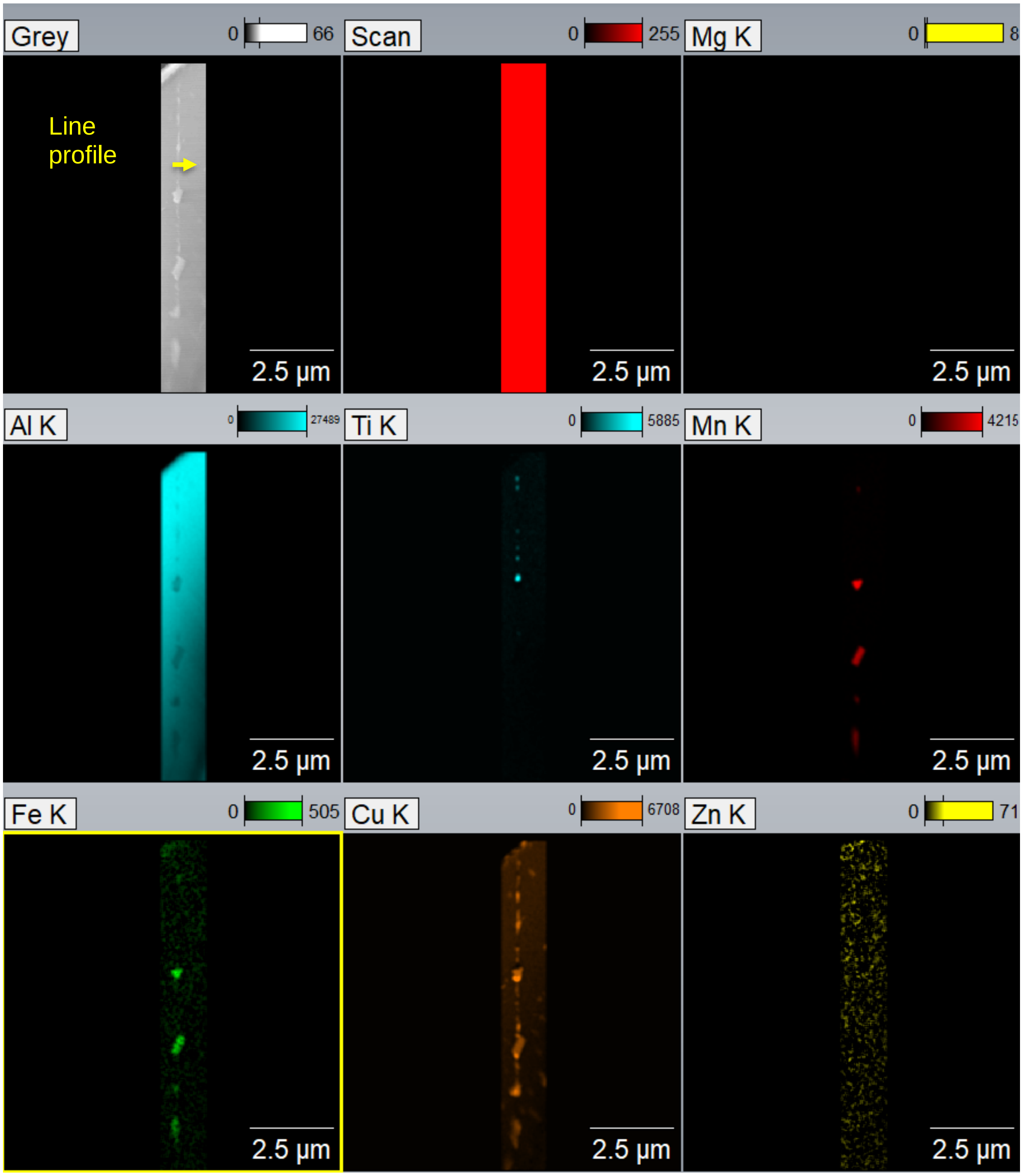

Figure 33: STEM EDS analysis of a grain boundary in the permanent mold cast sample (sample C).

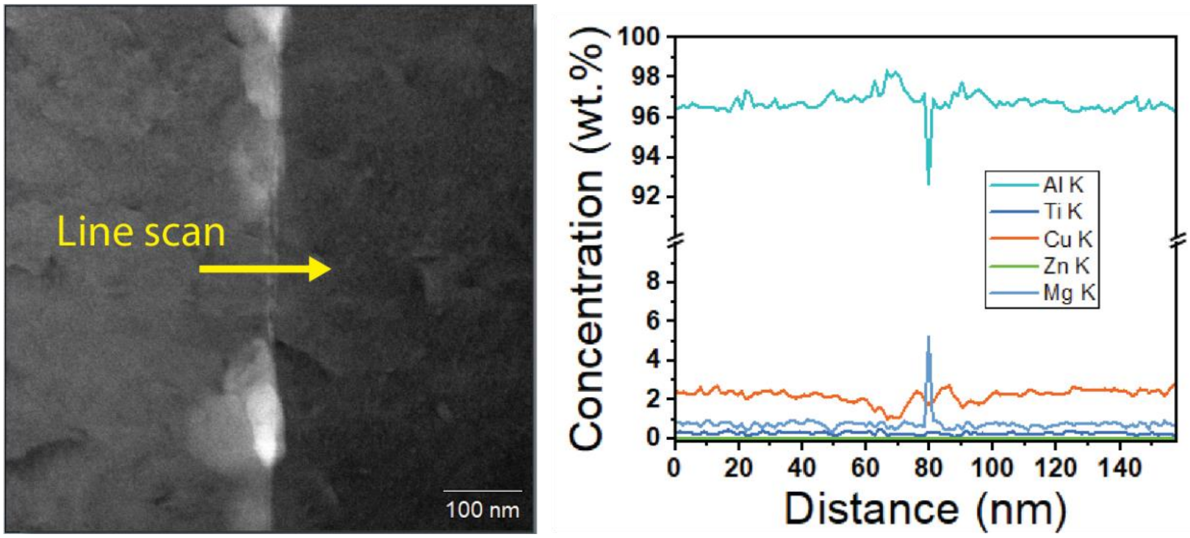

Figure 34: Line scan across grain boundary in permanent mold cast sample (sample C) marked in Figure 33.

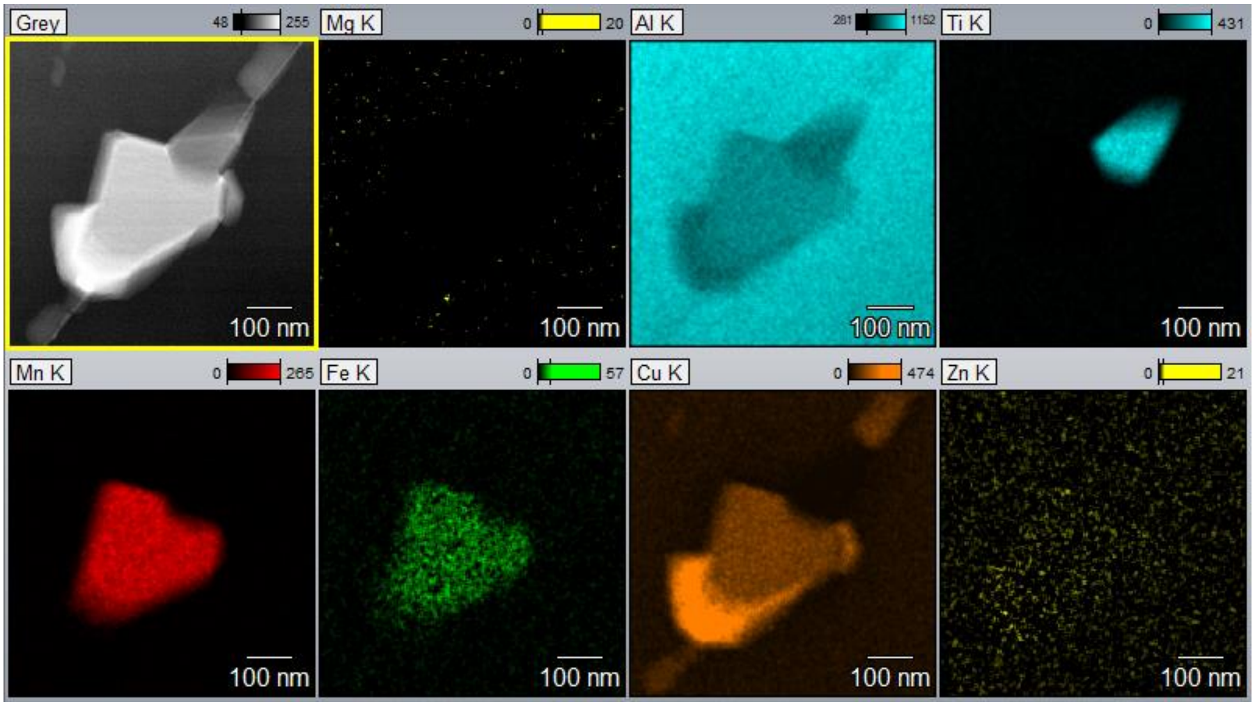

Figure 35: STEM EDS is showing Fe-Mn-Cu-precipitates, Ti-rich precipitates, and Cu-rich precipitates in the permanent mold cast sample (sample C).

STEM EDS data of grain boundaries in the PM cast nano sample is shown in Figure 36 and Figure 38. Figure 36 shows that the grain boundaries are dominated by fine Cu-rich precipitates. There was only one Fe-Mn-Cu-precipitate at a GB at the very edge of the analysis region. It is shown in Figure 38.

Figure 37 shows a line profile across the grain boundary as marked in Figure 36. The GB is slightly depleted of Cu. Slight Ti enrichment was observed over a width of several 100s of nanometers. The profile looks almost exactly reverse to the Ti profile in the sand cast sample with no chill nano (sample E). Sample E also exhibited a higher matrix concentration of Ti and many Ti-rich GB precipitates, which were absent from the permanent mold cast nano sample (sample F).

The overview image in Figure 32 already revealed the gross inhomogeneity of the precipitate distribution. Figure 39 shows some larger precipitates at the edge of the TEM foil. Rod-like Fe-Mn-Cu precipitates can be up to a micron long. Many Cu-rich intergranular precipitates are also present.

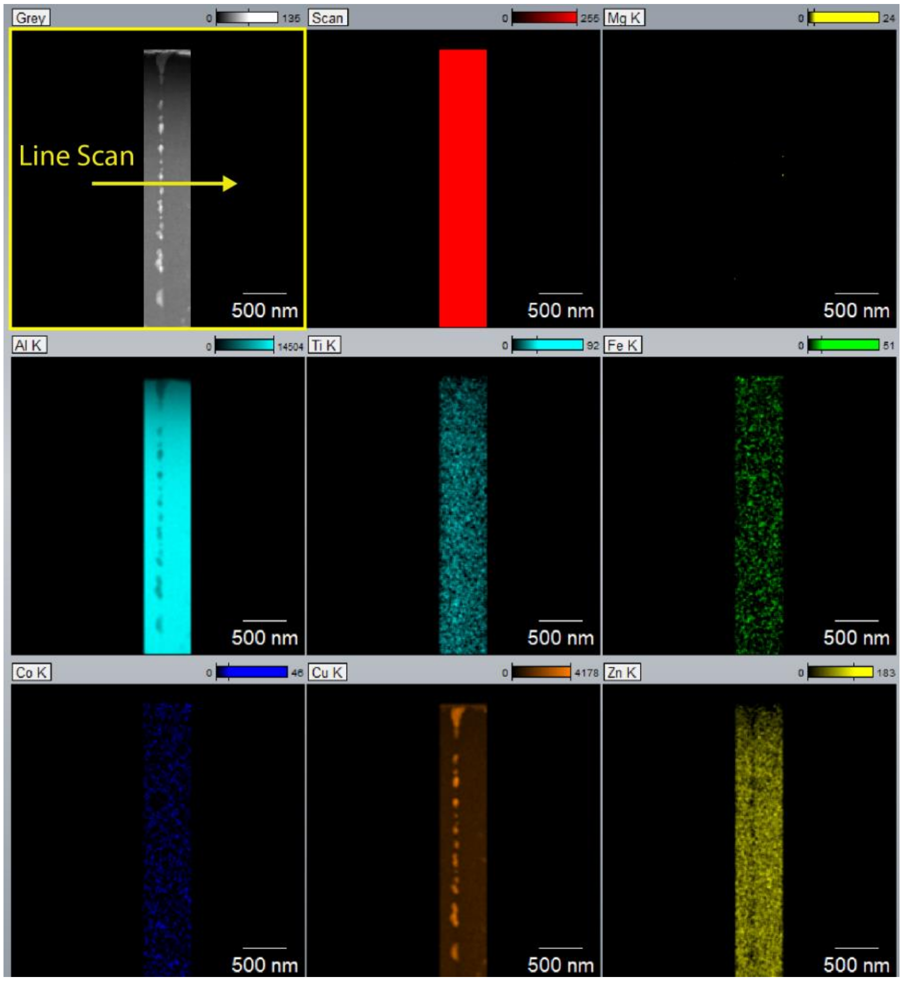

Figure 36: STEM EDS data of the permanent mold cast nano sample (sample F) showing the grain boundary region.

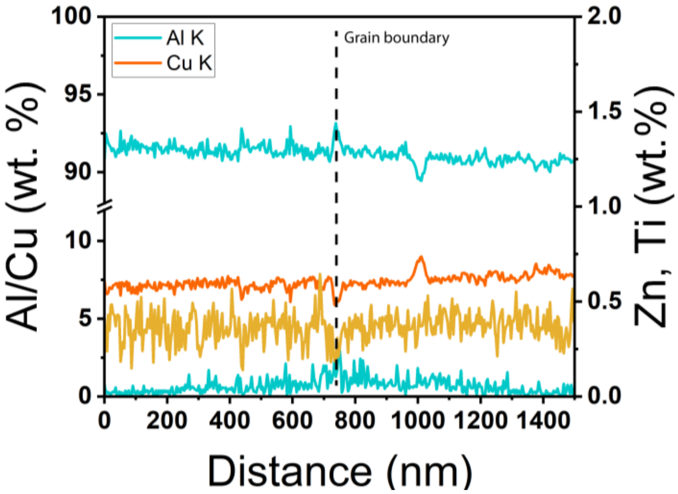

Figure 37: STEM EDS line profile across a grain boundary (marked in Figure 36) in the permanent mold cast nano sample (sample F).

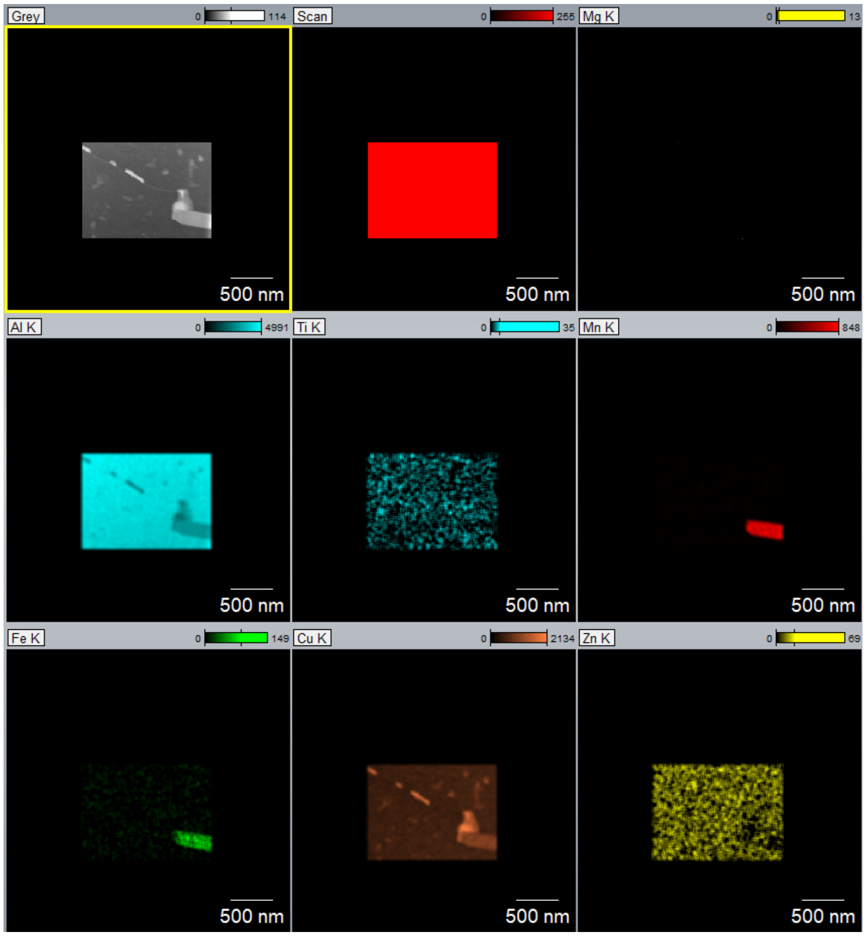

Figure 38: STEM EDS of a Fe-Mn-Cu precipitate at a GB in the permanent mold cast nano sample (sample F).

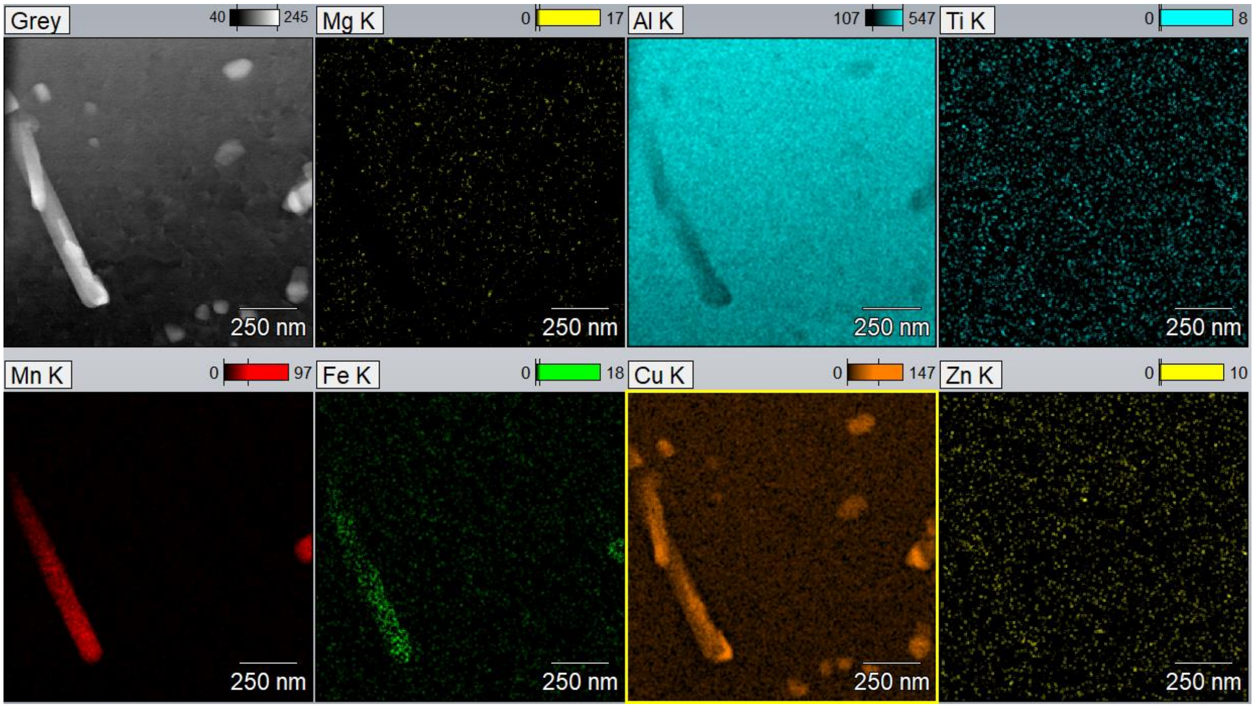

Figure 39: STEM EDS of intragranular precipitates in the permanent mold cast sample nano (sample F).

3.3.3 Microstructural Analysis- Post Corrosion Testing:

After SCC and tensile testing (detailed in Sections 3.1 and 3.2, respectively), the gauge of the dog bone samples was cross-sectioned adjacent to the fracture surface of each of the six samples. Data for each sample is highlighted for the permanent mold samples in Figures 40-47 with the remainder of the sand cast samples shown in the Appendix Figures 124-139. As noted in previous sections, because of the similar SCC microstructural observations between each of the A206-T6 alloys, only the permanent mold samples will be discussed in detail, with comparisons being made between the non-nano and nano additive samples.

From the SEM cross-sections of the SCC tested alloys, sharp SCC leading crack tips were identified. TEM analysis of a single leading crack tip from the permanent mold non-nano sample was performed as part of Milestone 2. Examinations of the oxide structure at the leading crack tip provide valuable insight into how the grain boundaries are affected during the SCC testing. Details of the SCC cracking morphology and chemistry will first be shown at lower magnifications in SEM and then discussed in higher detail in a TEM section.

3.3.3.1 SEM: Permanent Mold (C,F)

From the cross-sections of all the various casting types, there were three distinct features that were identified with respect to corrosion response. 1) The exterior/surface corrosion, which consisted of varying morphologies ranging from thin films to larger, micrometer-sized oxides; 2) Corroded pore structures that were a result of the as-cast pore structures (e.g., Figures 16 and 19) intersecting the surface, leading to rapid corrosion that filled each pore; and 3) Sharp SCC, intergranular cracks that were filled with oxide and were observed up to 100s of micrometers from the surface towards the center of the dog bone cross-section. The major difference between the non-nano and nano additive samples was the presence of Zn in the oxide on the outer surfaces of the latter. The following data will be used to highlight each of the noted features.

The exterior of the gauge section is the most exposed surface of the alloy, being in cyclic contact with the saltwater solution, and is expected to express the thickest oxide layers. Depending on the regions observed, one of two oxide morphologies was noted. The first being a thin, continuous film on the order of a few micrometers as seen in Figures 41 and 42. In the uncorroded condition, this appears to be aluminum oxide. In the nano additives sample, the same oxide is observed, but with the presence of Zn noted throughout the oxide (Figures 46-47). In addition to the thin, continuous oxide, larger aluminum rich oxides on the order of 10’s of micrometers were also noted (e.g., Figure 40). Like the thin, continuous films, in the nano additives sample, Zn was also noted in these oxides (Figure 46). There was no apparent microstructural reason for the thin, continuous oxide as compared to the thicker oxides and further study is needed to determine the root cause. Figure 40 (right image) shows bright precipitates adjacent to a larger oxide. Not all larger deposits show similar behaviors.

As shown previously, the casting process inherently leaves porosity throughout the casting. Therefore, it is very probable that some of these pores intersect with the surface of the dog bone specimen and allow water ingress during the SCC testing. In all of the A206-T6 samples the pores that intersected the surface were filled with aluminum oxide (e.g., Figures 40 and 44), of which the large oxides throughout the pore volume were cracked.

Lastly, and more pertinent to the SCC response are the sharp, intergranular SCC cracks observed extending up to hundreds of micrometers from the exterior of the sample (Figures 41 and 45). These sharp cracks can originate from the surface or at the ends of pores. After some time, longer cracks can open as the sample is stressed, but almost always the active cracks will be sharp and may not even show oxides at this level of observation. The reason is that grain boundaries are active and will react with the chloride solution to quickly promote corrosion. The stress of the sample being cyclically dried and dipped into solution can provide enough stress to exacerbate the crack growth. Some crack tips, as seen in Figure 41, can be blunted. This is suggestive of a crack that may have either encountered a precipitate or the stress levels were low enough that the crack growth was arrested. EDS analysis of the same crack tip (Figure 43) shows no indication of a remnant precipitate chemistry and only shows aluminum oxide, but the shape of the oxide is suggestive of a prior precipitate. This could mean that the crack persisted long enough to fully corrode the precipitate it encountered. Shorter cracks, such as the one shown in Figure 47 show that if the crack is actively growing, it will circumvent the Cu rich, grain boundary precipitate. Since this is a shorter crack, it may not have had time to fully corrode the grain boundary precipitate.

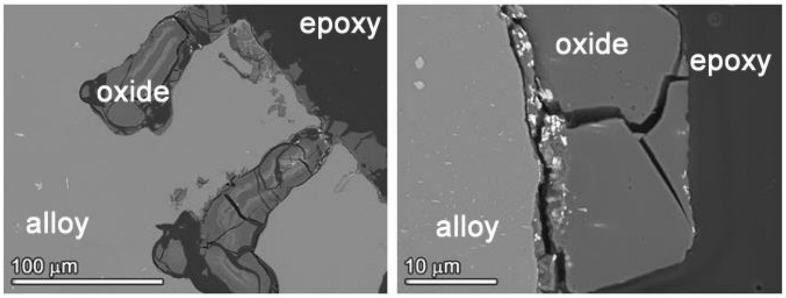

Figure 40: SEM(BSE) micrographs showing general surface corrosion of the PM sample.

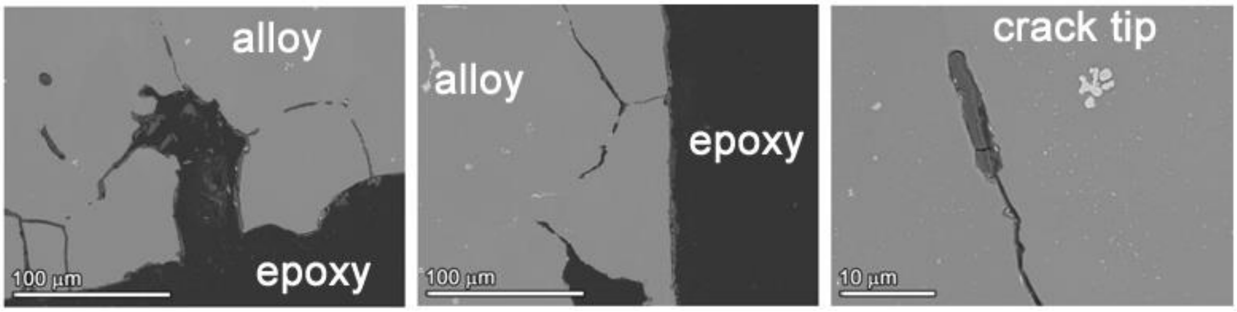

Figure 41: SEM(BSE) micrographs showing SCC cracking of the PM sample.

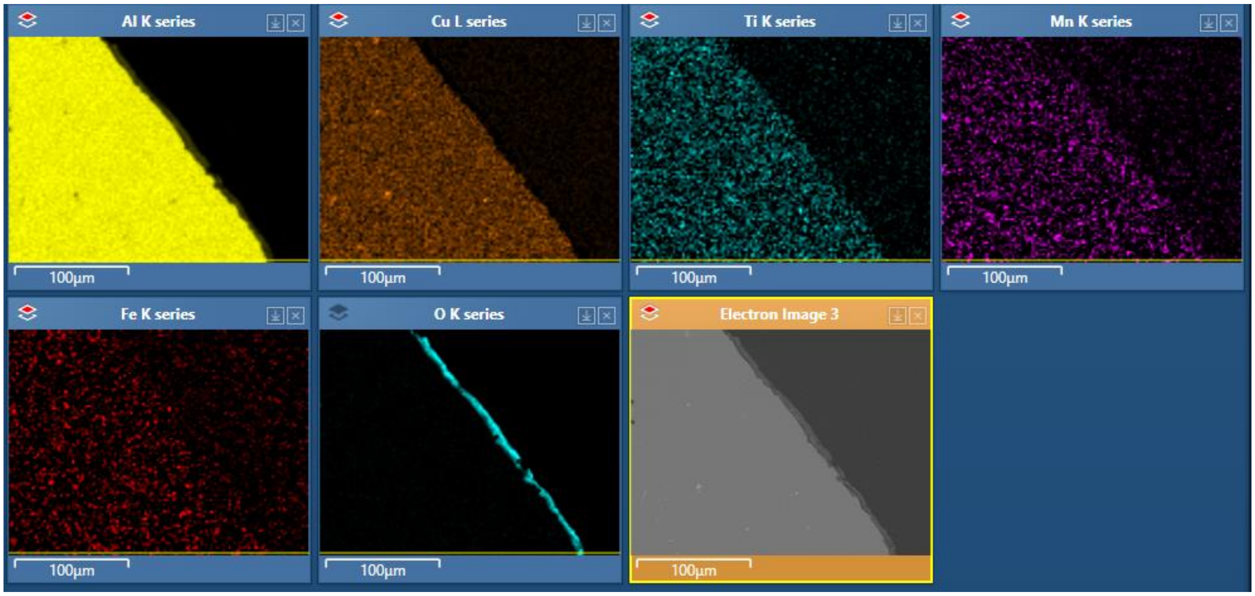

Figure 42: SEM(BSE) and EDS elemental maps of the corrosion surface of PM sample.

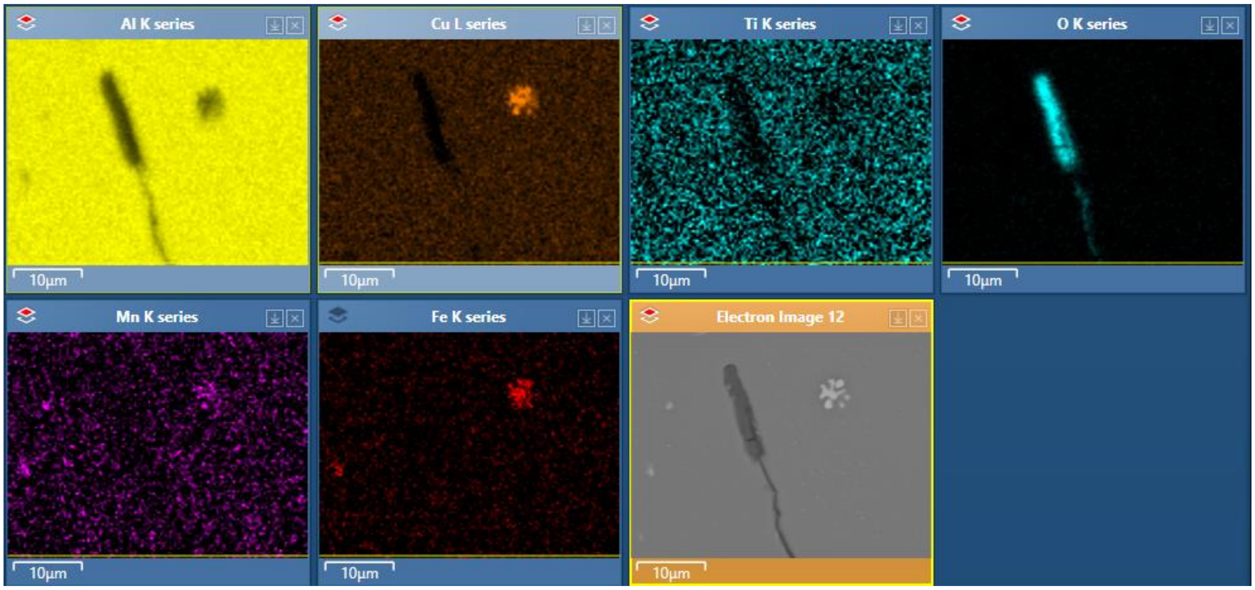

Figure 43: SEM(BSE) and EDS elemental maps of corrosion microstructures of PM sample.

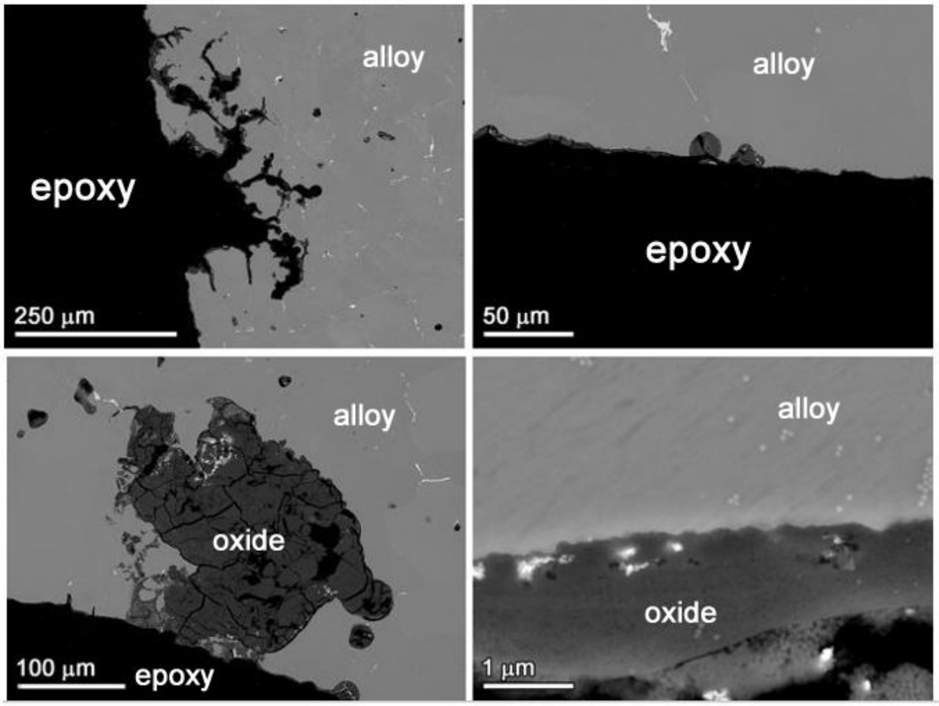

Figure 44: SEM(BSE) micrographs showing general surface corrosion of the PM nano sample.

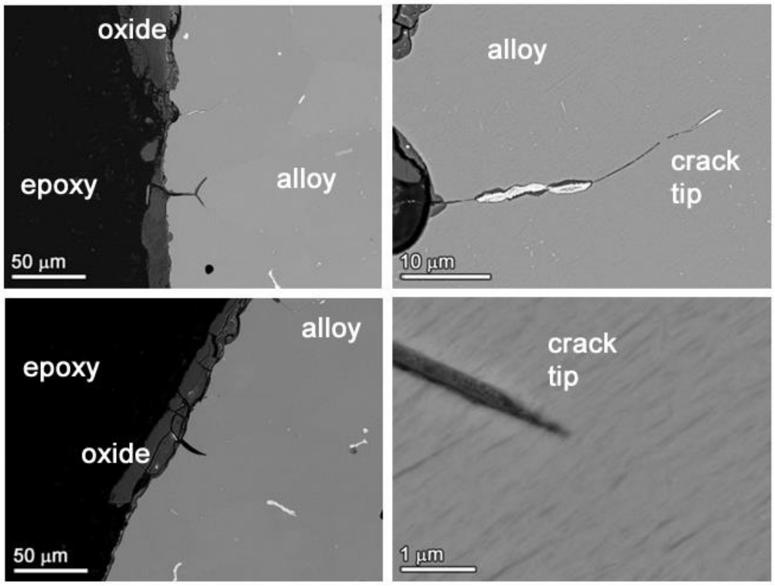

Figure 45: SEM(BSE) micrographs showing SCC cracking of the PM nano sample.

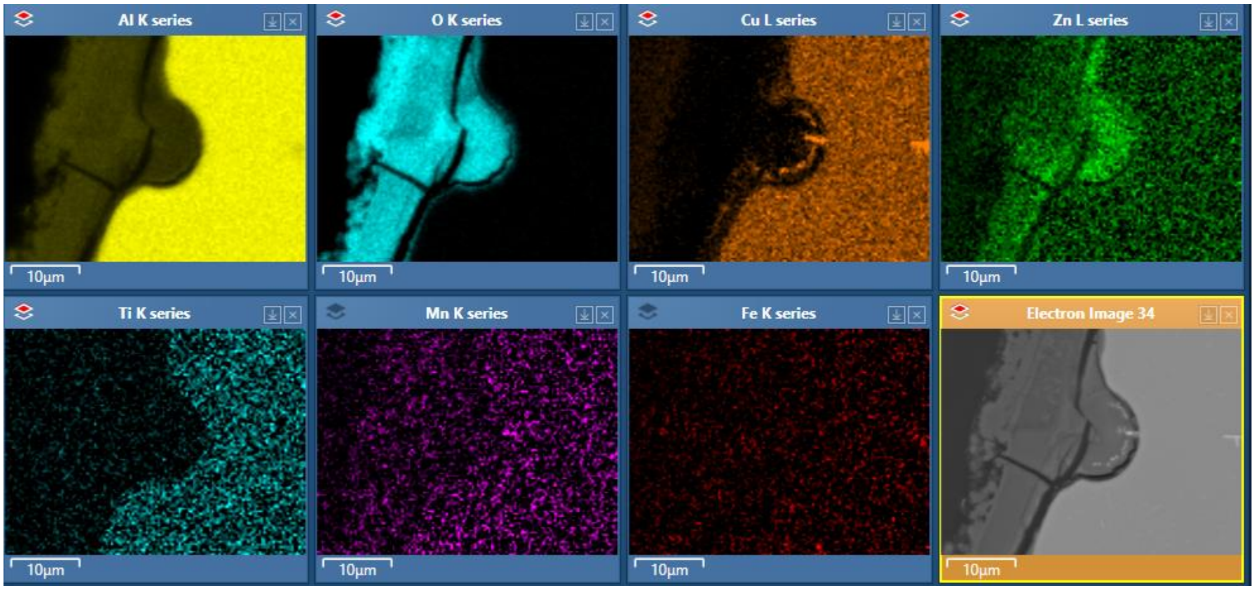

Figure 46: SEM(BSE) and EDS elemental maps of the corrosion surface of PM nano sample.

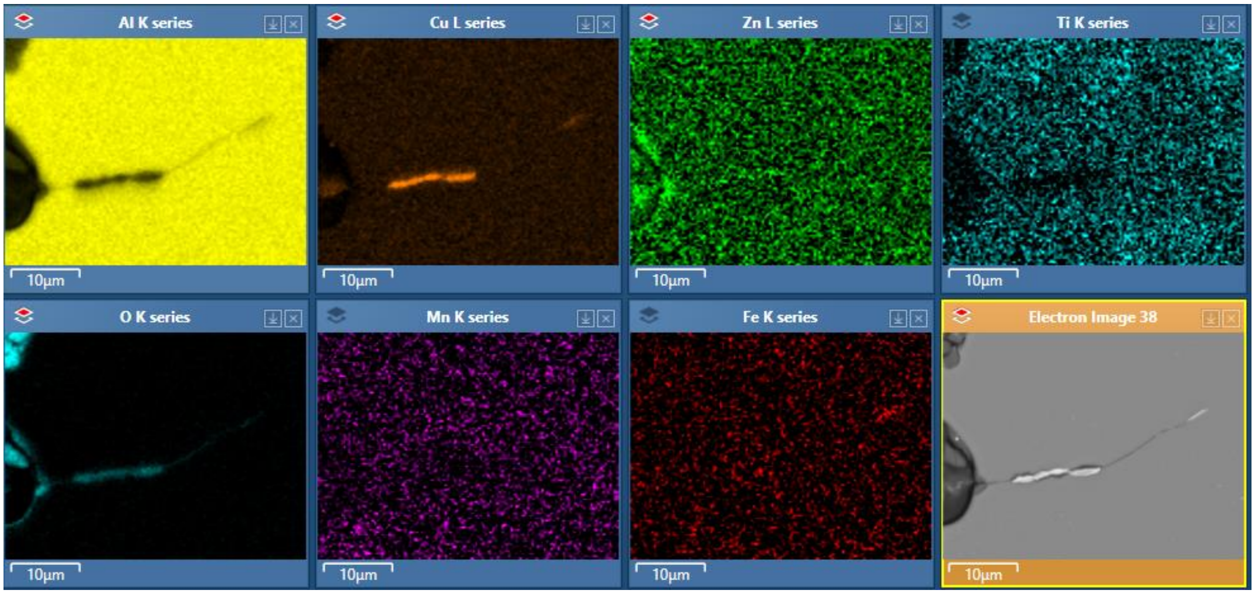

Figure 47: SEM(BSE) and EDS elemental maps of SCC cracks in the PM nano sample.

3.3.3.2 S/TEM: Permanent Mold As-Received I Corroded Sample

Sharp SCC cracks observed in the SEM can only be examined to a certain level, especially when performing chemical analyses. As part of Milestone 3 to better understand the SCC behavior at the nanometer level, a TEM sample was prepared from the permanent mold as-received sample (Figure 48) that was approximately 45 µm from the surface.

A cross-section of the FIB lift-out at various magnifications is shown in Figure 49. At low magnifications, the ordered, transgranular precipitates are shown. At higher magnifications the cross-section of the SCC crack can be observed. In the middle frame, the crack is noted traveling around the brighter, intergranular precipitates, and at the highest magnification the crack is ~50 nm wide and is filled with a continuous, solid oxide.

Chemical mapping performed at various magnifications (Figures 50 and 51) provides a clear indication of the chemistry of not only the intergranular precipitates (Al_2Cu) but also the oxide which consists of mainly alumina, but also has traces of Cl and S. The presence of Cl demonstrates the affinity for the saltwater solution to degrade the grain boundaries. The crack is ~50 nm wide and the presence of oxide and Cl for water at room temperature shows how quickly SCC can occur during these time scales. Figure 51 shows two distinct regions of the SCC crack, one circumventing transgranular precipitates and the other in a region with no precipitates. The oxide appears to be surrounding the intergranular Al_2Cu precipitates, with a faint trace of Mg being observed inside the particles. In the second instance, Al_2Cu precipitates are located near the grain boundary, but they are most likely transgranular precipitates that nucleated adjacent to the boundary. In this case, the continuous aluminum oxide is seen as a narrow channel complimented by a Cl signal. This suggests rapid corrosion during cracking (i.e., the crack does not have time to corrode into the surrounding matrix). Chemical mapping of these regions at various magnifications are shown in Figures 50 and 51.

Lastly, as shown in the SEM data, larger, rounded precipitates with Fe and Mn content were observed throughout the matrix. Atomic column crystallographic analysis of these precipitates indicates that they are alpha $Al_{201.593}Fe_{42.4416}Mn_{10.6104}$ (Figure 52). The unique atomic column pattern shown by the crystal in the <111> orientation helped to identify the 250 nm particle. While these do not constitute a larger fraction of the precipitates in these alloys, it is good to be able to identify their presence through these advanced analytical methods.

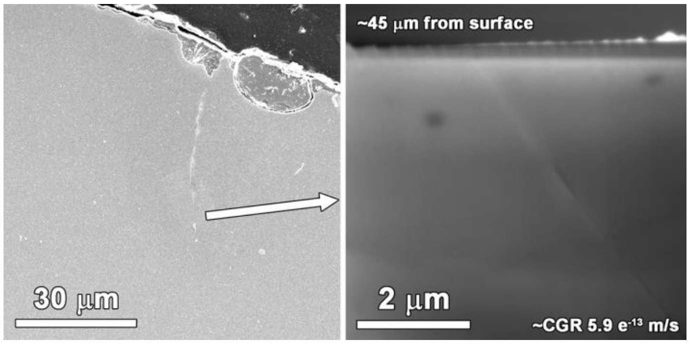

Figure 48: SEM/STEM images of the permanent mold sample illustrating deep SCC cracks and the location of a TEM lift-out ~45 µm from the surface.

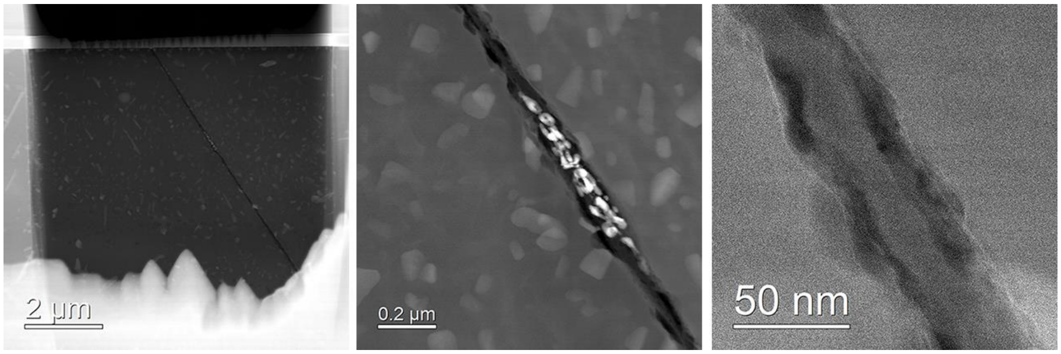

Figure 49: STEM(DF) images at varying magnifications of the cross-section of an SCC crack in the permanent mold sample.

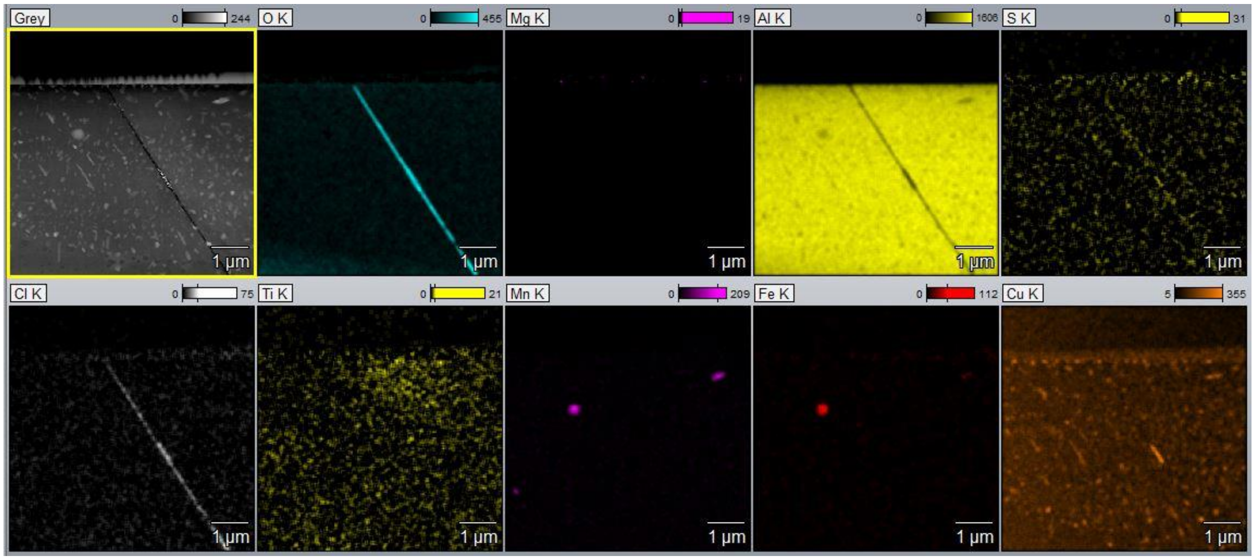

Figure 50: STEM(DF) and EDS elemental maps of the FIB sample prepared from a permanent mold SCC crack.

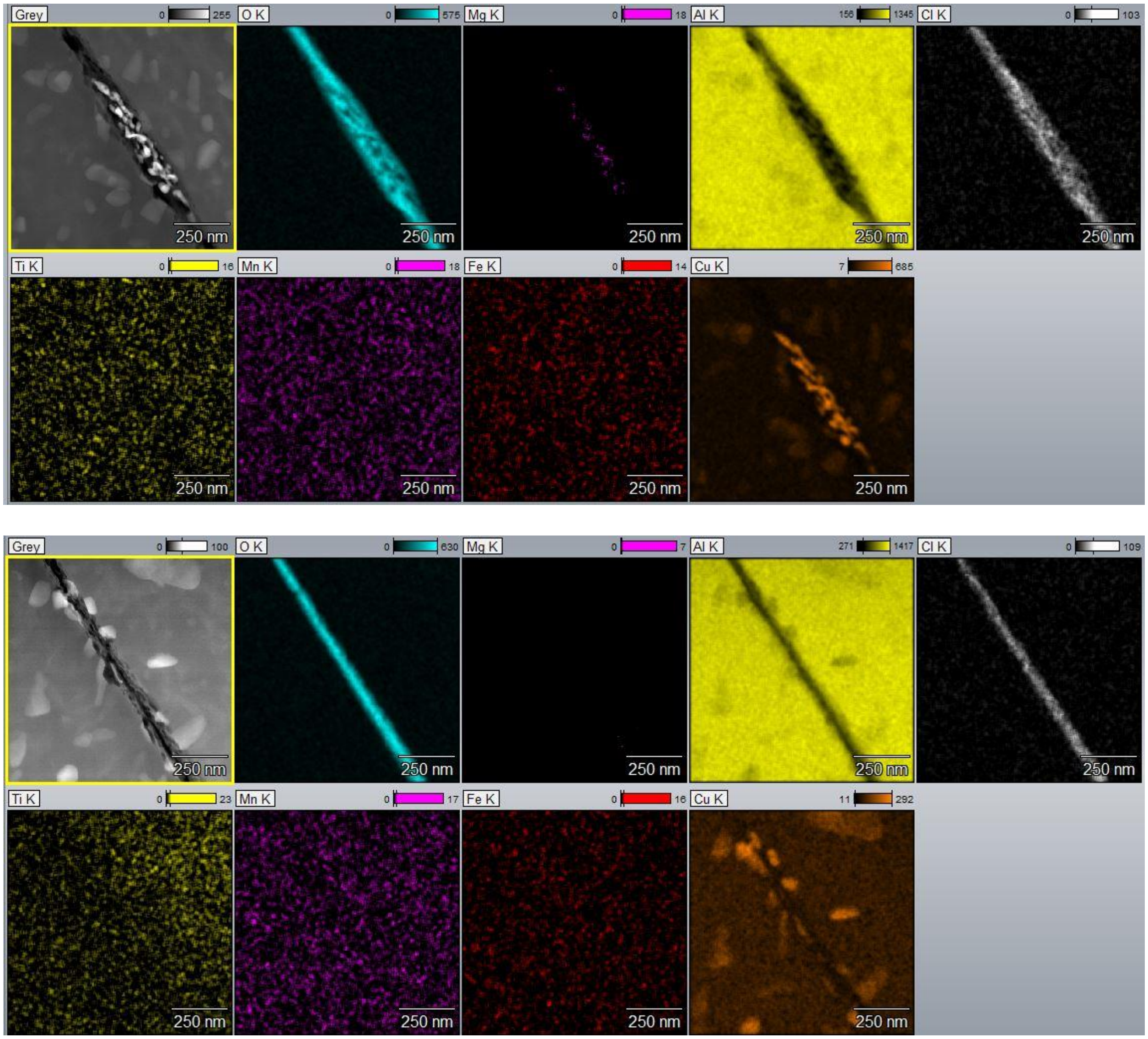

Figure 51: STEM(EDS) elemental maps of the SCC crack in regions with and without intergranular precipiates. A strong Cl signal is oberved colocated with the aluminum oxide signal.

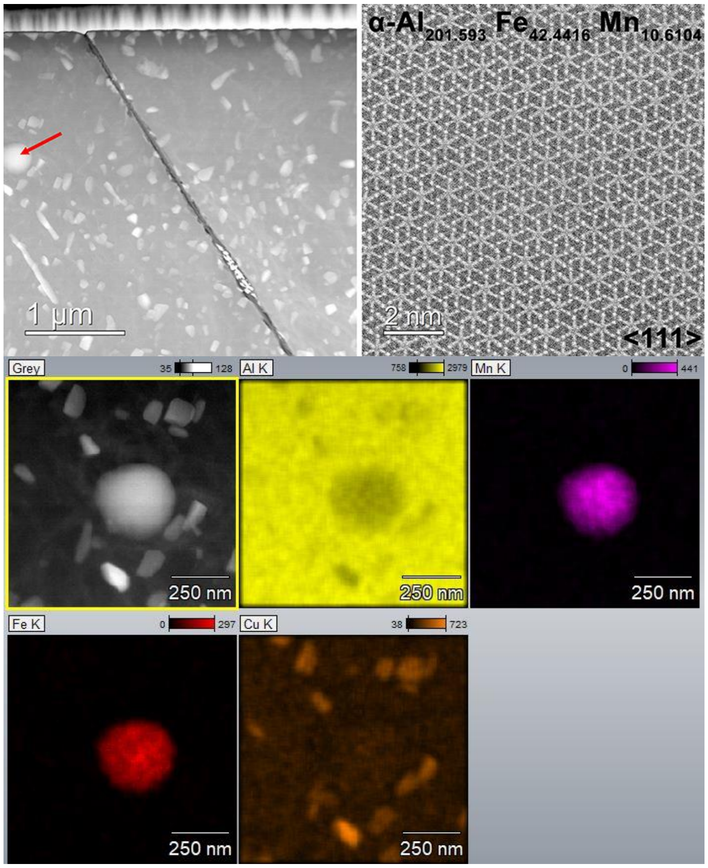

Figure 52: STEM(HAADF) and EDS elemntal maps of single, large precipitates (red arrow) observed in the matrix.

3.4 SECCM Testing

The sand cast with chill sample was selected for SECCM testing. A highly polished surface was first lightly etched to discern the grain microstructure (Figure 6). The Sand Cast with chill sample exhibited an equiaxed grain size ranging approximately 60-70 µm in diameter (Tables 3 and 4), which allowed for proper examinations of inside grains (IG) and grain boundaries (GB). An optical micrograph highlighting the outline of a single grain is shown in Figure 53, where the red lines are used to outline the grain and the green dots are approximate placement of SECCM testing points at IG and GB locations. A series of grains/grain boundaries pairs/triplets were selected for analysis to demonstrate how the SECCM technique could be utilized for comparative studies (e.g. in-grain analysis in Figure 6 and grain boundaries in Figures 54 and 55).

The OCP vs. time and Tafel polarization curves collected on the points shown in Figure 55 are shown in Figures 56 and 57. The comparison of OCP curves between GB and IG points shows (i) OCP values are in the range of -0.6 to -0.8 V vs Ag/AgCl which is within the expected range of OCP for Al alloys (ii) IG points have slightly high OCP compared to GB points. However, these OCP did not attain steady-state values and fluctuations were observed since the data was collected for only 60 seconds. The Tafel plots comparing GB and IG points show the steep anodic current profile and broad cathodic current profile, however, distinct differences between GB and IG were not established and need more points for improved statistics.

In order the improve the statistical significance, the subsequent measurements were performed on 25 GB and 25 IG points, whereas OCP (collected for 300 seconds as opposed to 60 seconds) and Tafel polarization were collected and shown in Figures 57 and 58. The first 60 seconds data were ignored since the solution-metal interface may not have equilibrated, and the last 270 seconds of OCP data were averaged (Figure 59 a), which clearly showed the broader distribution of potential and GB points have lower OCP than the IG points. The lower OCP of GB locations indicates that IG locations are more noble/less corrosive than the GB. This observation is also in-line with the E_{corr} and I_{corr} values determined from Tafel curves (Figure 59 b and c). The E_{corr} values of GB is lower than the IG points. The I_{corr} values are broadly distributed and are higher for GB than the IG, which supports the idea that GB locations will corrode more than the IG locations during Tafel polarization.

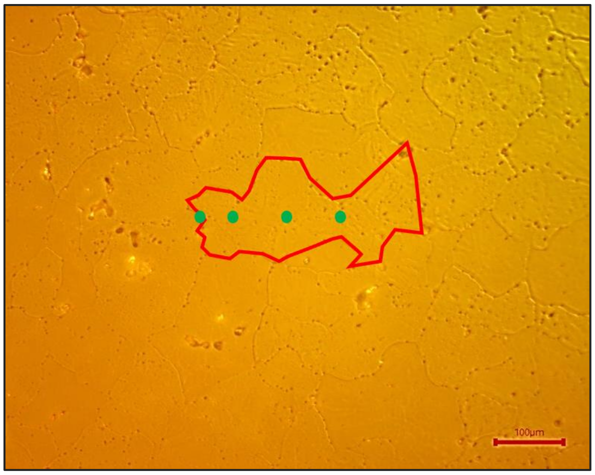

Figure 53: Optical micrograph of the sand cast with chill sample illustrating the testing methodology for understanding grain boundaries and grain interiors. The red line highlights area of interest where grain boundaries and grains can be analyzed at locations indicated by green dots.

Figure 54: Optical micrographs illustrating how the SECCM technique is performed on an alloy with grains on the order of 10s of micrometers. In this example, the probe is utilized to land at a single grain boundary and measure the electrochemical corrosion potential (OCP). The point in the center of the grain (red circled) is the same region collected and illustrated in Figure 6. The black conical shape at the top is the capillary tip and the similar shape at the bottom of the image is the capillary's shadow.

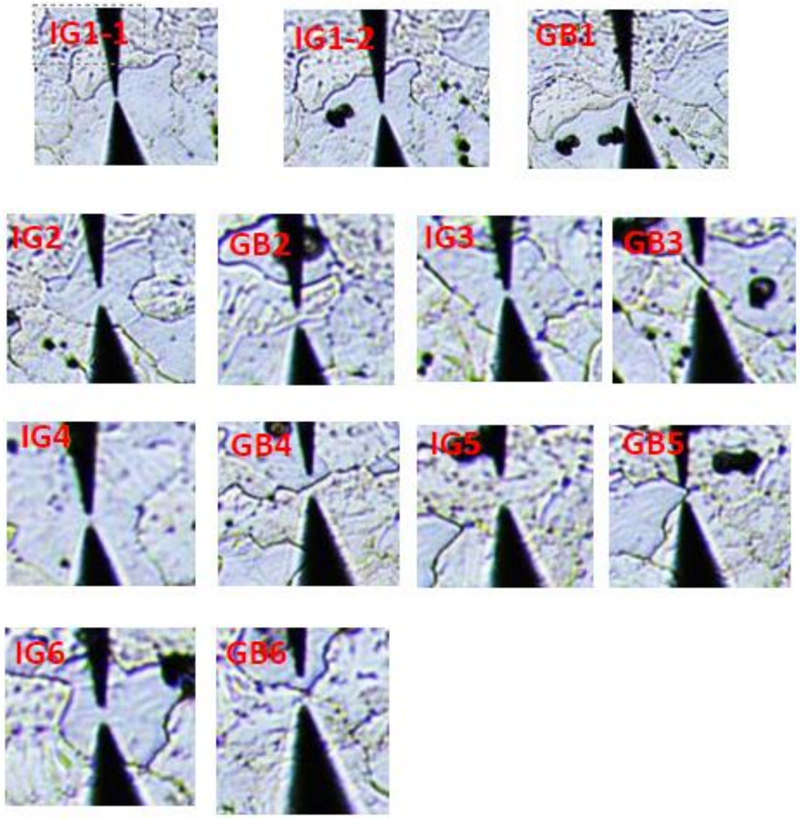

Figure 55: Optical micrographs showing the various testing sites for grain interiors (IG) and grain boundaries (GB) with the number to identify the specific site examined.

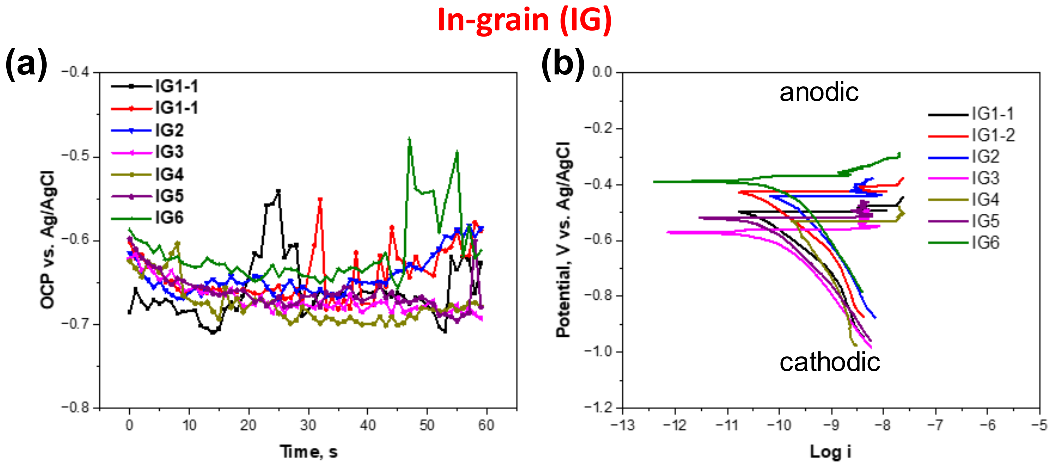

Figure 56: OCP vs Time (a) and Tafel polarization (potential vs log i) (b) for SECCM IG measurements at locations shown in Figure 55.

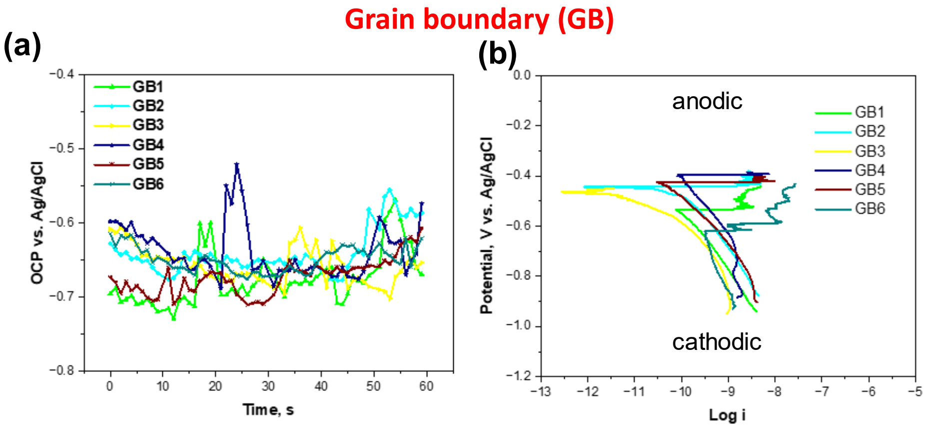

Figure 57: OCP vs Time and Tafel polarization (potential vs log i) for SECCM GB measurements at locations shown in Figure 55.

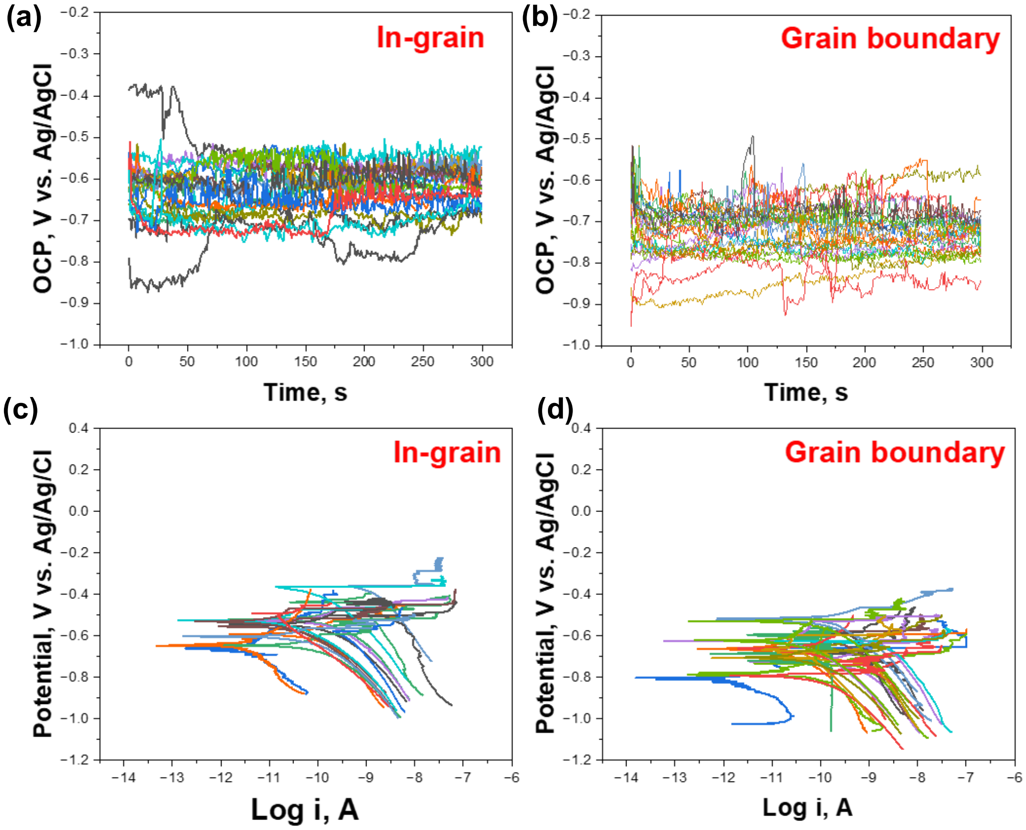

Figure 58: OCP vs Time (a, b) and Tafel polarization (potential vs log i) (c, d) collected using SECCM on 25 IG and 25 GB points to understand statistical variations of OCP, E_{corr} and I_{corr} at IG and GB sites.

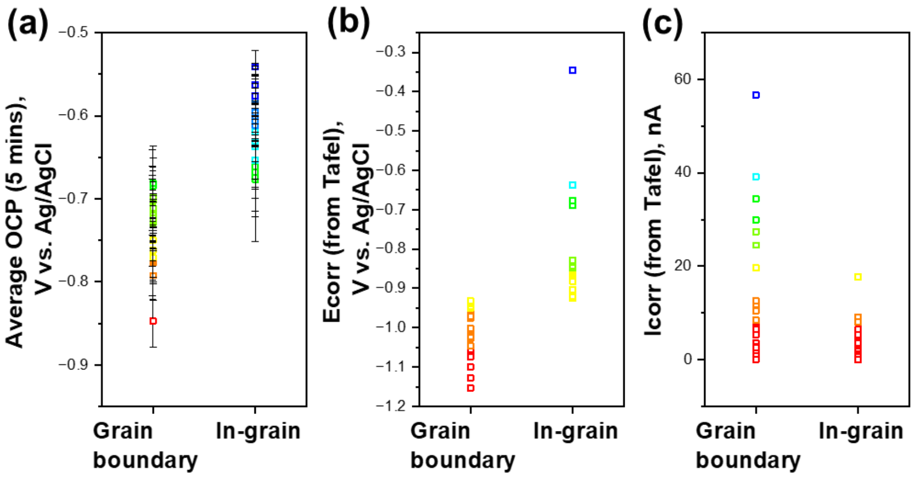

Figure 59: Comparison of averaged OCP and E_{corr} and I_{corr} obtained on 25 IG and 25 GB points, showing the statistical significance.

3.5 Microstructural Analysis of Al-Si-Mg-Fe Alloys

3.5.1 SEM Examination of Al-Si-Mg-Fe

Two bulk samples of Al-Si-Mg-Fe were examined for basic microstructure, compositional and grain distributions. The bulk samples were designated Al D3 (7.43% Si, 0.39% Mg, 0.72% Fe, 0.12% Ti, balance Al) and Al D7 (6.68% Si, 0.34% Mg, 1.69% Fe, 0.11% Ti, balance Al). These chemistries were produced to mimic Al alloys with high recycle content that often results in high Fe%. Due to schedule limitations, only a basic microstructural analysis was performed as described below.

These samples displayed a more dendritic grain structure with acicular iron-containing intermetallic needles ranging from approximately 10 to 200 μm in length. Bright structures in Figure 60 indicate precipitates while variations in the greyscale indicate phase and grain orientation contrast.

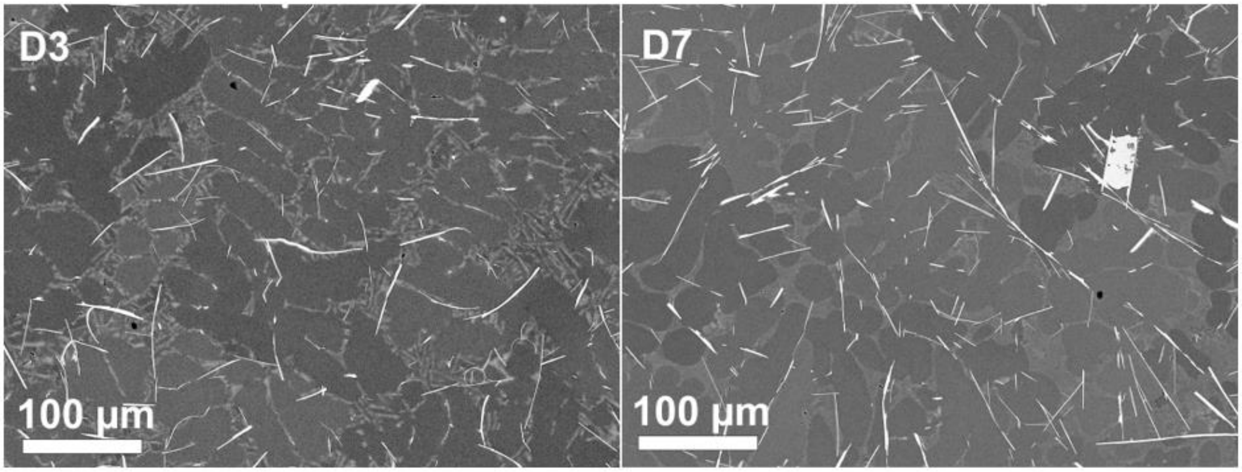

Figure 60: BSE images of Al-Si-Mg-Fe samples D3 and D7.

Silicon precipitates were also apparent and larger in the D3 material at approximately 5 to 10 µm compared to a 1 to 3 µm size in the D7 sample as seen in Figure 61.

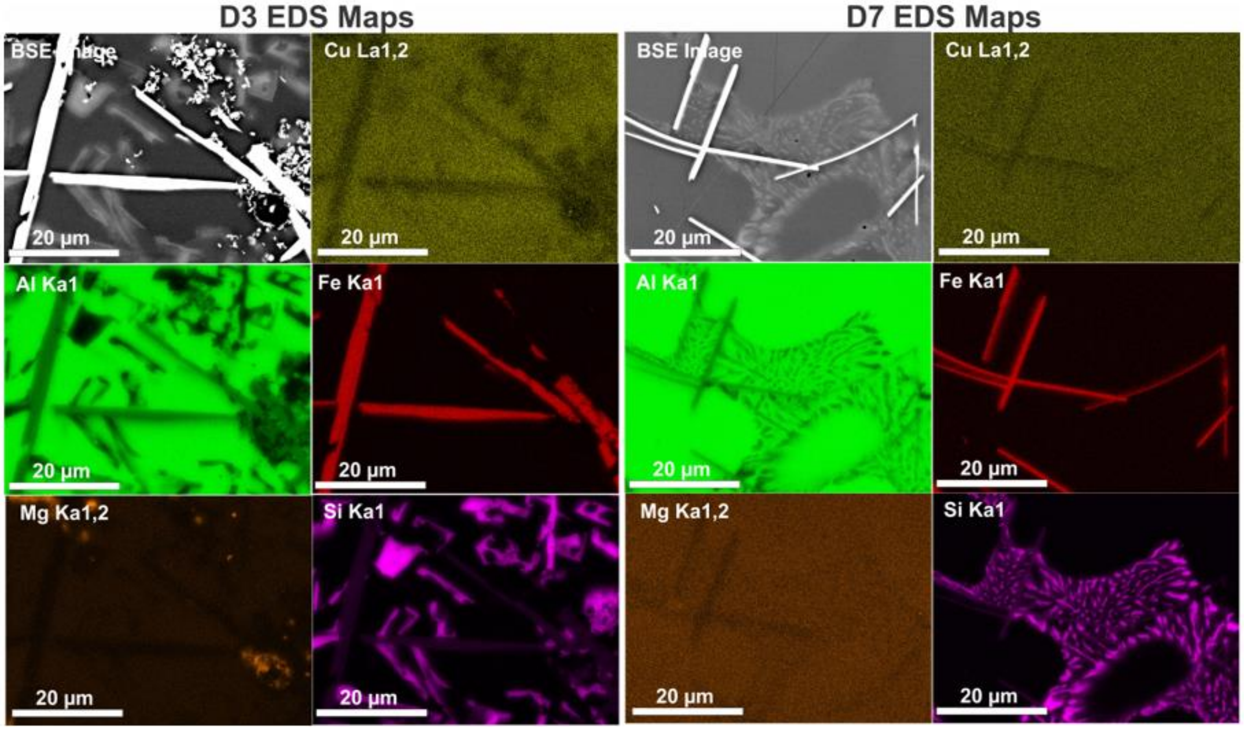

Figure 61: EDS maps of D3 and D7 samples.

EBSD inverse pole figure maps (Figure 62) reveal the dendritic grain structure. Due to the large grain size of the Al-grains, only few of those grains were measured. Black regions correspond to the Fe- and Si-rich regions that could not be indexed with the Al-crystal structure file. The second phase containing the Si-precipitates appears to be dominated by smaller 5-10 µm grains, while the dendrite grains extend over several 100s of µm (the maps in Figure 62 do not show an entire grain in either sample).

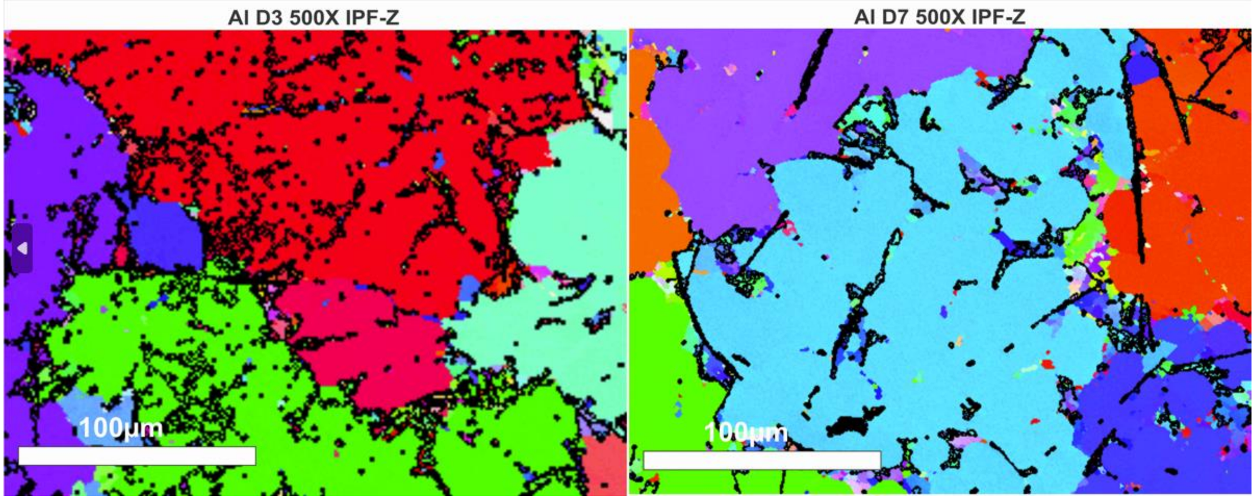

Figure 62: EBSD inverse pole figure map in the z-direction of D3 and D7 samples.

3.6 Analysis of Recycled 6XXX series Al Alloys

Three tubes, consisting of twitch and pre-consumer Al 6061 scrap, were extruded by PNNL's ShAPE process and examined for basic microstructure, compositional and grain distributions. The tubes were labeled as "A" Al 41-1425 (50% twitch + 50% pre-consumer Al 6061 scrap), "B" Al 32-1425 (75% twitch + 25% pre-consumer Al 6061 scrap), and "C" Al 37-1425 (100% twitch).

3.6.1 SEM Examination

All three tube samples displayed a consistent, equiaxed grain structure with a relative reduction in grain size as twitch percentage increased. In Figure 63, precipitates are bright while variations in the grey matrix correspond to orientation contrast.

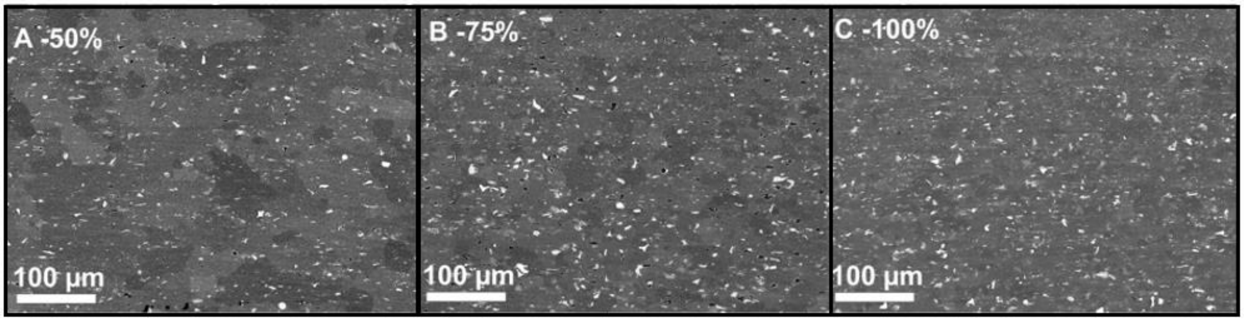

Figure 63: 250X Tube centers BSE images. The "%" refers to twitch content in the tube raw material.

They also showed similar distributions of precipitates within the aluminum matrix as shown in Figure 64. Precipitates were primarily silicon and magnesium with some iron and copper as well. Precipitate sizes range from approximately 1 to 10 µm.

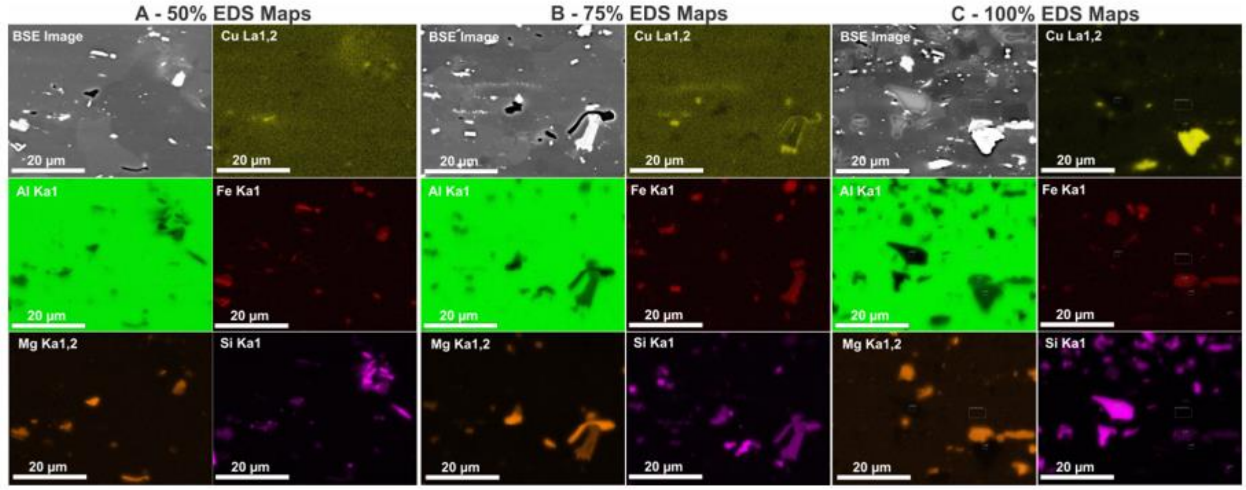

Figure 64: Tube center EDS Maps. The “%” refers to twitch content in the tube raw material.

EBSD analysis in Figure 65 and Figure 66 depicts the grain size distributions in the three specimens. The grain size decreases from sample A > B > C. Histograms showing the grain size distributions in the three samples are shown in Figures 67-69 for samples A-C, respectively. As the grains have irregular shapes and the EBSD analysis measures grain area, the “grain size” reported represents the circle equivalent diameter for each grain. As the smallest grains (<10 μm) in each histogram are an artifact of the limited imaging resolution, they were omitted from statistical analysis. The mean grain size for sample A was calculated from 243 grains to be 26.6±18.1μm. In sample B the mean grain size (526 grains) was 18.4±8.2 μm and in sample C the mean grain size (625 grains) was 16.1±6.3 μm.

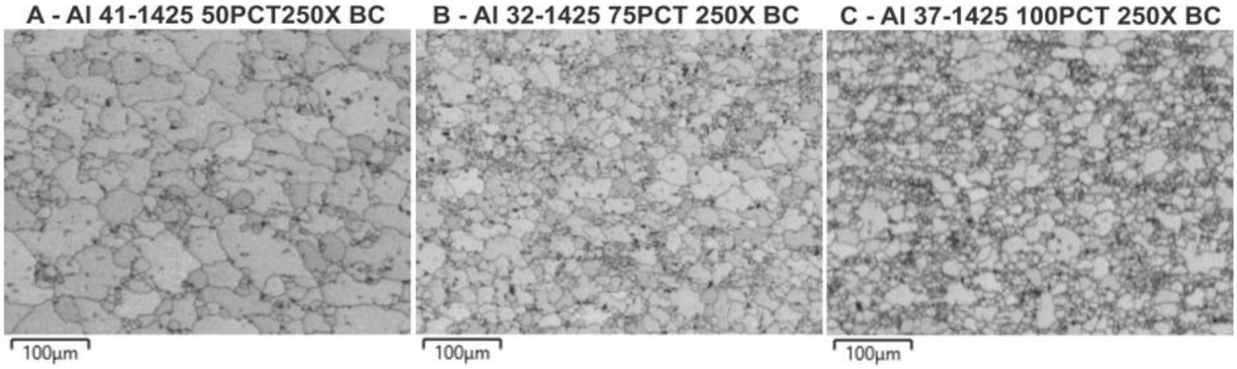

Figure 65: EBSD Band Contrast images showing relative grain size. The “PCT” refers to % twitch content in the tube raw material.

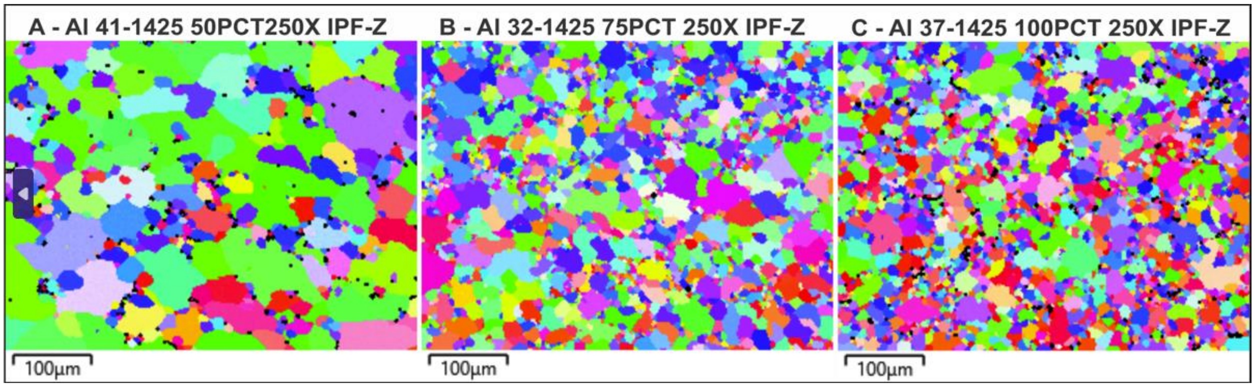

Figure 66 EBSD inverse pole figure (IPF) maps in the z-direction of the three recycled specimens. The "PCT" refers to % twitch content in the tube raw material.

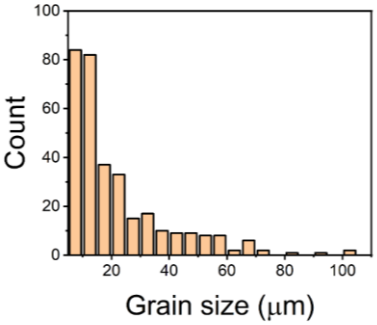

Figure 67 Histogram showing the grain size distribution in sample A (50 % twitch loading).

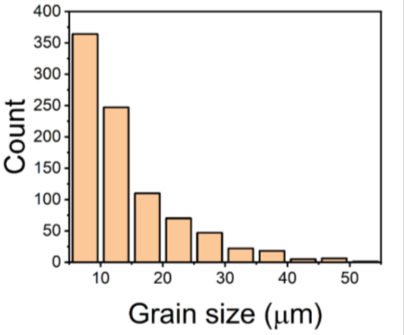

Figure 68 Histogram showing the grain size distribution in sample B (75 % twitch loading).

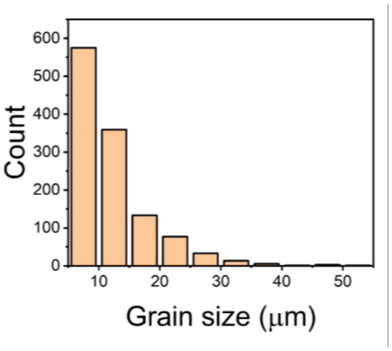

Figure 69 Histogram showing the grain size distribution in sample C (100% twitch loading).

3.6.2 SECCM Analysis

The SECCM measurements were performed as a line scan from the outer diameter (O.D.) to the inner diameter (I.D.) for all three tube samples, comprising 100%, 75% or 50% twitch with the balance made of pre-consumer Al 6061 scrap. The length of the line scan was 800 µm with a 100 µm step size, so the SECCM measurements were performed at a total of 9 points across the line (Figure 70). At each point, the OCP was collected for 3 minutes, followed by the Tafel polarization. Figure 71 shows the full OCP and Tafel polarization curves performed on each point. Figure 72a shows the averaged OCP determined from the OCP (3 mins.) measurement. The corrosion potential (E_{corr}), and corrosion current (I_{corr}) were determined from Tafel polarization curves and shown in Figures 72b and c, respectively.

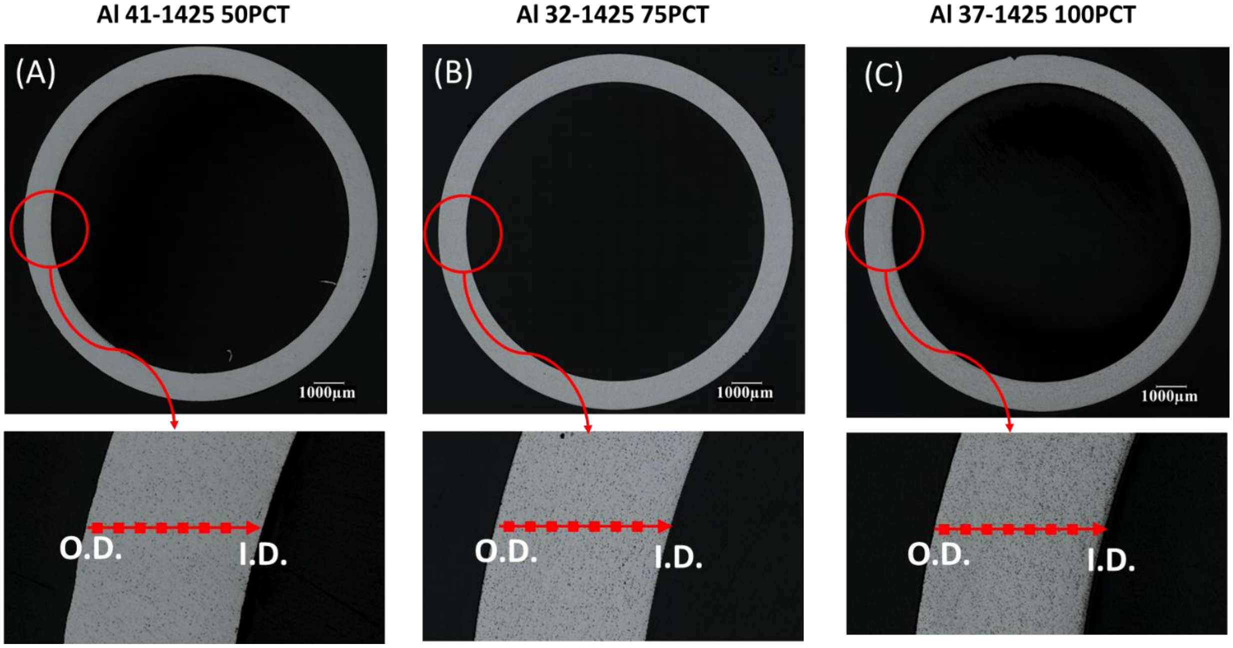

Figure 70: Micrographs of the three tube samples showing the location of the SECCM line scan performed between the outer and inner diameter of the tube. The approximate length of the line scan is 800 µm with 100 µm step (a total of 9 points). “PCT” refers to % twitch content in the tube raw material.

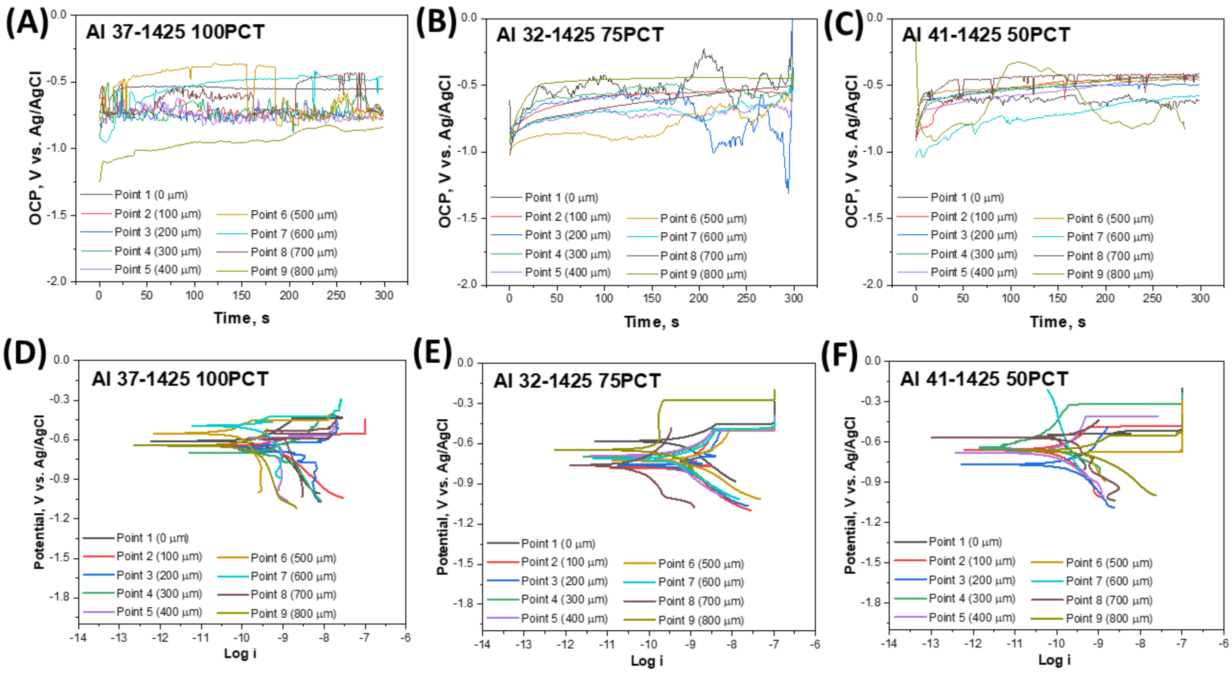

Figure 71: (A-C) The full OCP curves were collected for 3 minutes, and (D-E) the corresponding Tafel polarization curves measured at each point along the line for the samples. The “PCT” refers to % twitch content in the tube raw material.

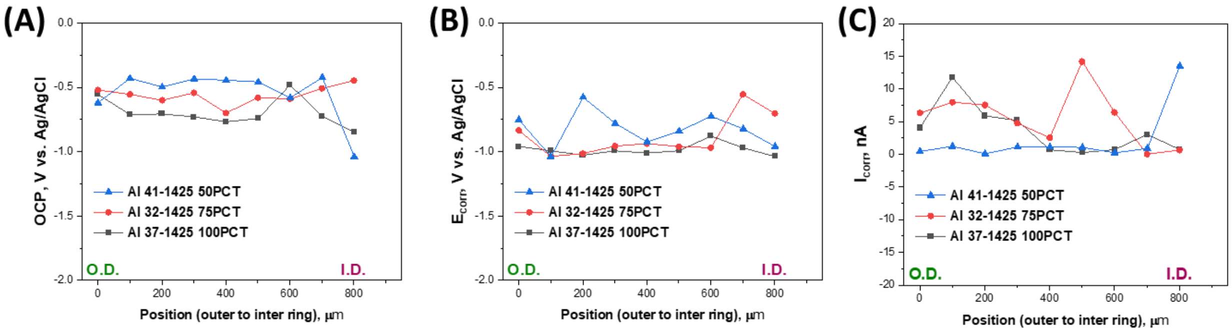

Figure 72: The SECCM line scan performed on tube samples showing the (A) averaged OCP determined after performing 5 mins. (B) Corrosion potential (E_{corr}), and (C) corrosion current (I_{corr}) determined from the Tafel polarization curves performed at each point along the line. “PCT” refers to % twitch content in the tube raw material.

The OCP and E_{corr} values of all three samples lie between -0.4 V and -1V, which aligns with the typical potential range for Al alloys. Furthermore, the OCP and E_{corr} values indicate that the tube with equal proportion of twitch and 6061 scrap is more cathodic (more noble) by 120 mV and 310 mV compared to the tube made from 75% and 100% twitch, respectively. This trend indicates that the tube made from 100% twitch will likely corrode more than the other two. This observation is supported by the presence of higher I_{corr} current measured at several points along the line scan of the 100% twitch tube. Furthermore, the outer ring exhibits relatively more cathodic behavior than the inner ring; however, most of the points between them show relatively similar OCP in each sample.

In summary, the SECCM measurement determined the order of tendency to corrode as follows: 100% twitch > 75% twitch > 50% twitch. It is presumed that the presence of smaller grains, as observed in EBSD analysis (section 3.6.1) may have contributed to greater anodic behavior in the tube made from 100% twitch. However, the effect of overall chemistry, presence of intermetallics phases, and alloying elements in solution, in controlling the electrochemical response is also likely to play a role and needs further detailed analysis.

4.0 Discussion

The development of this CRADA research program was geared toward meeting five Milestones:

- *Milestone 1:* Complete SCC test on A206 Al with two different grain sizes
- *Milestone 2:* Demonstrate TEM images of SCC tested A206 Al and characterize Cu distribution in the grain interior and grain boundaries
- *Milestone 3:* Demonstrate difference in the electrochemical behavior of A206 Al in as-cast and a heat-treated temper using scanning electrochemical cell microscopy (SECCM) method
- *Milestone 4:* Microstructural examination of specifically tailored Al-Si-Mg-Fe alloys with varied chemistries
- *Milestone 5:* Microstructural/microchemical analysis and SECCM testing on recycled Al6XXX series alloys.

The discussion section will center on addressing each of these three milestones with respect to the data provided in the Results section.

4.1 Milestone 1

SCC tests and tensile tests were performed on A206 alloy samples produced using three different casting methods, in the T6 condition, each with and without the addition of nano forming additives. The nano forming additives were intended to control the grain size during each of the casting methods.

Microstructural analysis, performed using both optical and SEM, indicated that for the Sand Cast and Sand Cast with chill, the addition of nano additives did decrease the grain size, whereas in the Permanent Mold casting the grain size slightly increased with the addition of nano additives. The ability to control grain size is important for the performance of these materials, and in some cases the addition of the nano additives achieved the goal of providing different grain sizes for the SCC tests. It is unclear as to why the grain size in the Permanent Mold sample increased, but it still provided two grain sizes for testing. As previously mentioned, one possible source of error for this measurement could be due to mislabeling either during delivery or receipt of the samples. However, the SEM-EDS chemical mapping of these alloys suggests that the measurements are not in error, with all nano additive samples exhibiting strong Zn signals in both the un-tested alloys and more importantly, in the oxides of the corroded samples.

For the casting conditions utilized in this work and the resulting grain size dependence on the cooling rates, the Permanent Mold samples exhibited the smallest grains followed by the Sand Cast with chill. Given that the Sand Cast with chill sample did show smaller grains, and the grain size reduced further when nano additives were added as compared to the Sand Cast without chill, it is possible that the cooling rate of the Permanent Mold was so rapid that it outweighed the effects of the nano additives. Further research should be geared towards understanding how the addition of nano forming additives affects grain size.

The SCC testing is meant to assess the effect of the various casting conditions through tensile testing response. In the case of the three casting conditions, with or without nano additive, there did not appear to be trends that would clearly indicate an improvement in mechanical performance with change in grain size. In some cases (e.g., Sand Cast with chill nano), the yield stress was higher after corrosion. Although, in all cases the ultimate tensile strength was lower after the samples had been exposed to the salt solution. The large standard deviation was likely a result of too few samples being tested per experiment. With only 5 samples being run per condition, even small errors in the testing or variability in initial samples would play a large role in the standard deviation. Interestingly, several of the samples failed either at the extensometer or outside of the gauge, suggesting that it may be necessary to reconsider the dog bone design or increase the total number of samples tested per condition, to elucidate the SCC response of these materials. Combined with the pore characteristics of these castings, small imperfections in the dog bone samples, especially in the corroded state, could play a large role in the failure location.

To further assess the casting conditions and nano additives, a Quality Index (QI) parameter was calculated (Figure 73). We define poor SCC response to indicate a “large” reduction in the QI while good SCC response indicates low reduction in QI after SCC testing. Figure 69 shows that for all samples, except for the Sand Cast with chill (#2), the QI decreased after corrosion testing. The Permanent Mold samples (as-received and with nano additives) exhibited the largest percent decrease in the QI after corrosion.

Post SCC test microstructural examination provided insight as to why the samples failed after corrosion. As expected, the exposure to a 3.5% salt solution after 30 days of cyclic dipping and drying caused localized attack along the grain boundaries to depths of 100’s of micrometers in some instances. In addition, the pores intersecting the surface can play a role by allowing water to be trapped while the rest of the surface is dried. Examination of the cross-section surfaces for perceived amount of SCC cracks and crack depths (Figures 40-46, and Appendix Figures 124-139) were translated into relative scores for SCC response (Figure 73). These data corroborate the QI scores viz., Permanent Mold samples showed the highest degradation after SCC testing and the minimum degradation was shown by the Sand Casting with Chill samples. The Sand Cast without chill (#1) also exhibited a medium range SCC response that correlated to a smaller decrease in QI post-SCC testing. The addition of nano additives, which in both Sand Cast cases showed a decrease in grain size, appears to correlate with a poorer QI index and a poorer SCC response. Since the Permanent Mold sample without additives exhibited a smaller grain size, the lowest QI, and poor SCC response, it suggests that grain size plays an important role in the SCC response of these materials.

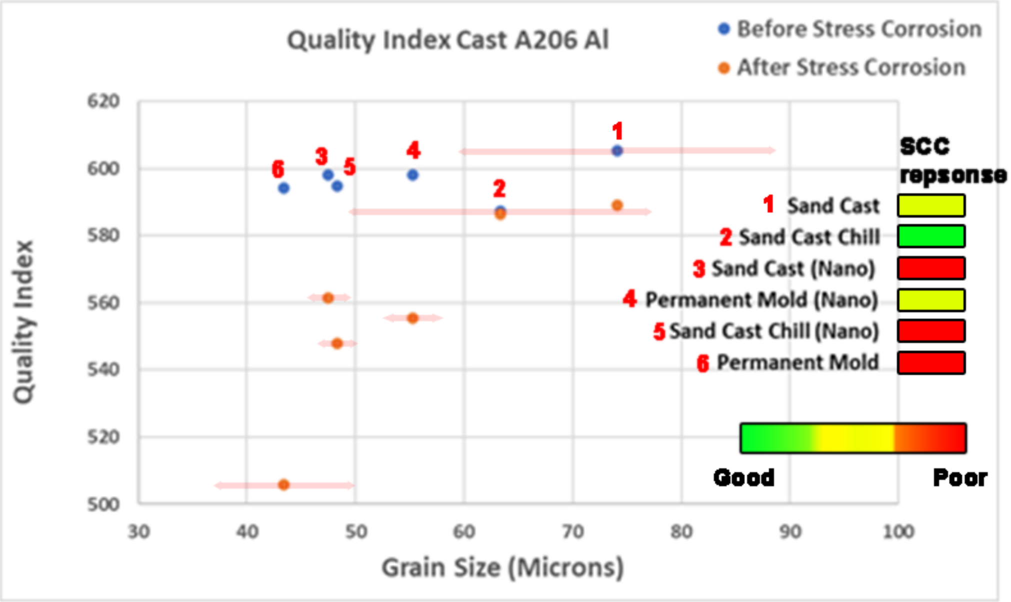

Figure 73: Quality index (QI) versus grain size and SCC corrosion response. Poor SCC response implies greater degradation in QI in post-SCC tensile testing while good SCC response implies minimal reduction in QI after SCC testing.

4.2 Milestone 2

Grain boundaries are an important factor when considering the performance of a material, although often modification of their properties can have conflicting responses depending on the requirements. Grain refining additives, such as the nano additives examined in this study, can reduce the grain size during casting. This reduction in grain size can improve the strength of the alloy but depending on how the grain boundaries are affected by nano additives, it may affect other properties too such as corrosion response. Milestone 2 was aimed at examination of the grain boundaries from a sample post SCC testing to understand corrosion response at very small length scales. The as-received Permanent Mold sample, that exhibited the smallest grain sizes (i.e., most rapid cooling rate) and the worst SCC response (Figure 73) was chosen for examination. A site-specific FIB lift-out was prepared from a leading crack tip (Figure 48) for examination. This type of analysis allows detailed analysis of the crack on the order of nanometers, at distances of tens of micrometers from the exposed dog bone surface.

The data highlighted in Figures 49-52 indicates that the surrounding matrix microstructure appears like the un-tested sample observed in Figure 39. The matrix has a high density of ordered, Al_2Cu that appears to form almost immediately adjacent to the boundary, and in some cases on the boundary. There appear to be no chemical gradients (e.g., Cu, Al, or Ti) associated with the grain boundary. The SCC crack was filled with alumina that exhibited both S and strong Cl signals, suggesting that the saltwater solution was able to penetrate along the tight (~50 nm wide) crack. Given that the only stress applied to these alloys was through the room temperature drying of the salt solution, it suggests that even at these chloride concentrations, the grain boundaries are highly active. Future work could include the utilization of highly polished coupons of identical alloys in each casting condition in the dip testing process. Microstructural analysis of the coupons as compared to the dog bones could provide a baseline for the material response of the A206-T6 alloys.

4.3 Milestone 3

Electrochemical corrosion testing methods provide direct quantification and comparison of material chemical stability and origin of instabilities. The chemical composition of interior grain (IG) and grain boundaries (GB) influence the bulk corrosion properties; therefore, it is imperative to distinguish the corrosion behavior between IG and GB using localized probing methods such as SECCM. SECCM was performed on targeted IG and GB of the Sand Cast with chill sample and the corrosion properties (defined by open circuit potential (OCP), corrosion potential (E_{corr}) and corrosion current (I_{corr})) were determined by performing OCP vs. time and Tafel polarization curves.

This sample has a grain size of 60-70 µm in diameter (Tables 3 and 4). The diameter of the tip used in SECCM defines the spatial resolution or probing area. The tip diameter of 10 µm and 3 µm were initially employed with 0.01 M NaCl as electrolyte, and the 3 µm diameter tip (Figure 5) was selected as it showed higher stability with no issues of electrolyte leaking as shown in Figure 6. Figure 7 shows the typical OCP vs. time and Tafel (potential vs. curves) polarization curves collected on IG and GB points.

Following the initial success in performing localized corrosion testing using 3 µm tip, the SECCM was performed on the series of subsequent IG and GB (6 pair points) to establish the feasibility to compare the corrosion properties. The OCP curves showed the OCP values ranges between -0.6 to -0.8 V vs. Ag/AgCl, which is in-line with the expected range of OCP values for Al alloys (Figures 56 and 57). The associated Tafel curves shows steep anodic current profile and broad cathodic profile, which indicates high rate of metal dissolution. However, a clear distinction in differences in corrosion properties were not established during this initial set of measurements and needed more points for improved statistics. Therefore, the subsequent SECCM measurements were performed for 25 IG and GB pair points with OCP collected for long duration (300 seconds).

The plot of averaged OCP comparing IG and GB shows that the OCP of GB is generally lower than the IG, indicating that GB is less noble/more corrosive compared to IG (Figure 59 a). The E_{corr} and I_{corr} determined from Tafel plot (Figure 59 b and c) also support this observation as it shows the E_{corr} values of GB are lower than the IG and the I_{corr} values of GB are broader and higher indicating more propensity for corrosion than then IG.

Overall, SECCM method is successfully adapted to testing the electrochemical corrosion behavior in cast Al alloys and may be expanded to other type of alloys for comparison.

4.4 Milestone 4

In addition to A206 alloy castings, two Al-Si-Mg-Fe samples (labeled D3 and D7) with controlled Si and Fe chemistries were also provided that mimic Al alloys with high recycle content that often results in high Fe%. Due to schedule limitations, only a basic microstructural analysis was performed. Electron backscatter imaging, EDS elemental analysis, and EBSD grain size measurements were collected for both samples and compared. The Si and Fe content used in these samples produced a large volume fraction of intermetallic phases that were Fe and Si rich (Figure 61). No immediate local differences in chemistry or secondary phases could be ascertained between the D3 and D7 samples. In terms of grain size, the D3 sample appeared to have larger grains as compared to the D7 sample. Additional work needs to be performed to determine how their relative chemistries affect grain size, SCC, and the local electrochemical response.

4.5 Milestone 5

Al recycling is an important process to reclaim scrap materials and lower the materials cost and embedded energy. PNNL developed the ShAPE process that can efficiently recycle scrap into extrusion forms such as tubes tested in this work. Milestone 5 was intended to understand how the processing feed stock, comprising different amounts of scrap, could affect the microchemistry and corrosion response of 6xxx Al alloys. Three different feedstocks with varying percentages of twitch (100%, 75%, and 50%) mixed with pre-consumer 6061 Al scrap were examined. The SECCM line scan measurements performed on the ShAPE extruded tubes made from these recycled materials show that tube made from 100% twitch feedstock is the least cathodic (i.e., most corrosion prone compared to the other two feedstocks). Further, the 100% twitch feedstock also produced a microstructure with the smallest grain size while the 50% feedstock produced the largest grain size. Chemically, there were minimal changes in inclusion chemistry, with Cu, Fe, Si, and Mg-rich phases observed in all feedstocks with no significant differences in their dimension and morphology. Higher resolution analysis, such as TEM to further assess finer details (e.g., grain boundary chemistry and defect densities), in combination with SCC and mechanical testing, is recommended for future work to make direct correlations of the corrosion response, microstructure, and mechanical properties of ShAPE produced extrusions.

5.0 Conclusions

The research conducted at PNNL was designed to understand the SCC, corrosion response and microstructure of several Al alloys viz. A206 Al alloy in the T6 temper, as-cast Al-Si-Mg-Fe alloys and recycled 6xxx extruded by the ShAPE process. A206 was produced by three different casting methods, namely sand casting with and without chill and permanent mold casting. For each of the casting techniques, A206 was cast in two variants, with and without nano forming additives. Corrosion and microstructures in recycled Al alloys were also explored in Al-Si-Mg-Fe alloys (two as-cast chemistries with differing Fe and Si contents) and in 6xxx Al extruded tubes (three types of recycled feedstock comprising twitch and pre-consumer 6061 scrap). The work was designed to achieve the following milestones:

- Milestone 1: Complete SCC test on A206 Al with two different grain sizes.
- Milestone 2: Demonstrate TEM images of SCC tested A206 Al and characterize Cu distribution in the grain interior and grain boundaries.
- Milestone 3: Demonstrate difference in the electrochemical behavior of A206 Al in as-cast and a heat-treated temper using scanning electrochemical cell microscopy (SECCM) method.
- Milestone 4: Microstructural examination of specifically tailored Al-Si-Mg-Fe alloys with varied chemistries.
- Milestone 5: Microstructural/microchemical analysis and SECCM testing on recycled Al 6XXX series alloys.

The goal of each of the milestones was to elucidate a different facet of the aluminum alloys tested, ranging from the mechanical response to SCC testing to understanding the microstructure and local microchemical response. The following conclusions can be reached:

- SCC testing following ASTM standards G44-99 and G139-05 were performed on A206 Al samples produced by three different casting conditions, with and without nano additives for each of the casting conditions. Post-SCC tensile testing suggests that Sand Casting, whether with or without chill, performed better than the Permanent Mold samples. The addition of nano additives appeared to lower the quality index of the samples. SCC response corroborated the QI results in that the samples with smaller grains exhibited poorer corrosion response (e.g., larger/higher density of SCC-induced cracks).

- Contrary to expectation, presence of nano additives did not necessarily result in grain size refinement in the castings (relative to their respective non-nano additive counterpart). Microstructural analysis using TEM/EBSD mapping showed that only the Sand Casting samples showed a lower average grain size with the addition of nano additives, whereas the Permanent Mold sample with nano additives exhibits slightly larger grains. While not explicitly called out, the chemistry of all the samples with nano additives appeared to have Zn, although no single microstructural feature could be pinpointed that would describe the resultant grain change. Finally, the addition of nano additives plays a role in both the formation of pores within these materials, as well as the formation and growth of precipitates. Future work/milestones should focus on the mechanisms of how nano additives affect the microstructure as a function of casting type.

- It was not feasible to perform crack tip analysis on all the SCC tested samples. Nevertheless, the tight leading crack tips observed in a Permanent Mold sample showed the ~50 nm cracks were filled with aluminum oxide with strong S and Cl signals suggesting that even under small stresses, chloride ions can exacerbate cracking.

- The SECCM measurement performed on grain boundary (GB) and in-grain (IG) locations of the A206 alloy sand cast with chill showed the OCP range of -0.6 to -0.8 V vs Ag/AgCl which is within the range for Al alloys. The statistics of SECCM measurement were improved by performing open circuit potential (OCP) and Tafel scans on at least 25 GB and 25 IG points. Collectively, it was determined that GB points have higher OCP and corrosion potential/current than the IG points, which indicates IG are more noble and less corrosive than the GB points.

- SECCM measurements were performed as a line scan from the outer diameter to the inner diameter on three recycled Al6XXX series alloy tube samples, comprising 100%, 75% or 50% twitch with the balance made of pre-consumer Al 6061 scrap. Among these ShAPE extruded tubes, the SECCM data suggests the decreasing order of tendency to corrode as follows: 100% twitch > 75% twitch > 50% twitch. The presence of smaller grains in the tube made from 100% twitch may have contributed to its greater corrosion relative to the other tubes that had a larger grain size. Additional microstructural analysis and testing is necessary to confirm this relationship and investigate potential effects of any other microstructural features associated with different twitch content.

6.0 Publications

- Effect of Grain-boundary dependent corrosion behavior in A206 aluminum alloys. By Venkateshkumar Prabhakaran, Matthew Olszta¸ Timothy J Roosendaal, Karen Kruska, David Weiss and Aashish Rohatgi (Manuscript under preparation – Expected to be submitted to Corrosion Science).

7.0 Appendix

7.1 Sample Receiving

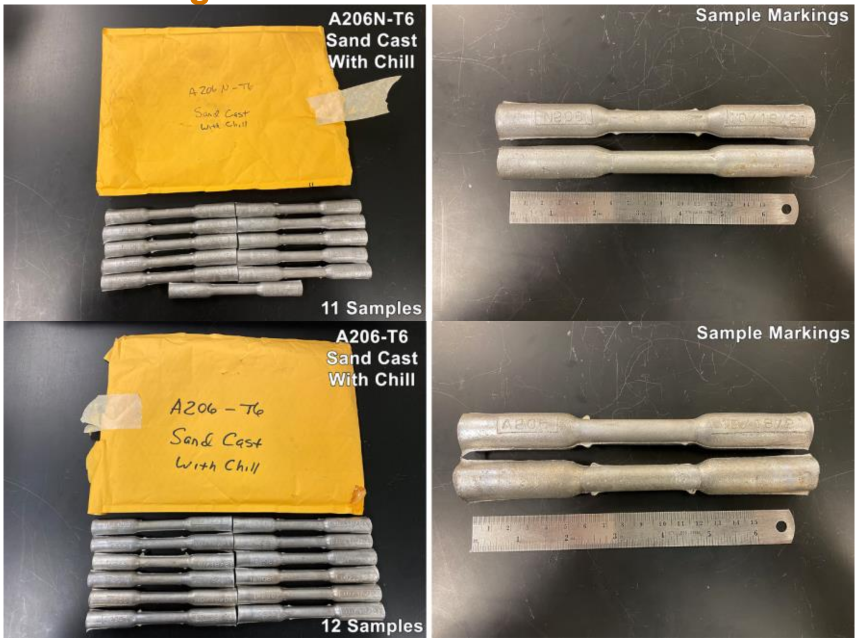

Figure 74: A206-T6 samples cast in a sand cast mold (with chill), with A206N containing nanoparticles. The A206N-T6 sample contained only 11 samples.

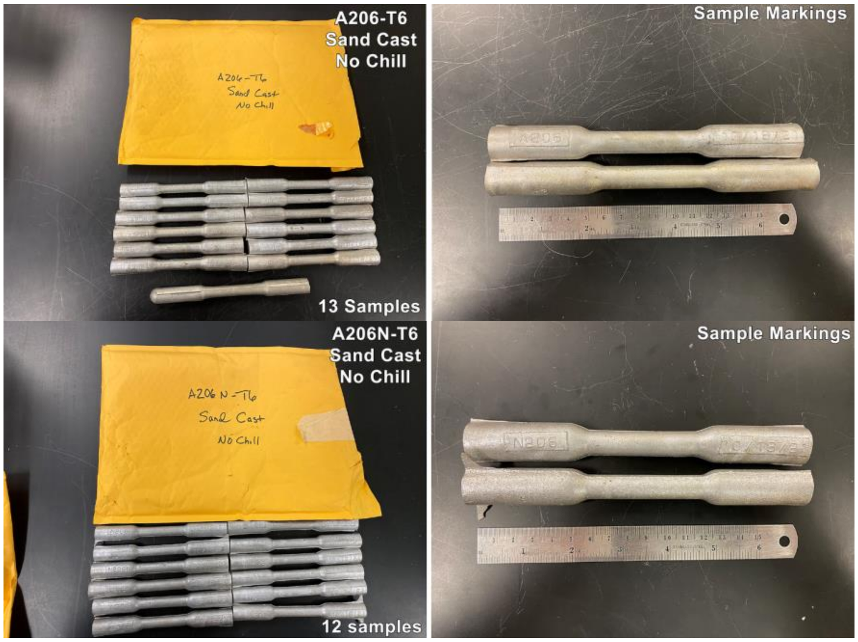

Figure 75: A206-T6 samples cast in a sand cast mold (without chill) with A206N containing nanoparticles. The A206-T6 sample contained 13 samples, one of which appeared to be a permanent mold sample.

7.2 Tensile Testing

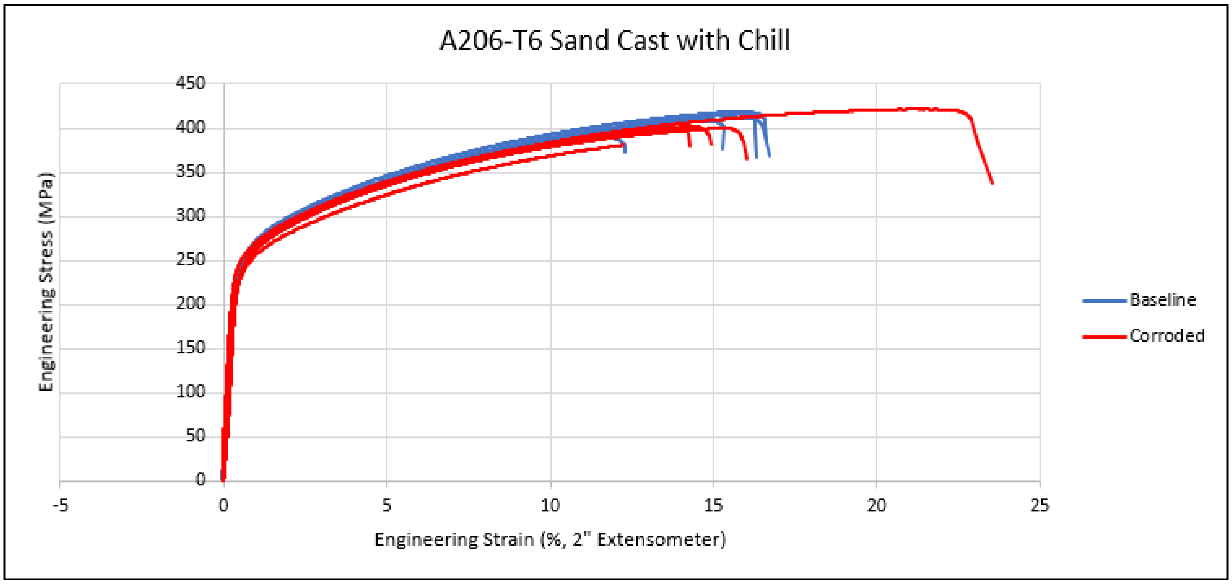

Figure 76: Plot of engineering stress (MPa) versus engineering strain (%) using a 2” extensometer for the A206-T6 sand cast with chill (A) samples.

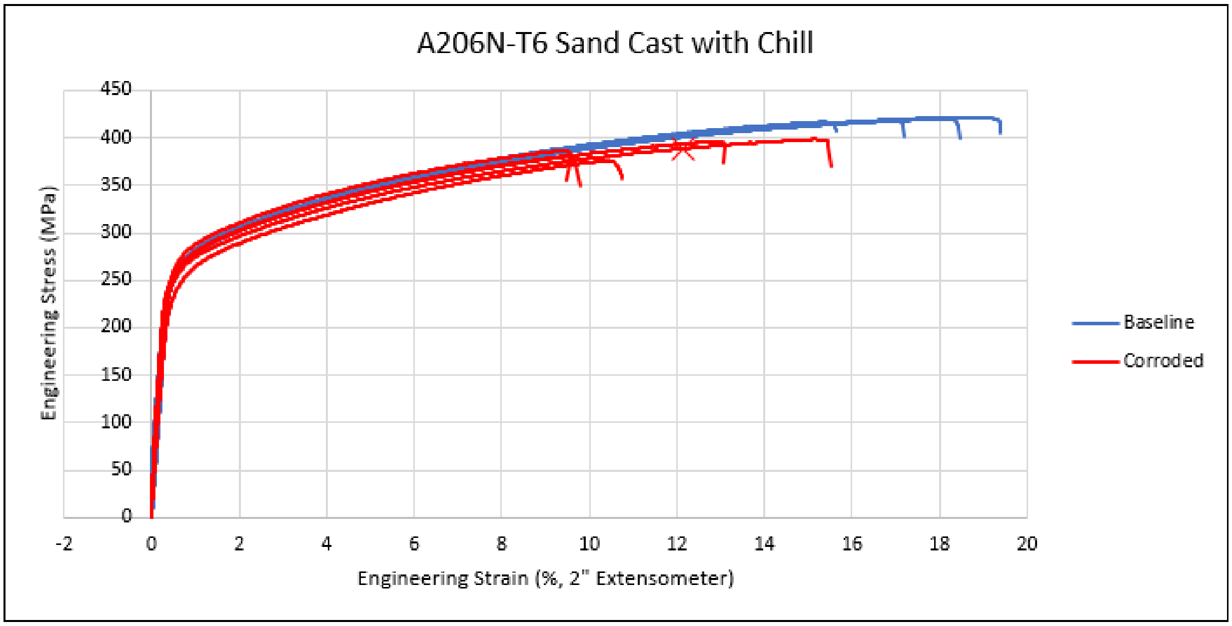

Figure 77: Plot of engineering stress (MPa) versus engineering strain (%) using a 2” extensometer for the A206-T6 sand cast with chill/nano (D) samples.

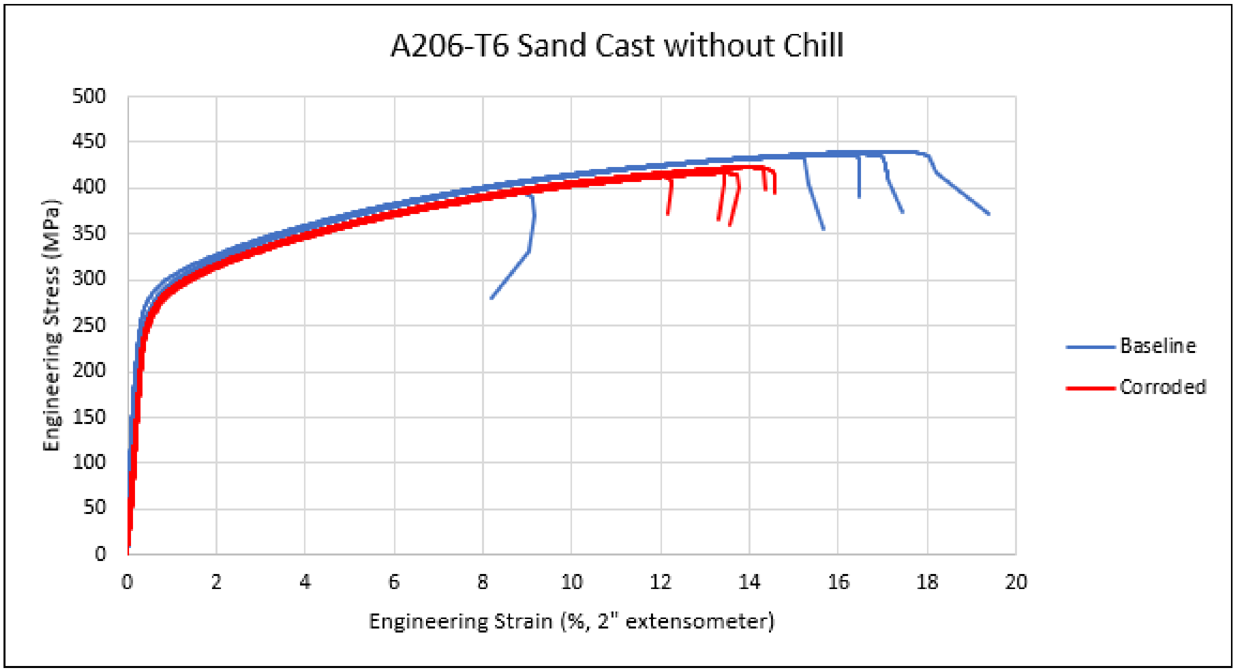

Figure 78: Plot of engineering stress (MPa) versus engineering strain (%) using a 2” extensometer for the A206-T6 sand cast without chill (no chill) (B) samples.

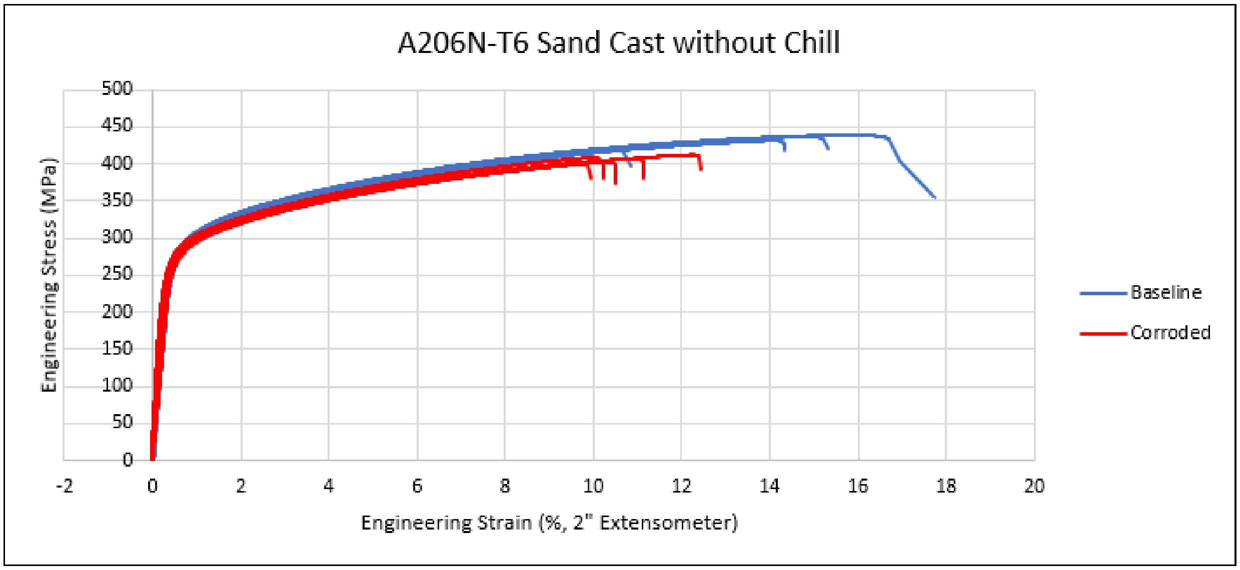

Figure 79: Plot of engineering stress (MPa) versus engineering strain (%) using a 2” extensometer for the A206-T6 sand cast without chill (no chill)/nano (E) samples.

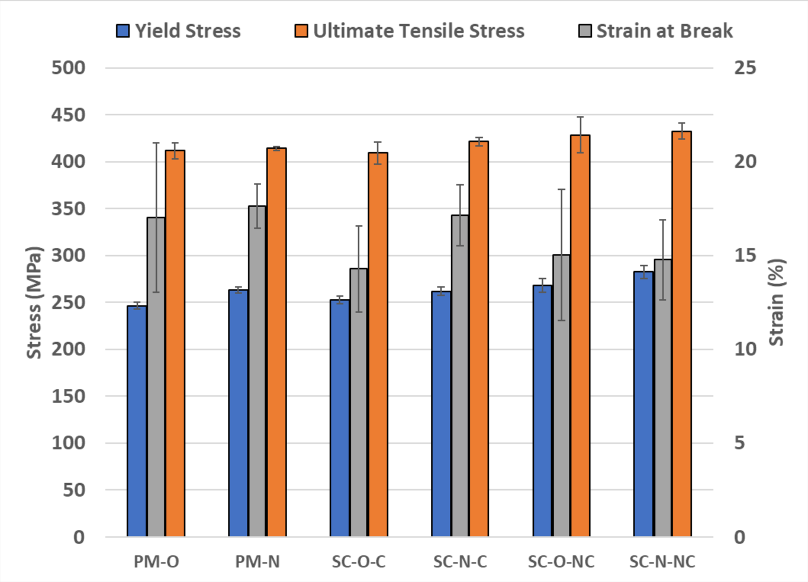

Figure 80: Histogram plot of the yield stress, ultimate tensile stress, and strain at break of the A206-T6 samples prior to SCC testing. PM = Permanent Mold, SC = Sand Cast, O = Original (i.e. without nano particles), N = With nano particles, NC = No chill.

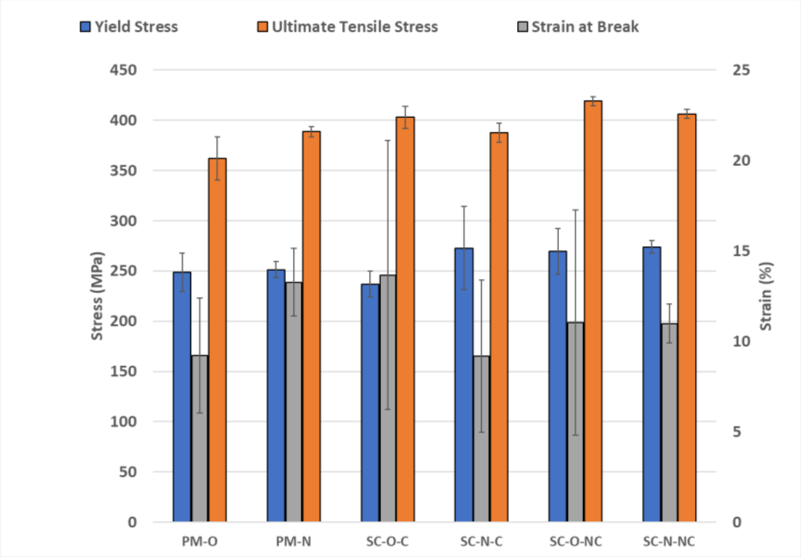

Figure 81: Histogram plot of the yield stress, ultimate tensile stress, and strain at break of the A206-T6 samples after SCC testing.

7.3 Microstructural Analysis

7.3.1 Optical Analysis

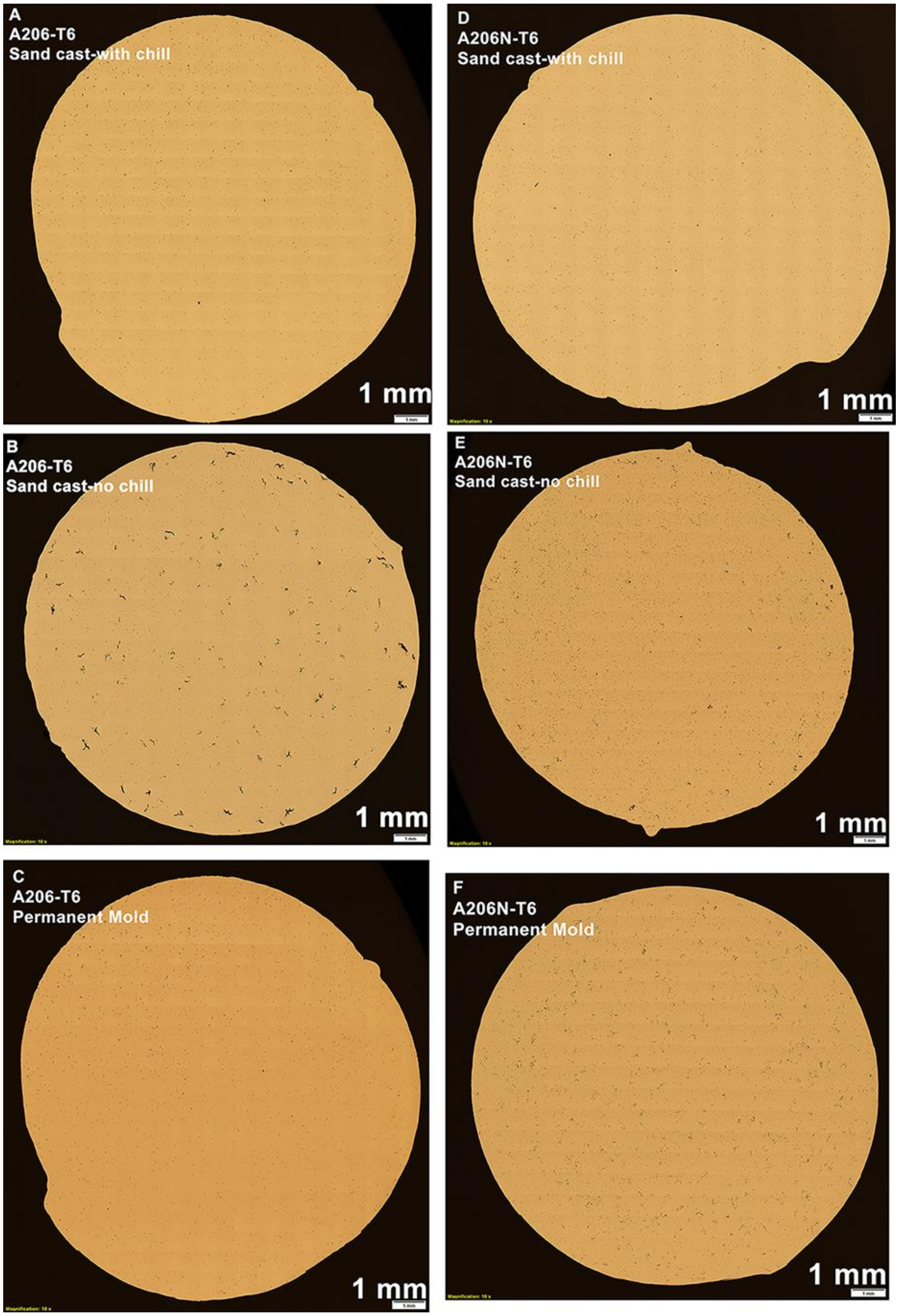

Figure 82: Optical micrograph montage images of cross-sections of each of the A206-T6 alloys in the as-received condition.

7.3.2 SEM Feature Analysis

7.3.2.1 Sand Cast with chill

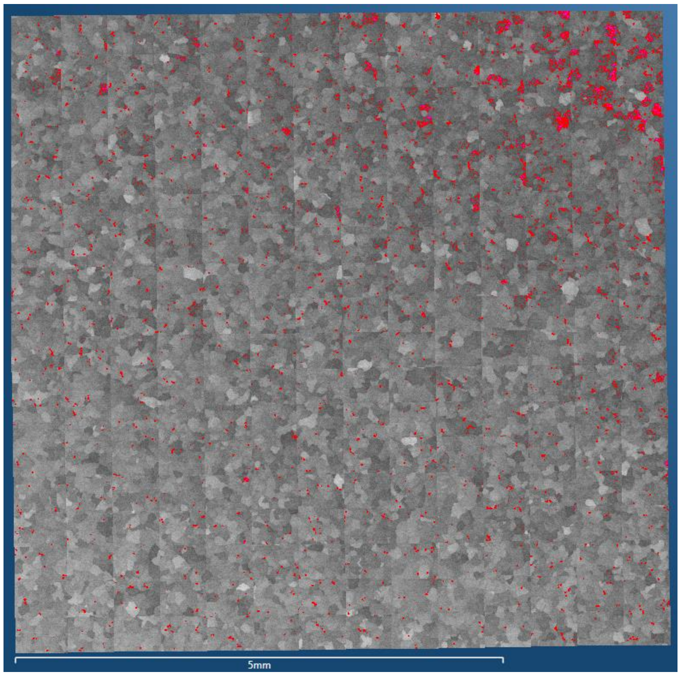

Figure 83: SEM(BSE) void Feature analysis of the Sand Cast with chill sample. Thresholding of the contrast indicates pores in the sample (red areas).

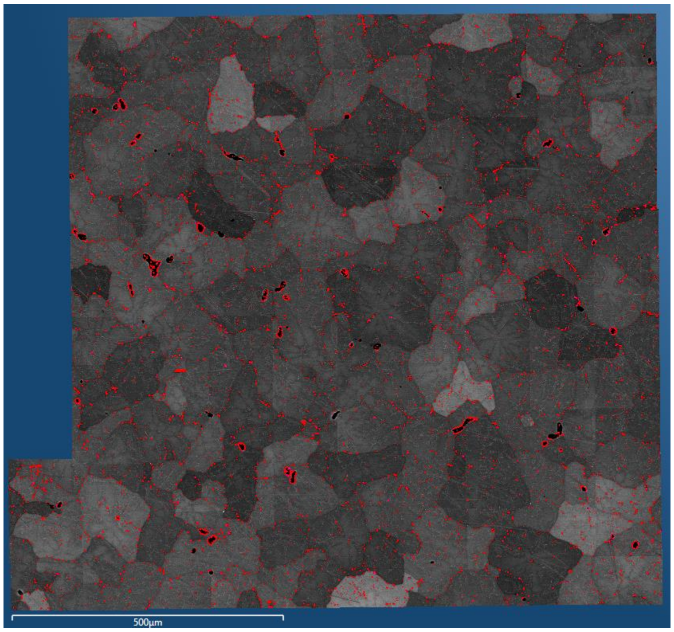

Figure 84: SEM(BSE) grain boundary precipitate Feature analysis of the Sand Cast with chill sample. Thresholding of the contrast indicates precipitates in the sample (red areas).

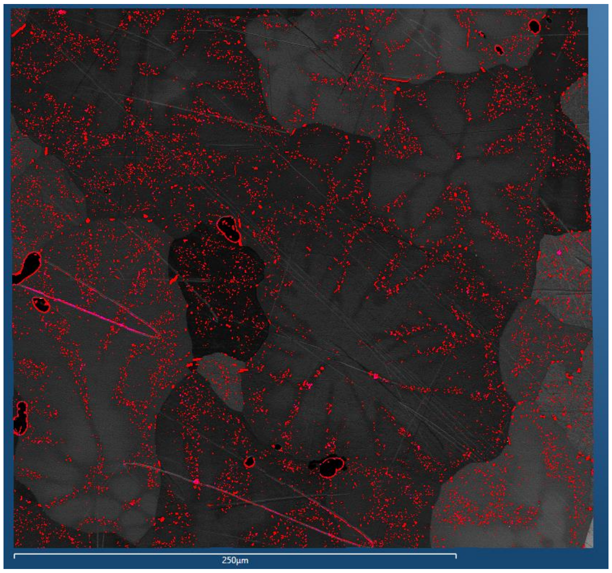

Figure 85: SEM(BSE) transgranular precipitate Feature analysis of the Sand Cast with chill sample. Thresholding of the contrast indicates precipitates in the sample (red areas).

7.3.2.2 Sand Cast with chill nano

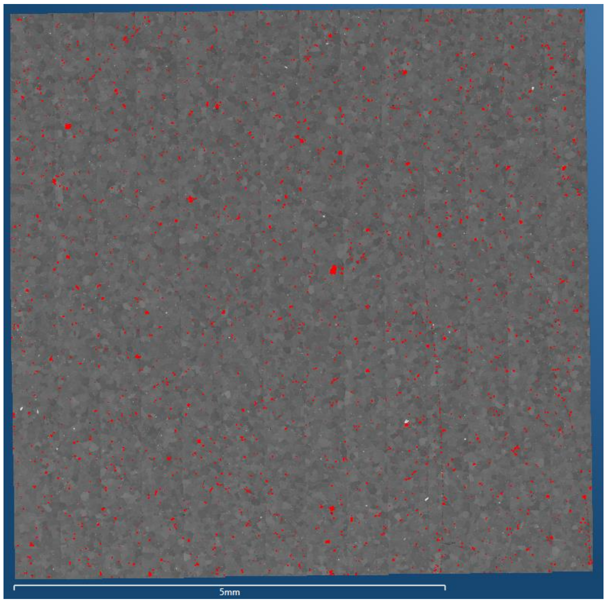

Figure 86: SEM(BSE) void Feature analysis of the Sand Cast with chill nano sample. Thresholding of the contrast indicates pores in the sample (red areas).

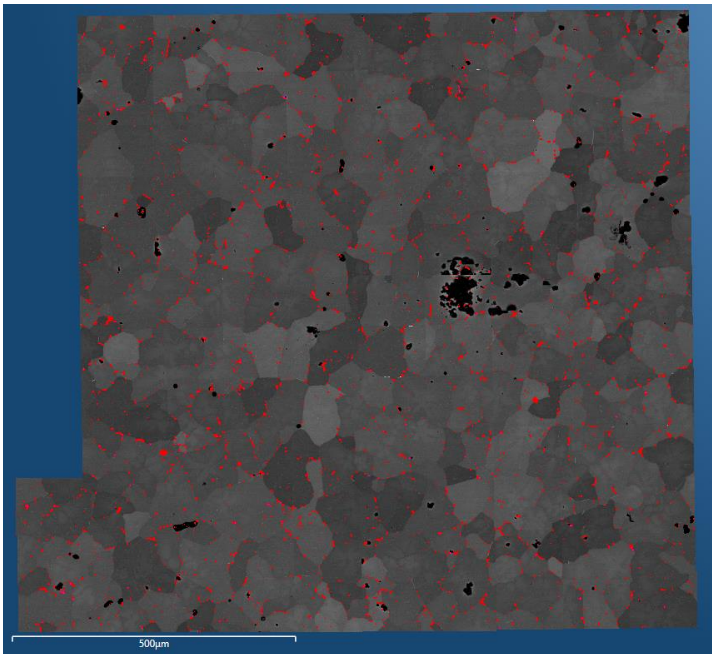

Figure 87: SEM(BSE) grain boundary precipitate Feature analysis of the Sand Cast with chill nano sample. Thresholding of the contrast indicates precipitates in the sample (red areas).

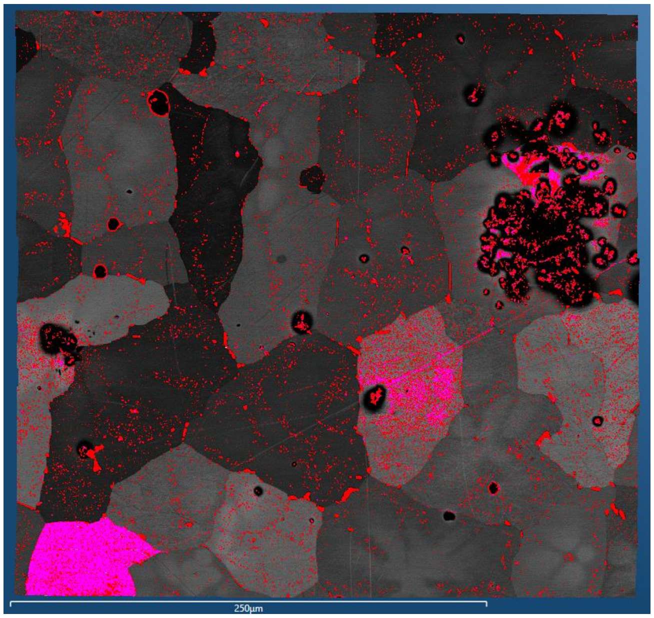

Figure 88: SEM(BSE) transgranular precipitate Feature analysis of the Sand Cast with chill nano sample. Thresholding of the contrast indicates precipitates in the sample (red areas).

7.3.2.3 Sand Cast no chill

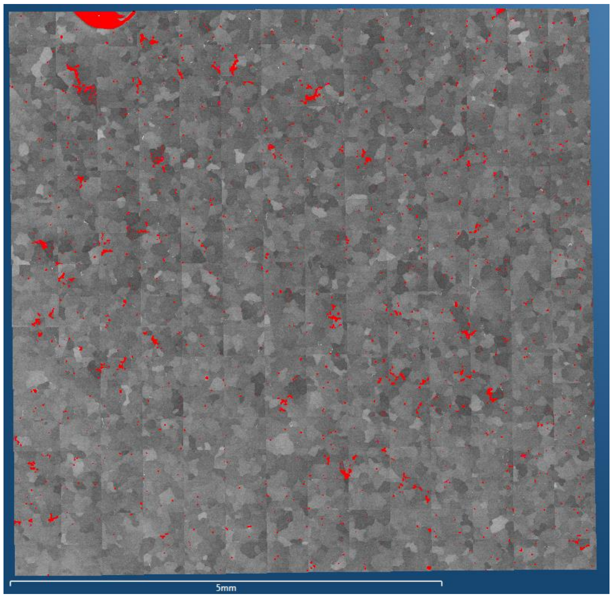

Figure 89: SEM(BSE) void Feature analysis of the Sand Cast no chill sample. Thresholding of the contrast indicates pores in the sample (red areas).

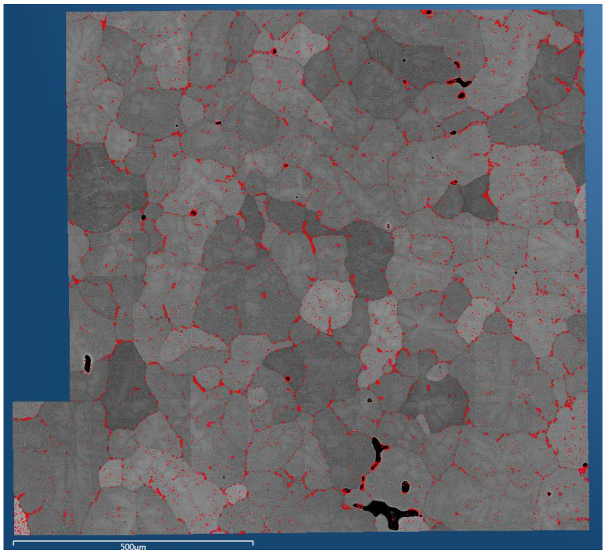

Figure 90: SEM(BSE) grain boundary precipitate Feature analysis of the Sand Cast no chill sample. Thresholding of the contrast indicates precipitates in the sample (red areas).

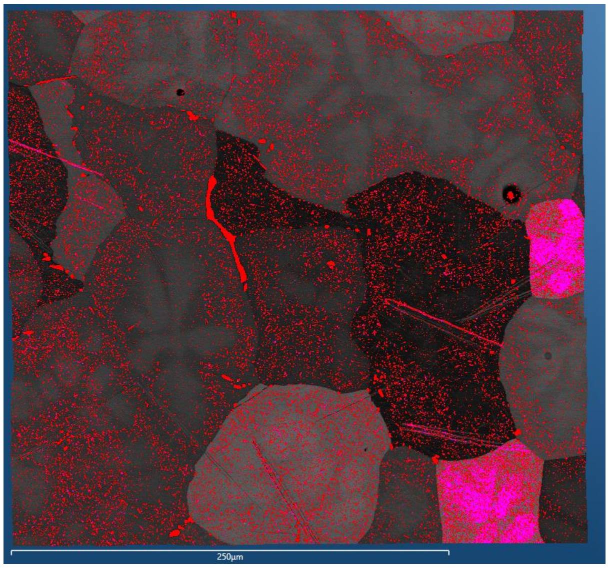

Figure 91: SEM(BSE) transgranular precipitate Feature analysis of the Sand Cast no chill sample. Thresholding of the contrast indicates precipitates in the sample (red areas).

7.3.2.4 Sand Cast no chill nano

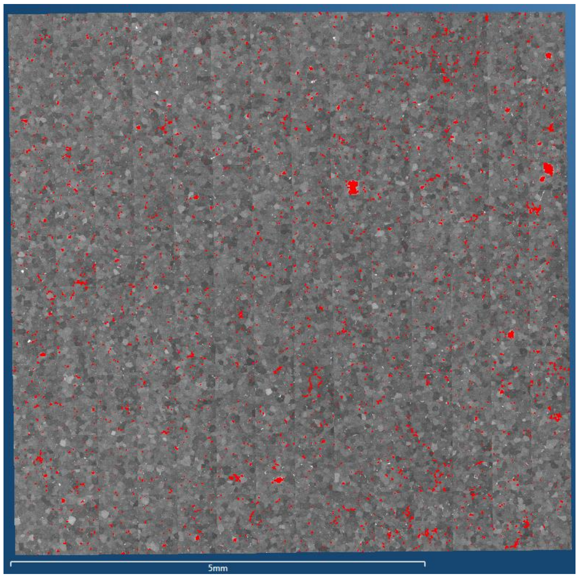

Figure 92: SEM(BSE) void Feature analysis of the Sand Cast no chill nano sample. Thresholding of the contrast indicates pores in the sample (red areas).

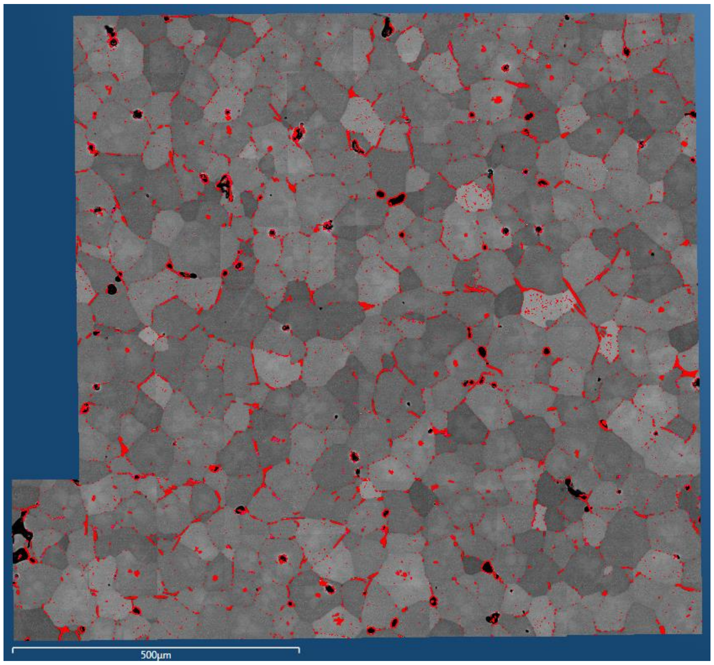

Figure 93: SEM(BSE) grain boundary precipitate Feature analysis of the Sand Cast no chill nano sample. Thresholding of the contrast indicates precipitates in the sample (red areas).

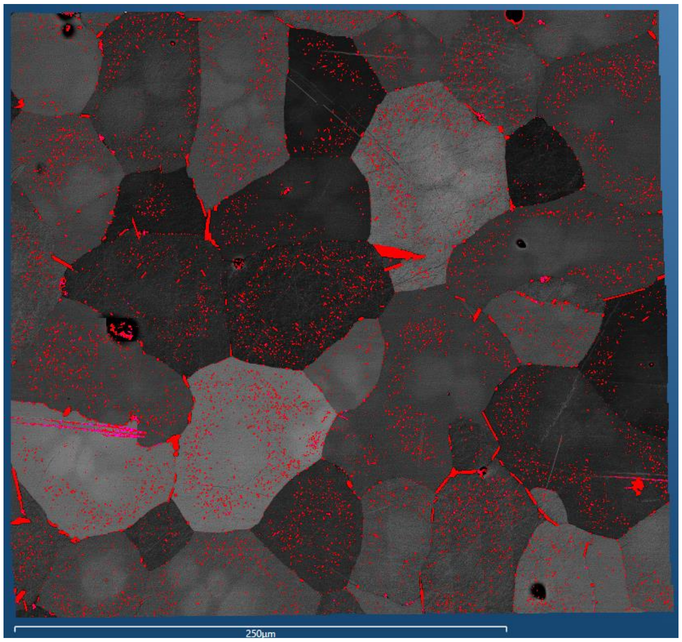

Figure 94: SEM(BSE) transgranular precipitate Feature analysis of the Sand Cast no chill nano sample. Thresholding of the contrast indicates precipitates in the sample (red areas).

7.3.2.5 SEM: Sand Cast With Chill (A, D)

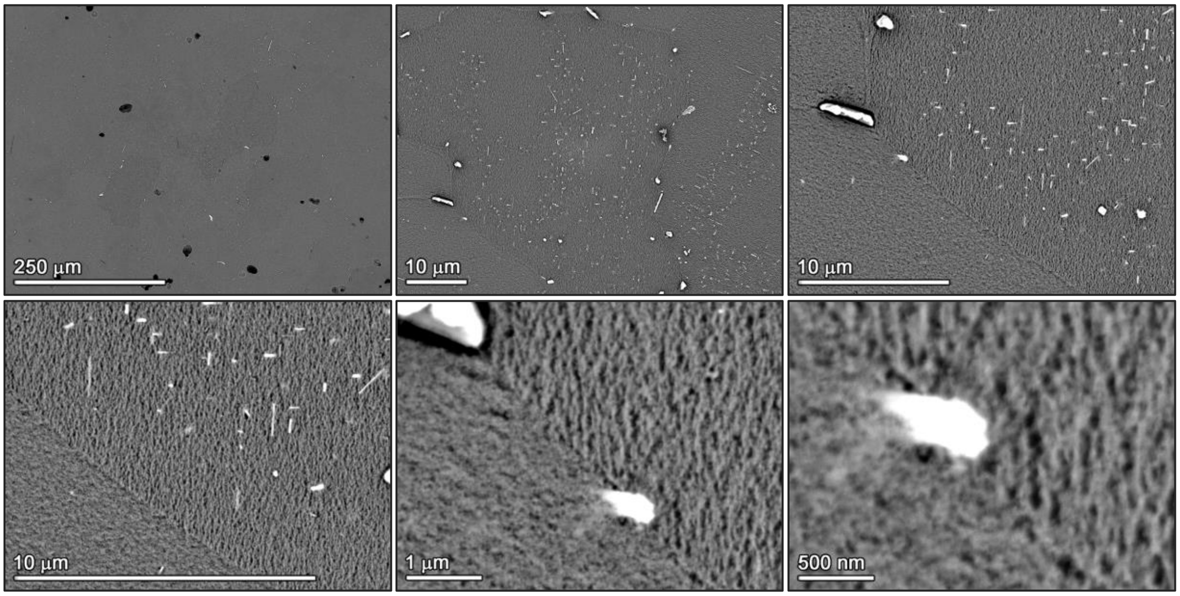

Figure 95: SEM(BSE) images of the representative microstrucuture of the Sand Cast with chill sample.

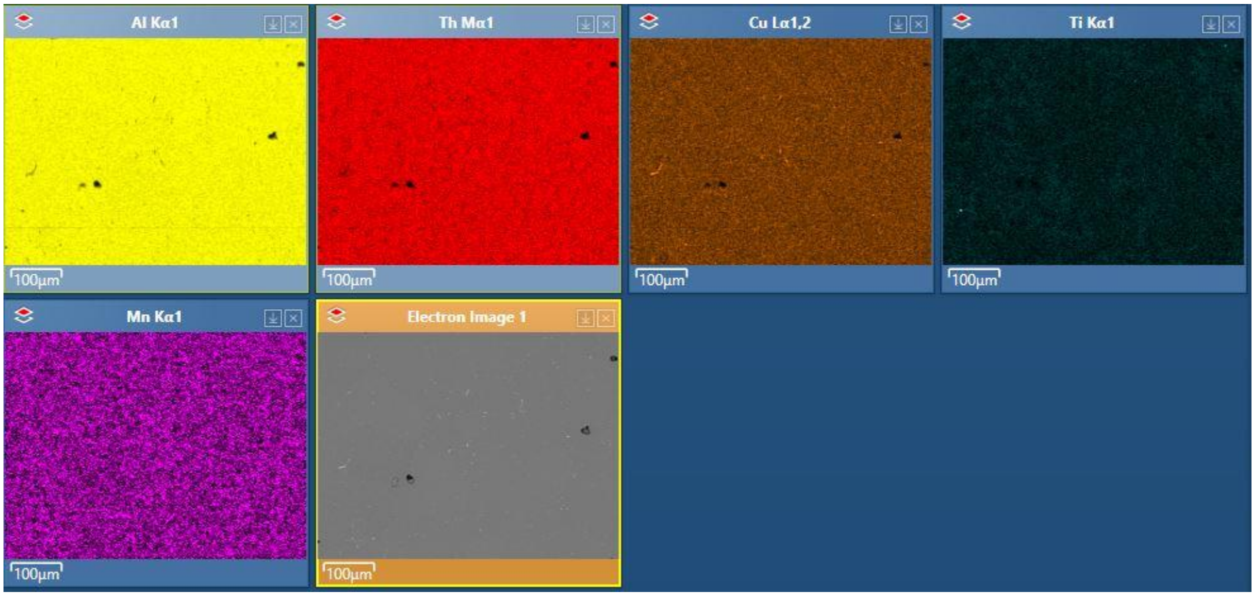

Figure 96: SEM(BSE) image and EDS elemental maps of the representative microstrucuture of the Sand Cast with chill sample.

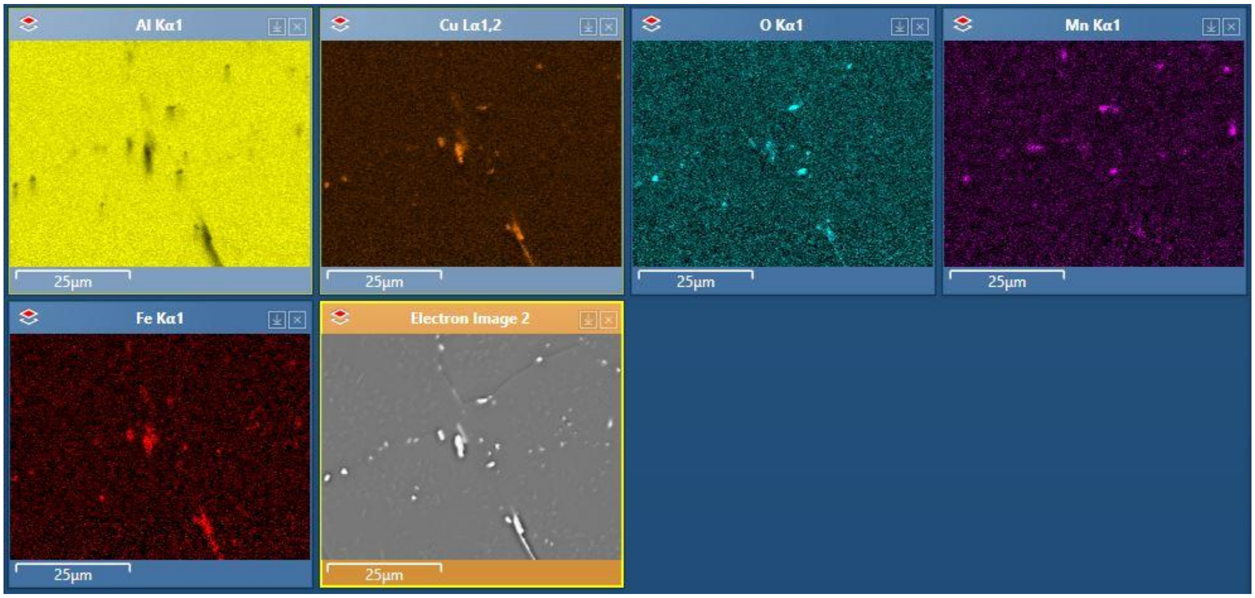

Figure 97: SEM(BSE) image and EDS elemental maps of the representative microstrucuture of the Sand Cast with chill sample.

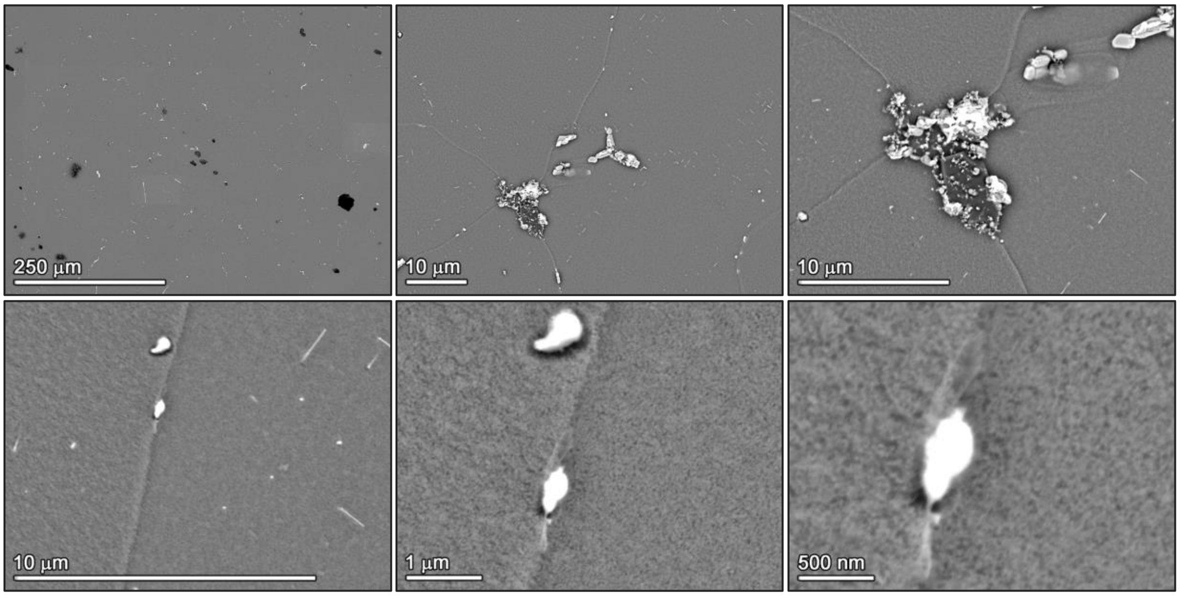

Figure 98: SEM(BSE) images of the representative microstrucuture of the Sand Cast with chill nano sample.

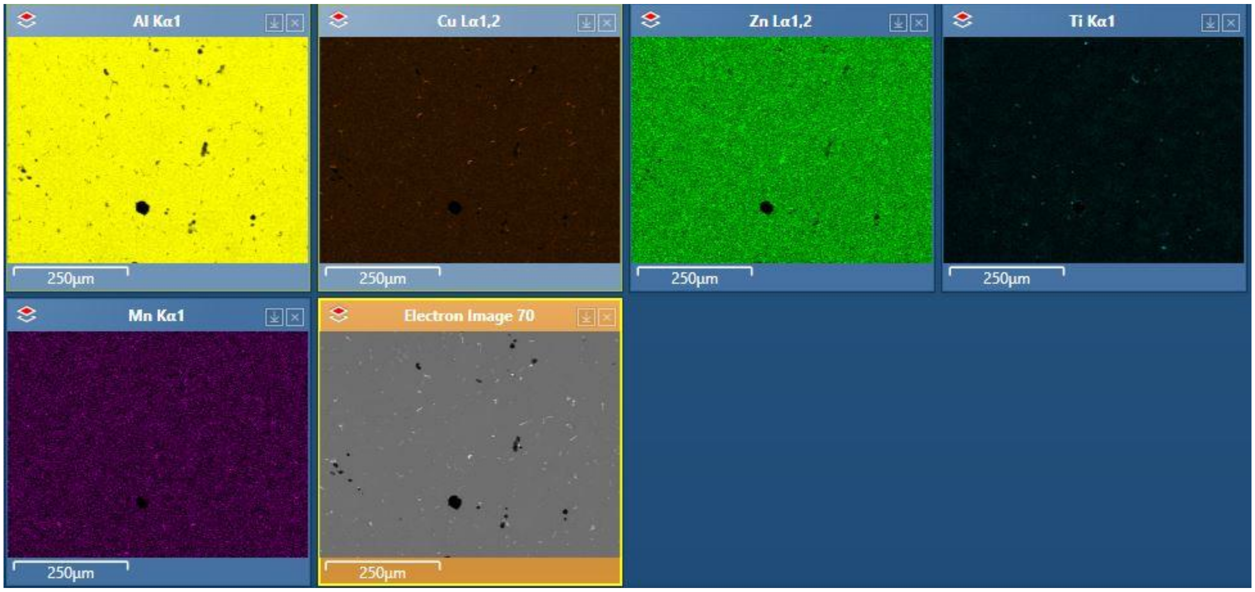

Figure 99: SEM(BSE) image and EDS elemental maps of the representative microstrucuture of the Sand Cast with chill nano sample.

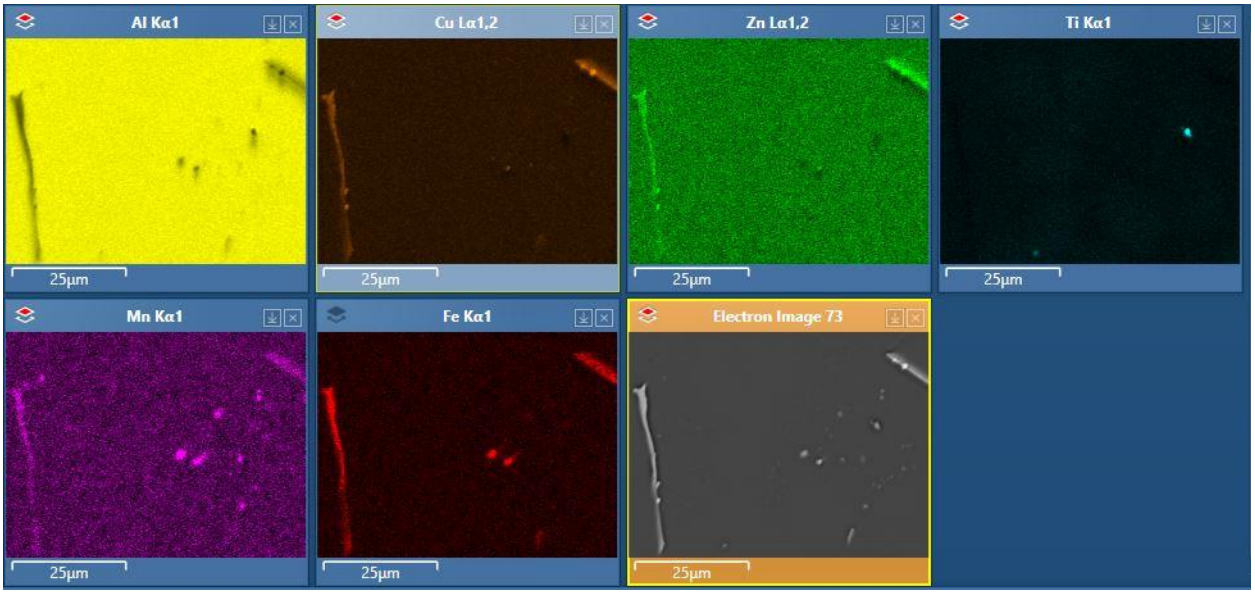

Figure 100: SEM(BSE) image and EDS elemental maps of the representative microstrucuture of the Sand Cast with chill nano sample.

7.3.2.6 S/TEM: Sand Cast With Chill (A, D)

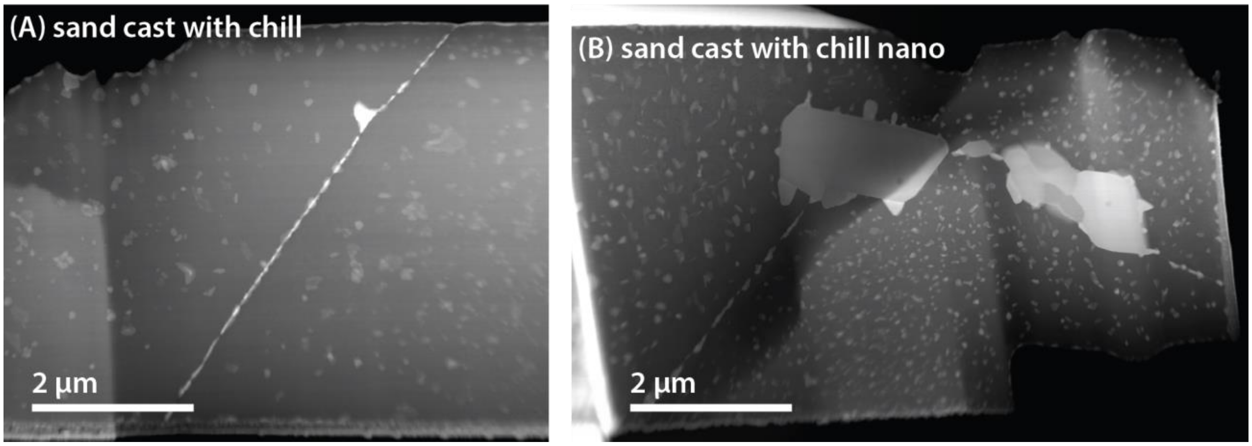

Figure 101: STEM HAADF images showing grain boundary regions in the sample sand cast with chill (sample A) and sand cast with chill nano (sample D). Sample D has a much finer precipitate dispersion than sample A and exhibits much larger (several microns) grain boundary precipitates.

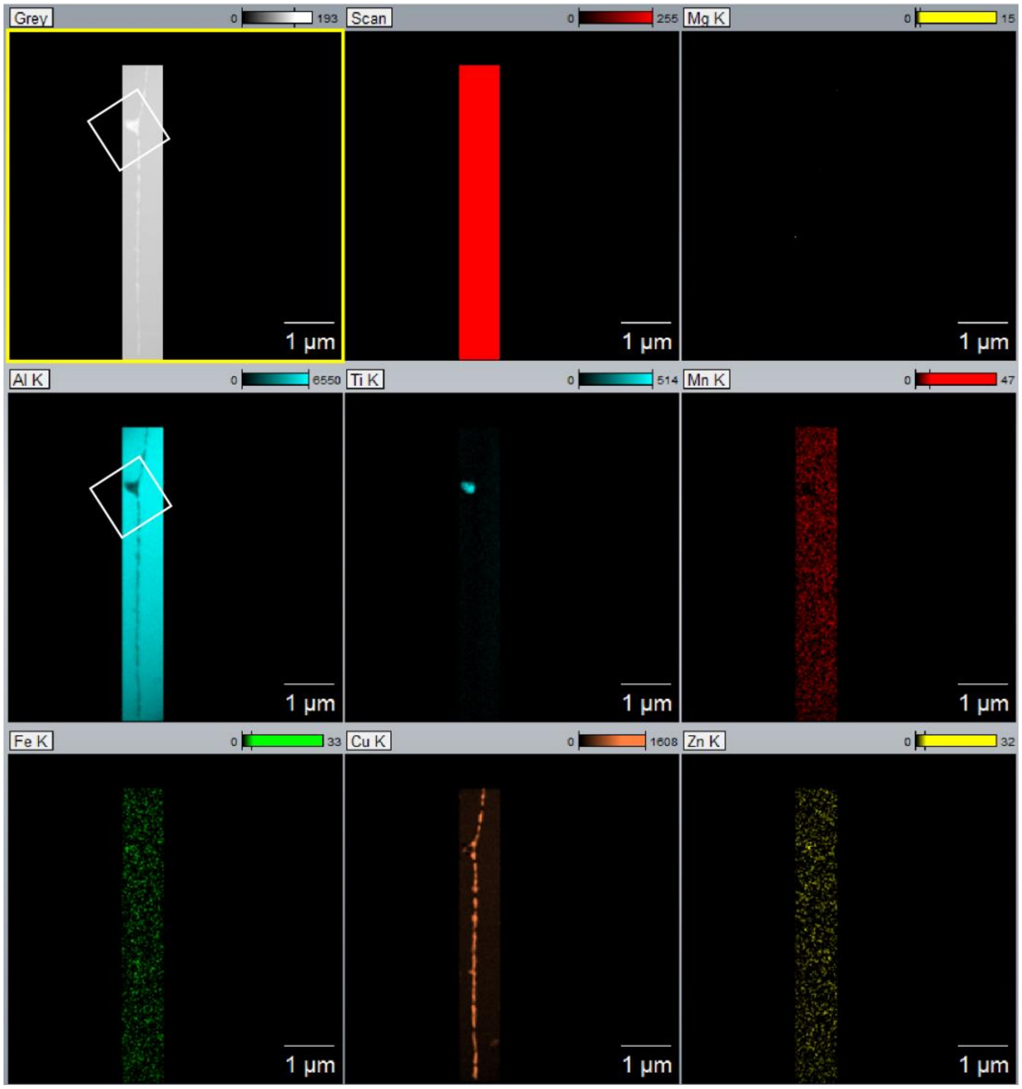

Figure 102: STEM EDS analysis of grain boundary precipitates in the sand cast sample with chill (sample A). The grain boundary is lines with fine Cu-rich precipitates and has one Ti-rich precipitate in the analysis region.

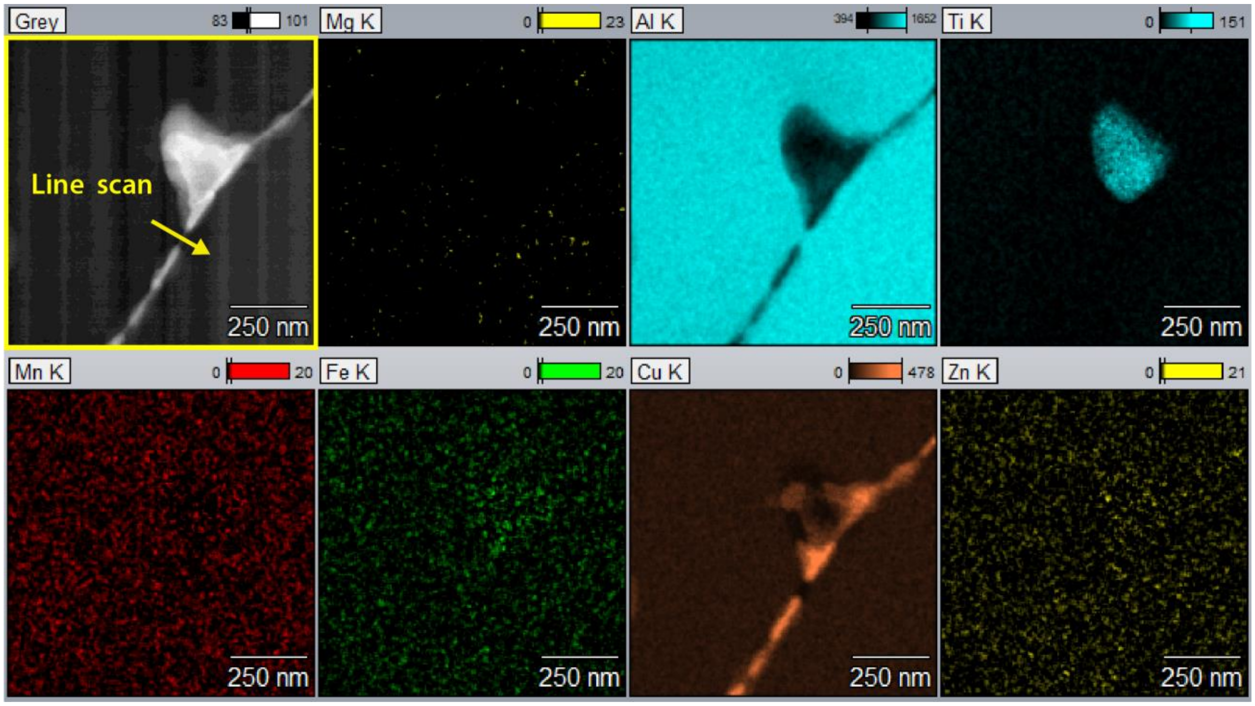

Figure 103: STEM EDS analysis of large Ti-rich precipitate at GB in the sand cast sample with chill (sample A). Both Cu and Al are almost entirely absent in the region of the precipitate. Neither nitrogen nor carbon were detected with the Ti.

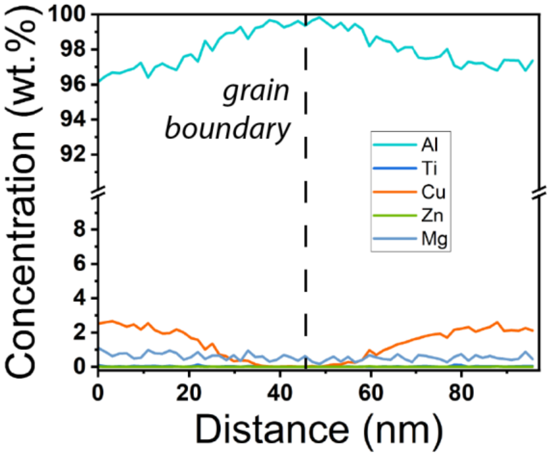

Figure 104: STEM EDS line profile across GB marked in Figure 103 (sample A).

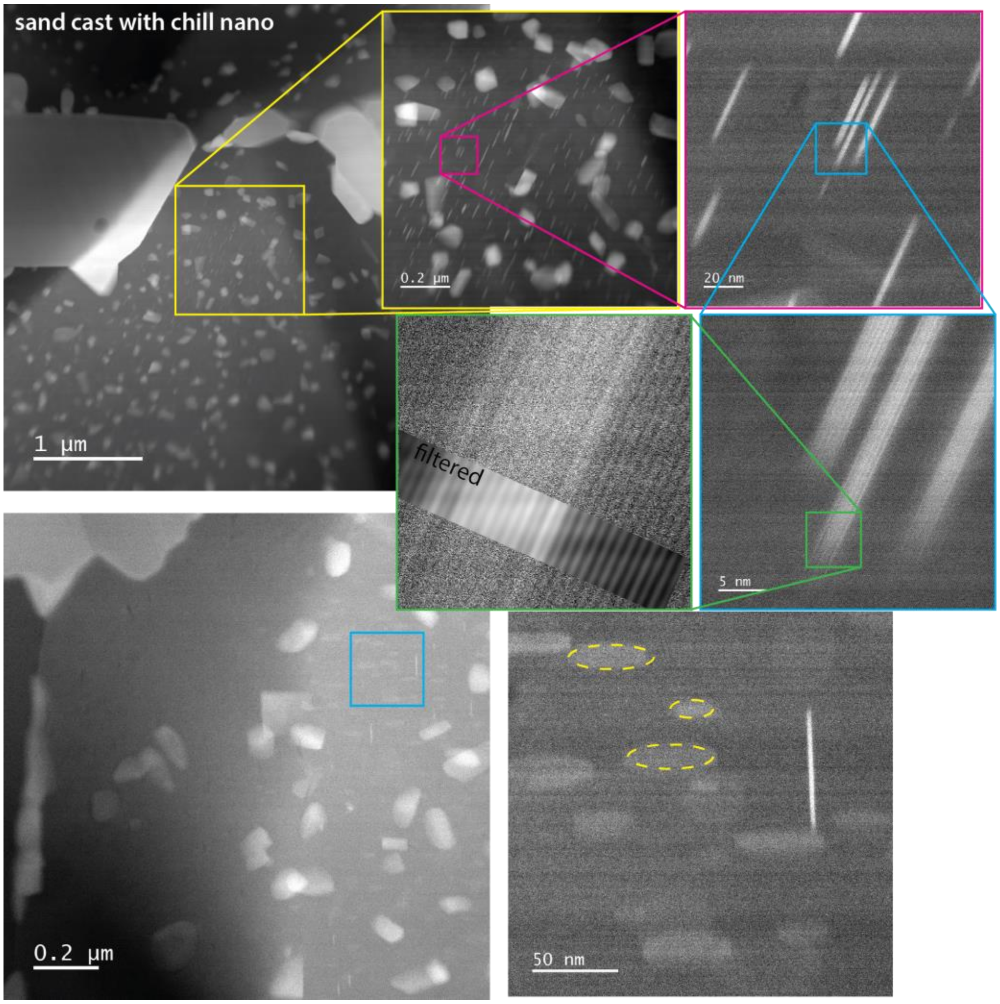

Figure 105: STEM HAADF of the sand cast sample with chill (sample D) showing nanoplatelets of ~10-15 atomic layer thickness in profile in the upper half of the Figure and tilted to reveal their round shape in the lower half.

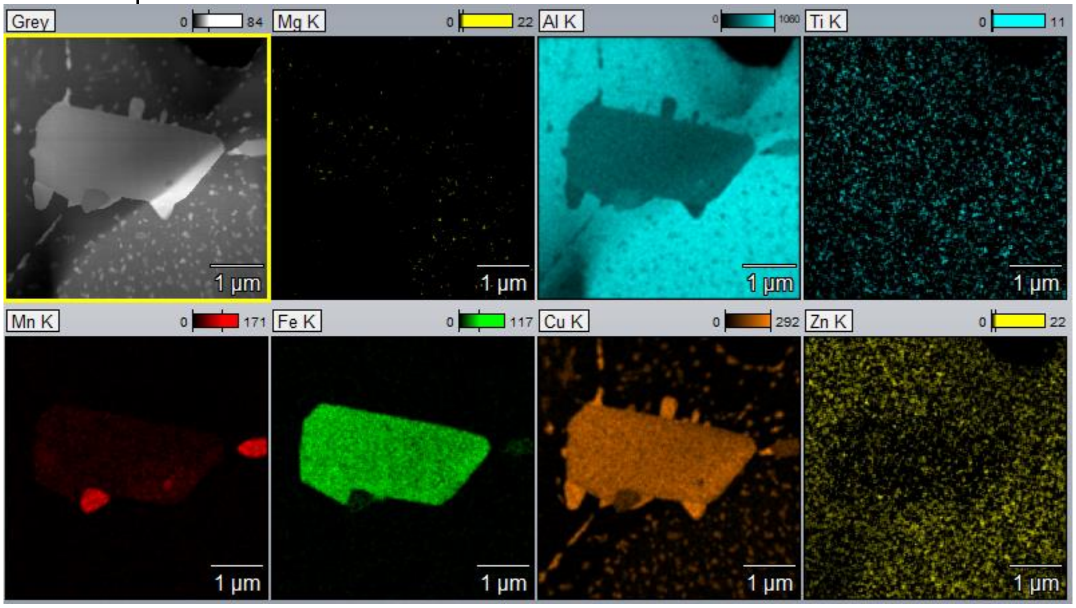

Figure 106: STEM EDS analysis of large precipitate at triple point in the sand cast sample with chill nano (sample D). The largest precipitate is Fe- and Cu-rich and surrounded by Cu- and Mn-rich precipitates. Many small Cu-rich intra granular precipitates can also be observed.

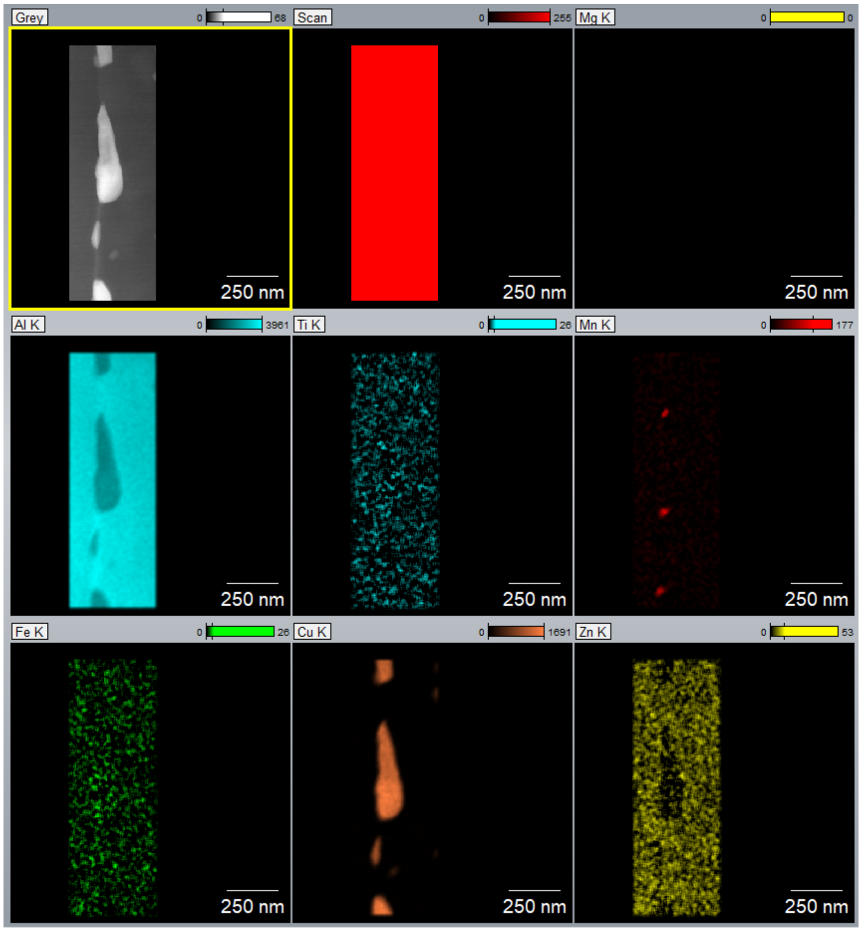

Figure 107: STEM EDS analysis of a selection of GB precipitates in the sand cast sample with chill nano (sample D). Large Cu-rich precipitates interspersed with small Mn-rich precipitates.

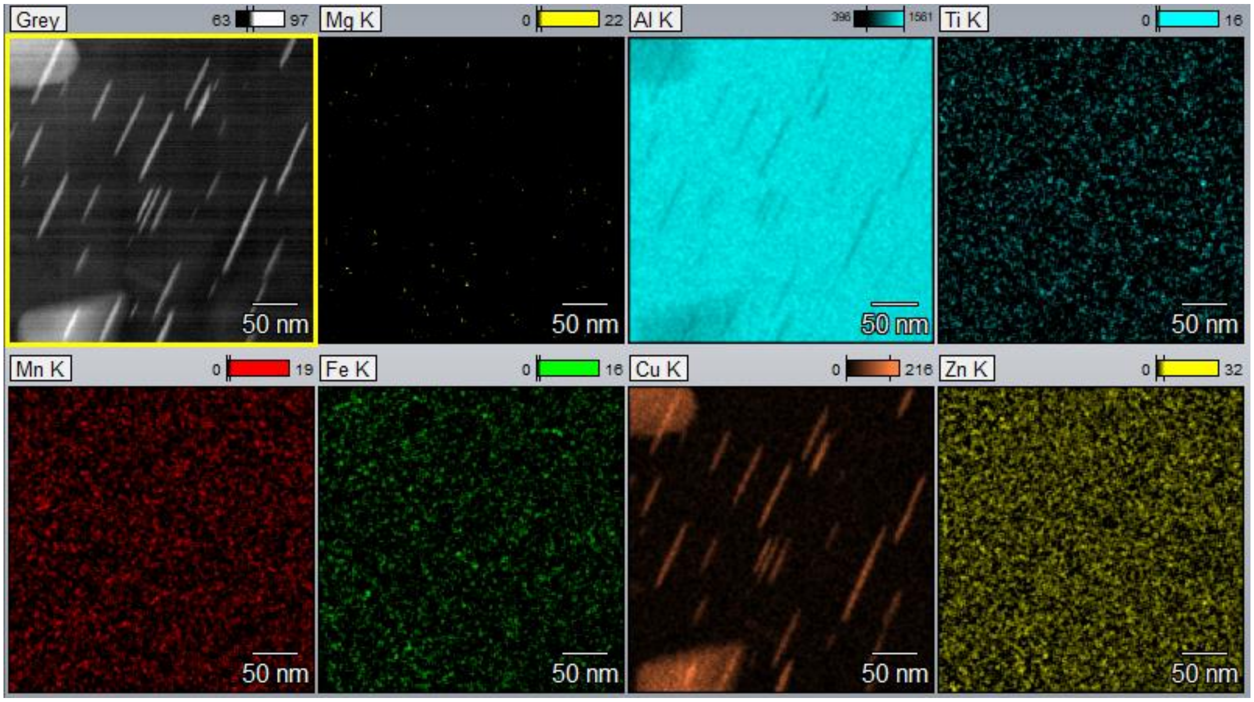

Figure 108: STEM EDS analysis of the nano platelets in the sand cast sample with chill nano (sample D) reveals Cu-enrichment.

7.3.2.7 SEM: Sand Cast No Chill (B, E)

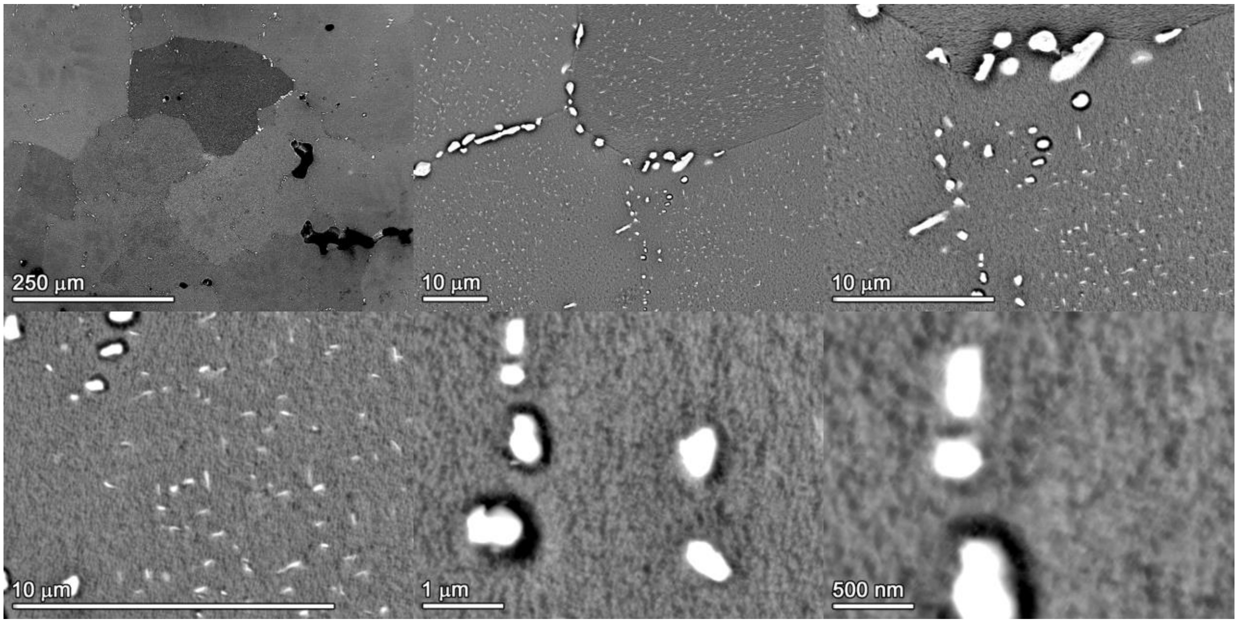

Figure 109: SEM(BSE) images of the representative microstrucuture of the Sand Cast no chill sample.

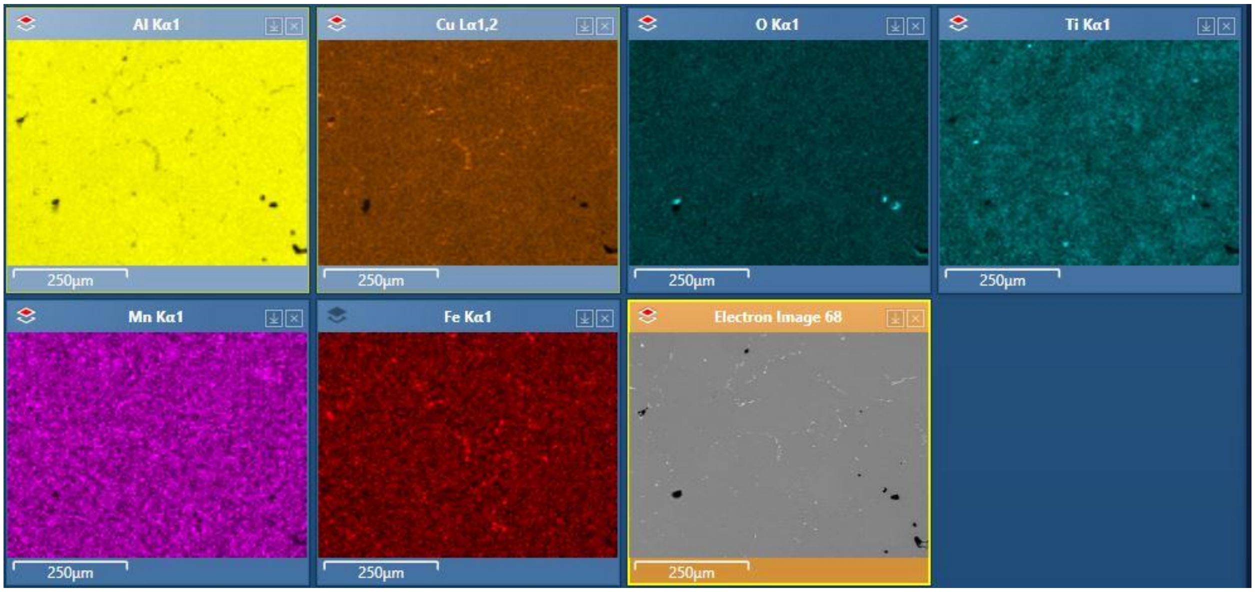

Figure 110: SEM(BSE) image and EDS elemental maps of the representative microstrucuture of the Sand Cast without chill sample.

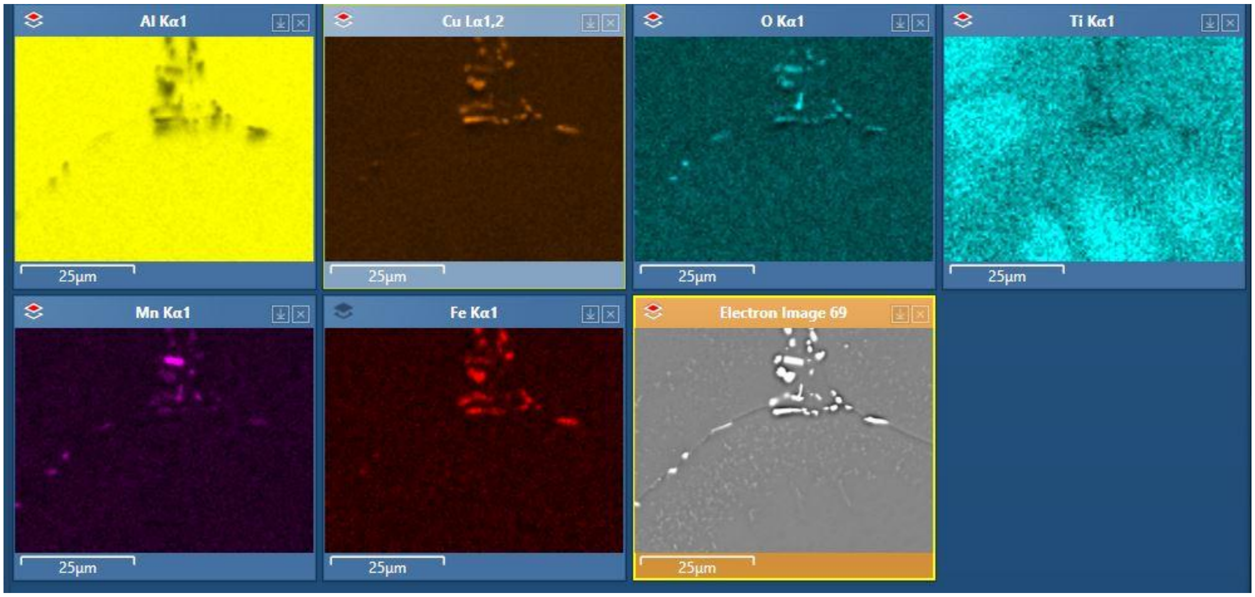

Figure 111: SEM(BSE) image and EDS elemental maps of the representative microstrucuture of the Sand Cast without chill sample.

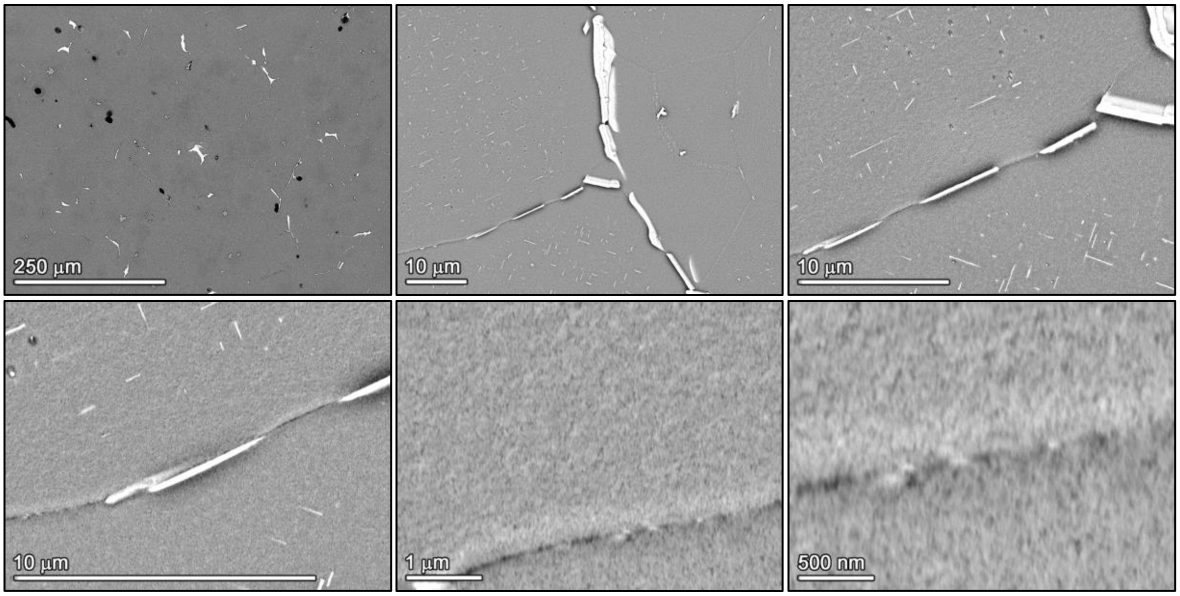

Figure 112: SEM(BSE) images of the representative microstrucuture of the Sand Cast no chill nano sample.

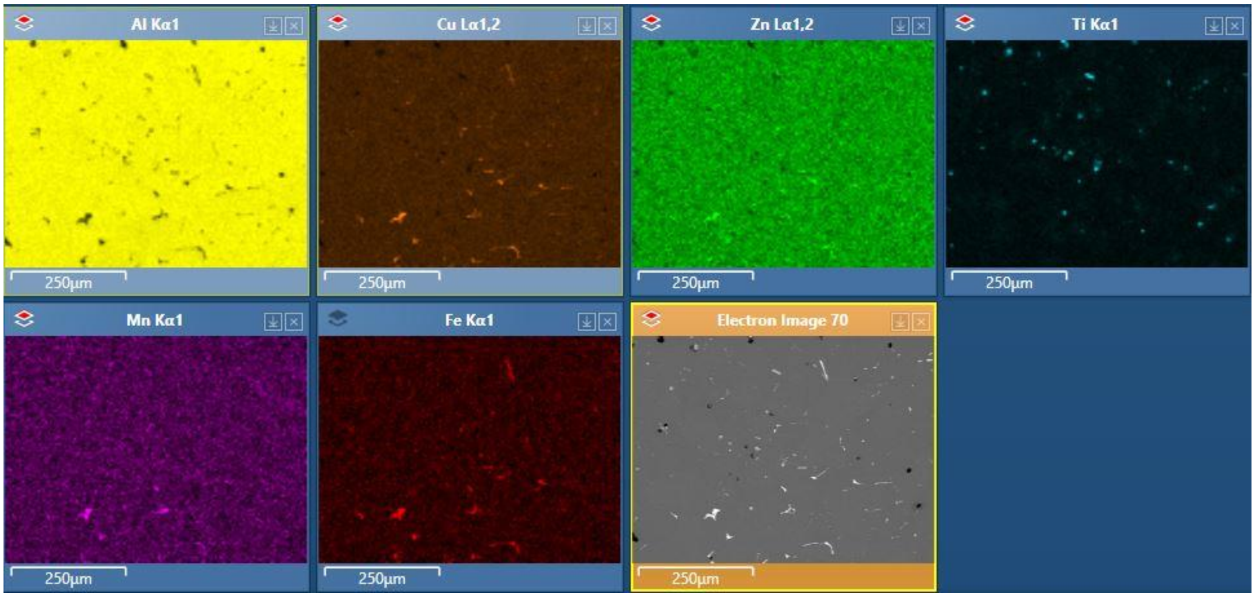

Figure 113: SEM(BSE) image and EDS elemental maps of the representative microstrucuture of the Sand Cast without chill nano sample.

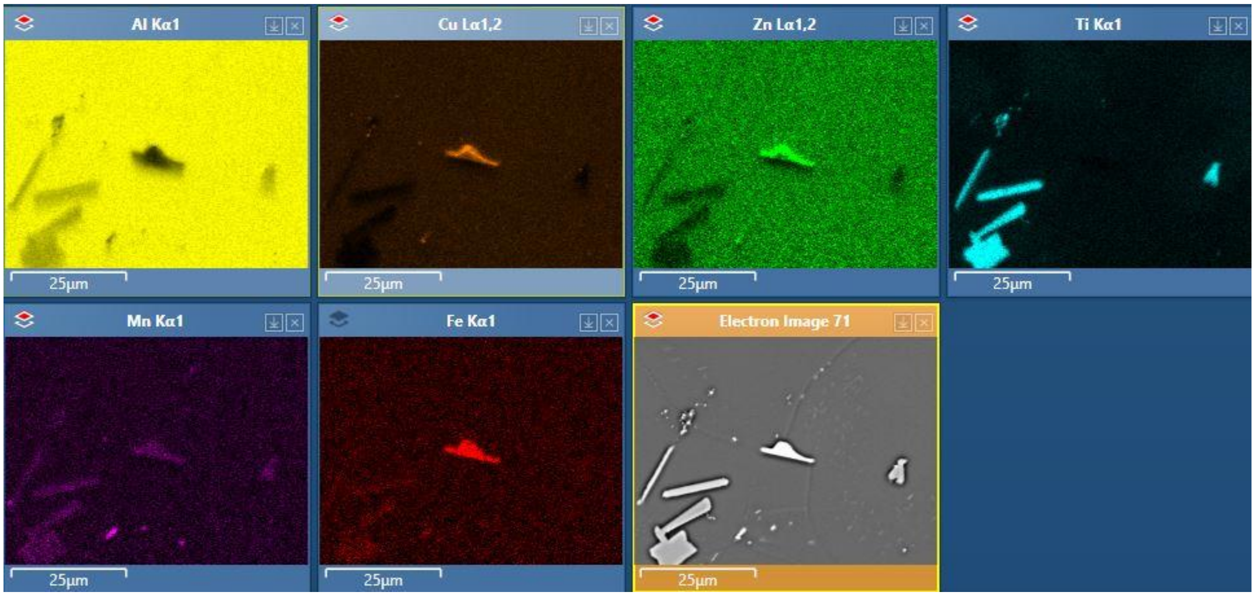

Figure 114: SEM(BSE) image and EDS elemental maps of the representative microstrucuture of the Sand Cast without chill nano sample.

7.3.2.8 S/TEM: Sand Cast No Chill (B, E)

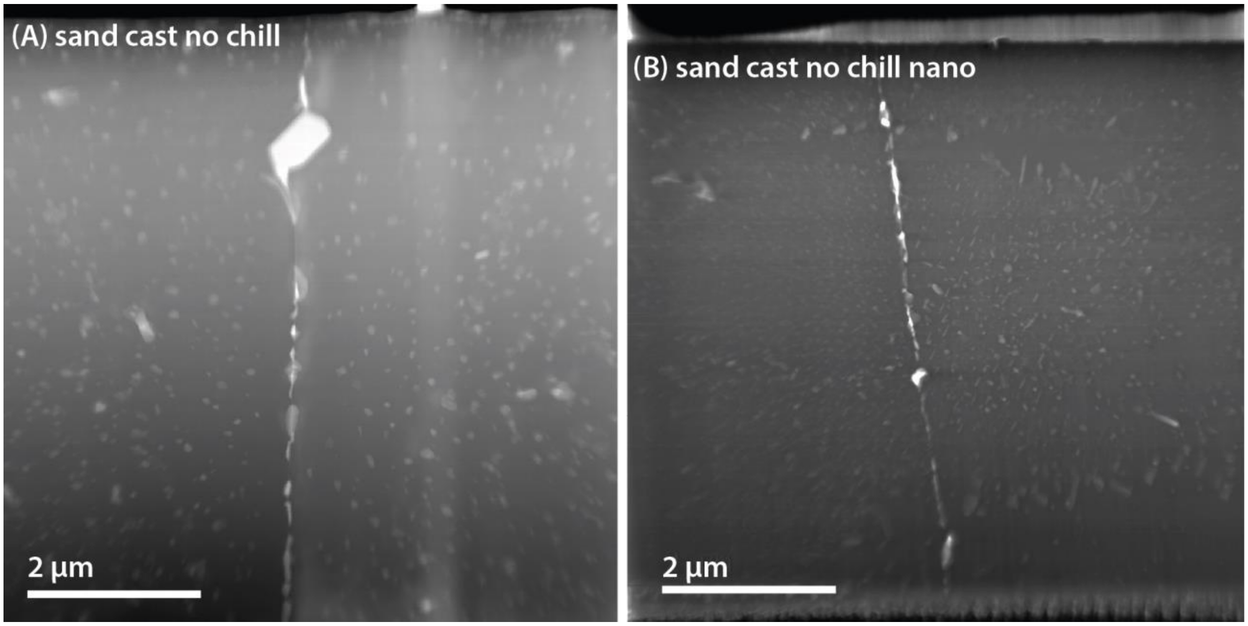

Figure 115: STEM HAADF images showing grain boundary regions in the samples sand cast without chill (sample B) and the sand cast sample with no chill nano (sample E). The precipitate dispersions are more homogenous than in the samples with chill. The nano sample has a finer dispersion and smaller intergranular precipitates at least in the analysis region.

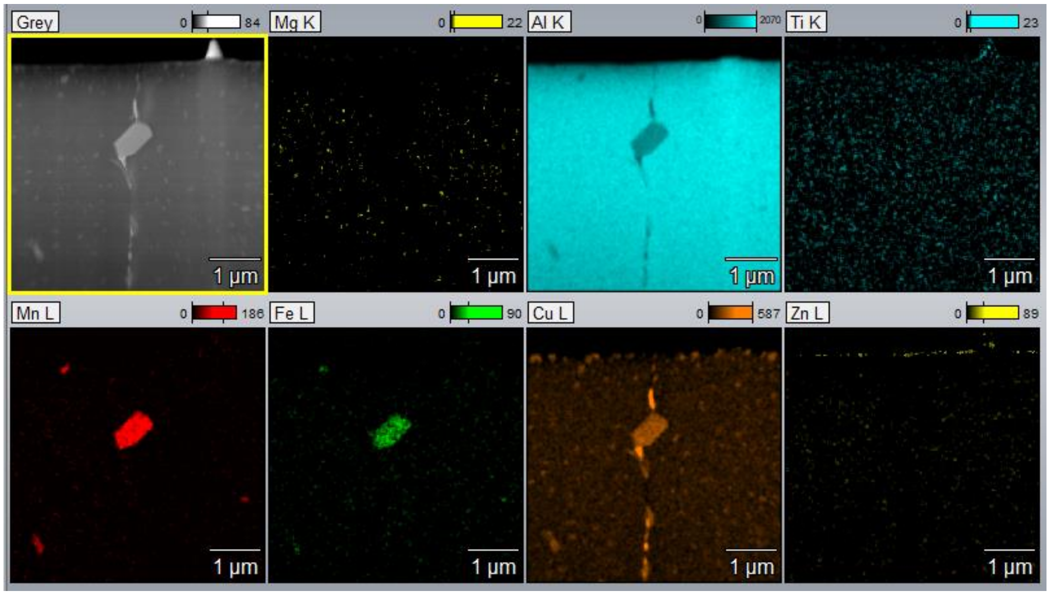

Figure 116: STEM EDS of the grain boundary region in the sand cast sample with no chill (sample B). Fe and Mn-rich precipitates can be found inter- and intragranular. They are larger than Cu-rich inter- and intragranular precipitates.

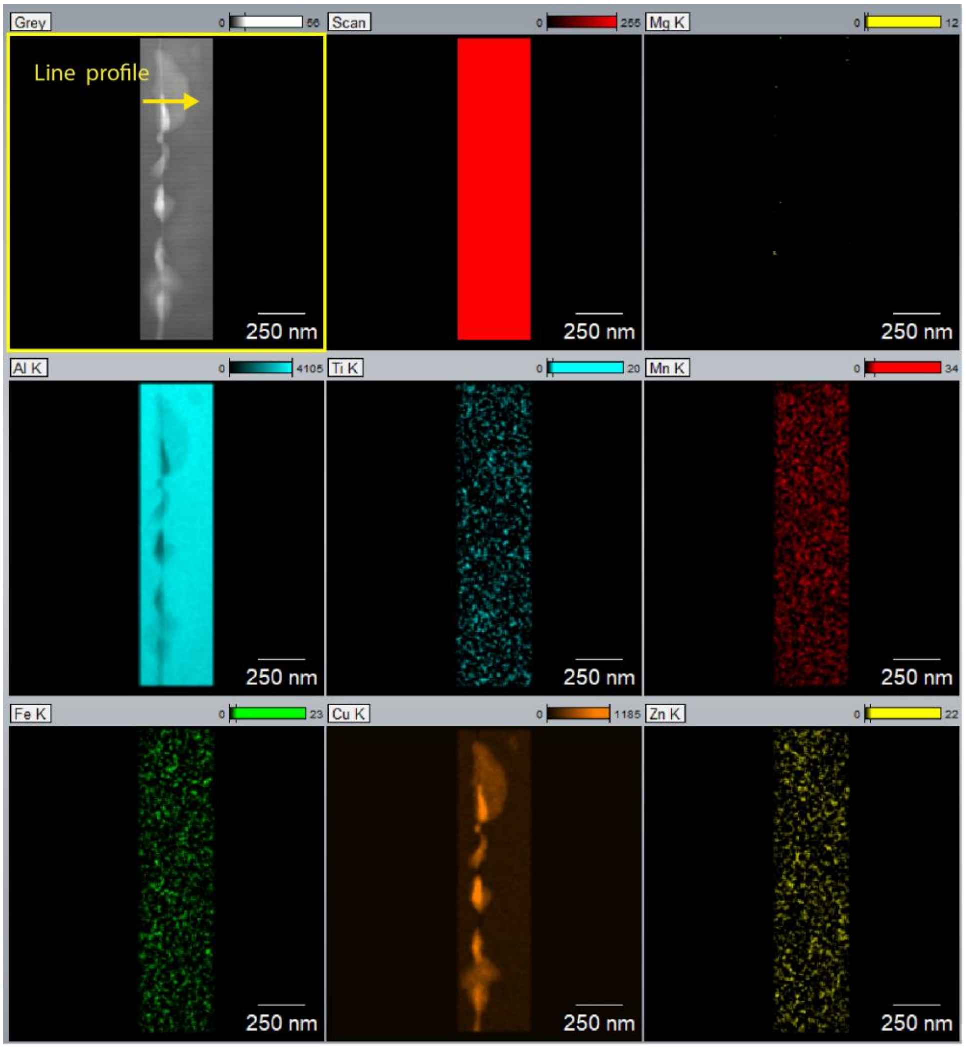

Figure 117: STEM EDS data showing Cu-rich grain boundary precipitates with two distinct compositions in the sand cast sample with no chill (sample B).

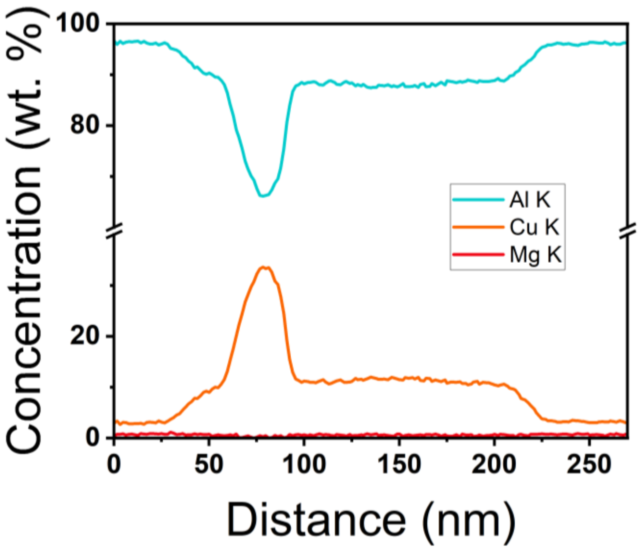

Figure 118: Line profile across Cu-rich grain boundary precipitates, marked in Figure 117, showing precipitates with two distinct compositions present. The center is consistent with a θ-phase ($CuAl_2$), and the outer region exhibits ~10 wt.% Cu.

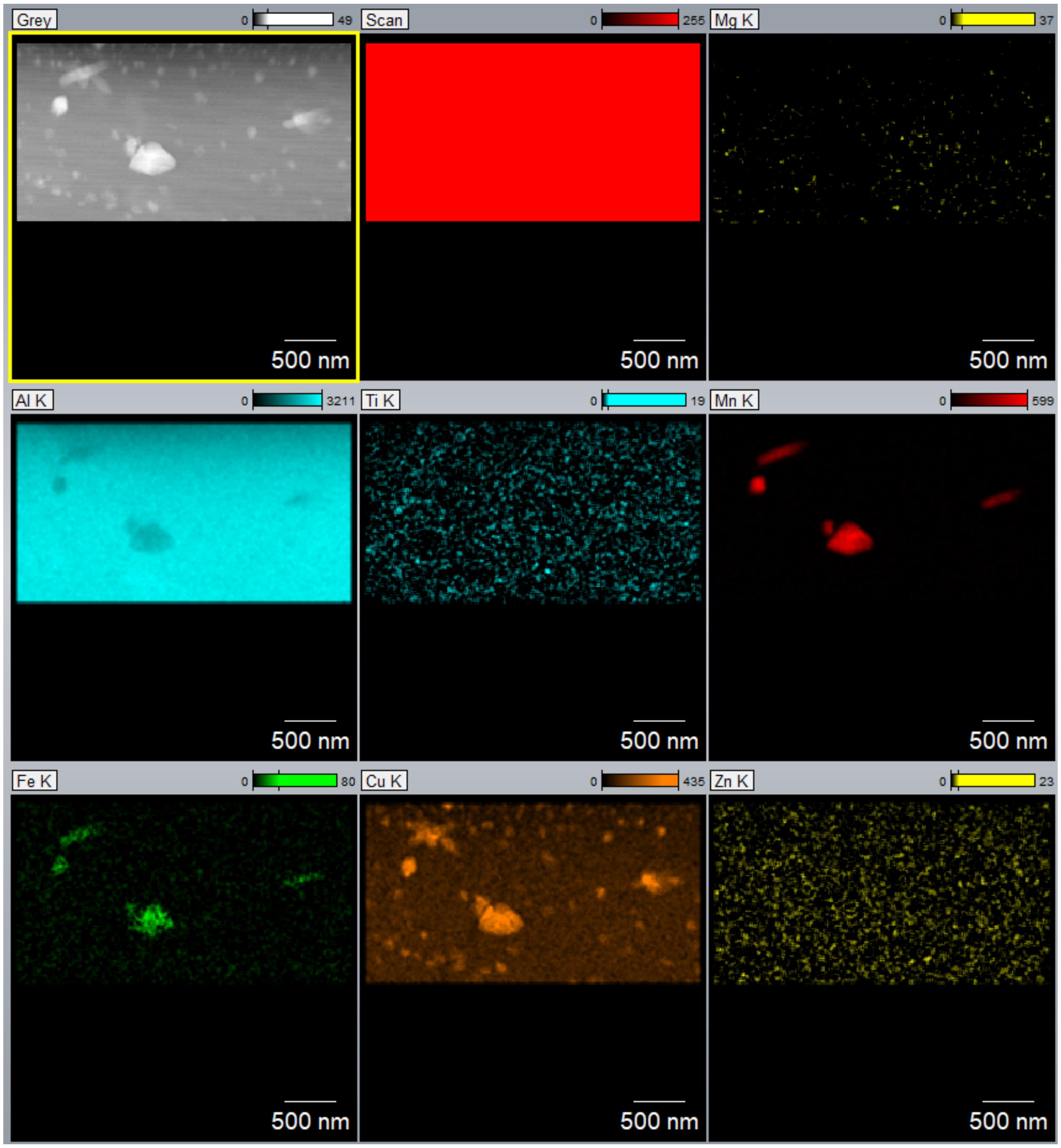

Figure 119: STEM EDS showing intragranular precipitates in the sand cast sample with no chill (sample B). No distinct geometry can be determined. In some cases, stand-alone particles are observed; in other cases, Fe-Mn-Cu-rich precipitates are clustered with Cu-rich precipitates.

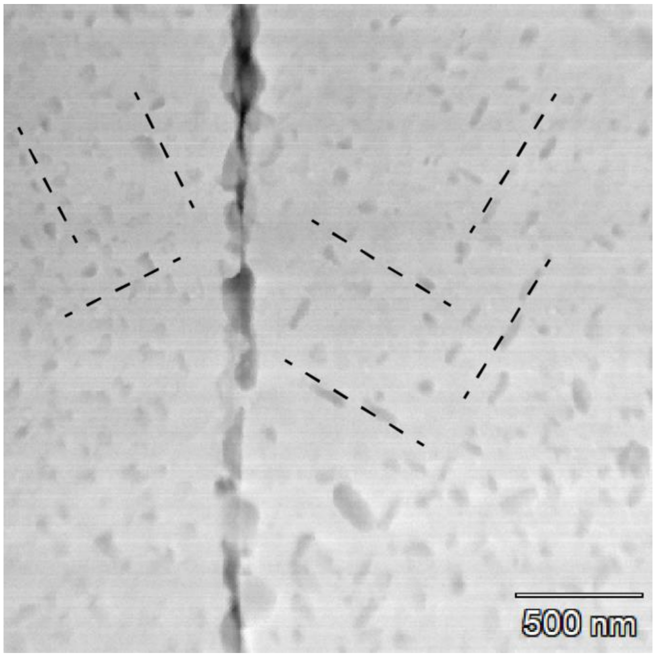

Figure 120: STEM BF image showing the precipitates in each grain of the sand cast sample with no chill nano (sample E) are aligned with the matrix crystal structure.

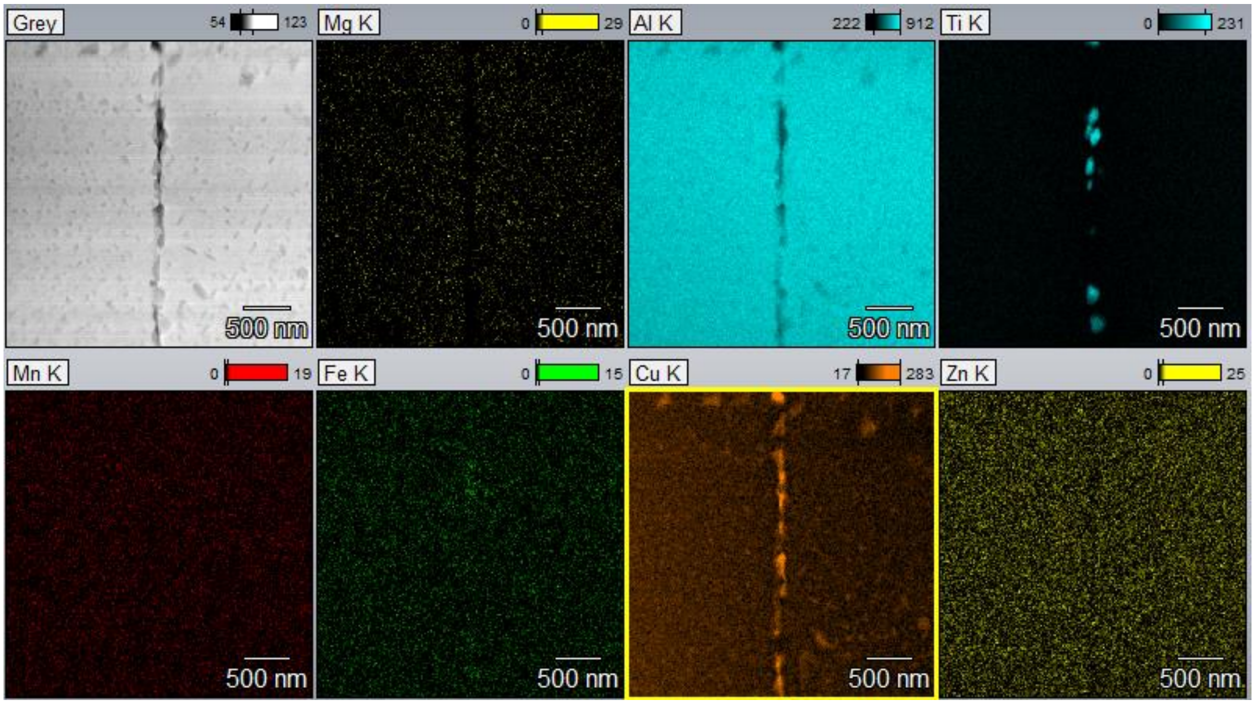

Figure 121: STEM EDS of the sand cast sample with no chill nano (sample E) reveals Ti-rich and Cu-rich precipitates along the grain boundary.

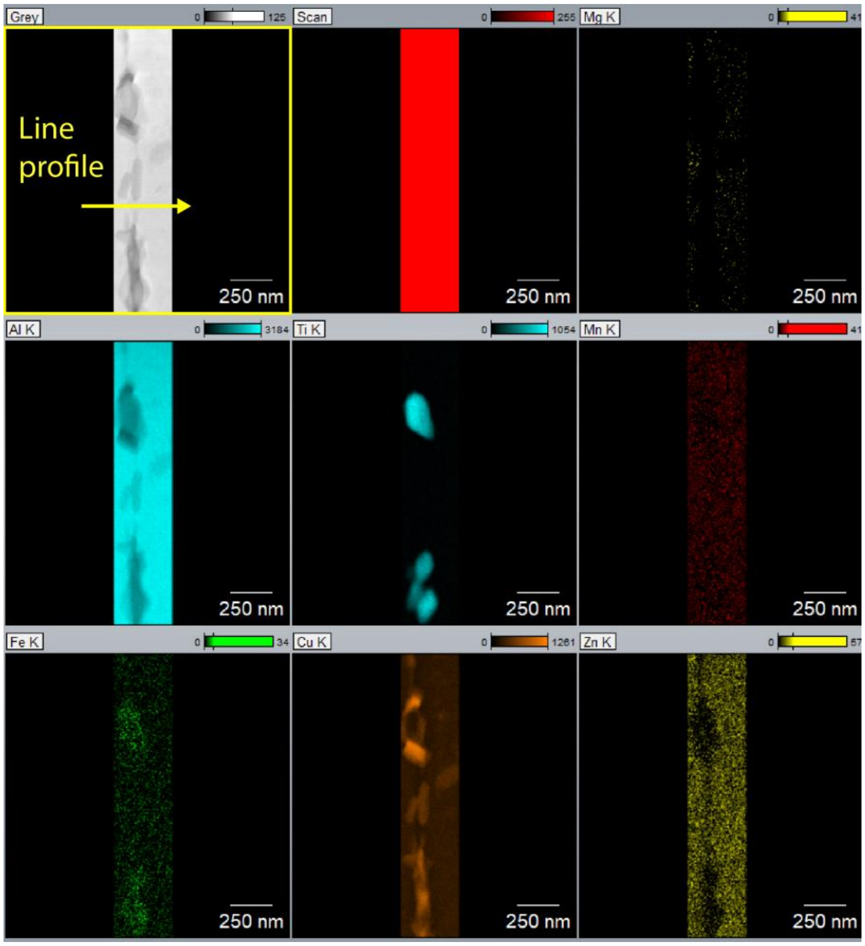

Figure 122: STEM EDS shows Ti-rich precipitates surrounded by a Cu-rich layer and Cu-rich precipitates with different concentrations of Cu at the grain boundary of the sand cast sample with no chill nano (sample E).

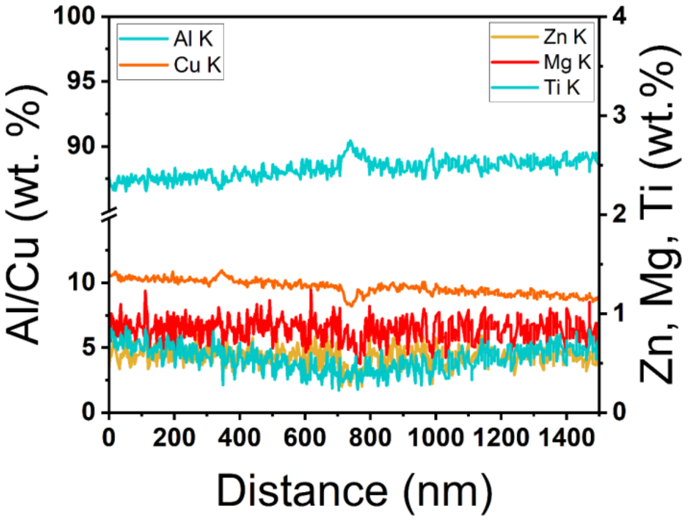

Figure 123: EDS line profile across the GB of the sand cast sample with no chill nano (sample E) as indicated in Figure 122. Cu, Zn and Mg are depleted in a narrow (20 nm) region at the GB; minor Ti depletion is 100’s of nm wide.

7.3.2.9 SEM: Sand Cast With Chill (A, D)

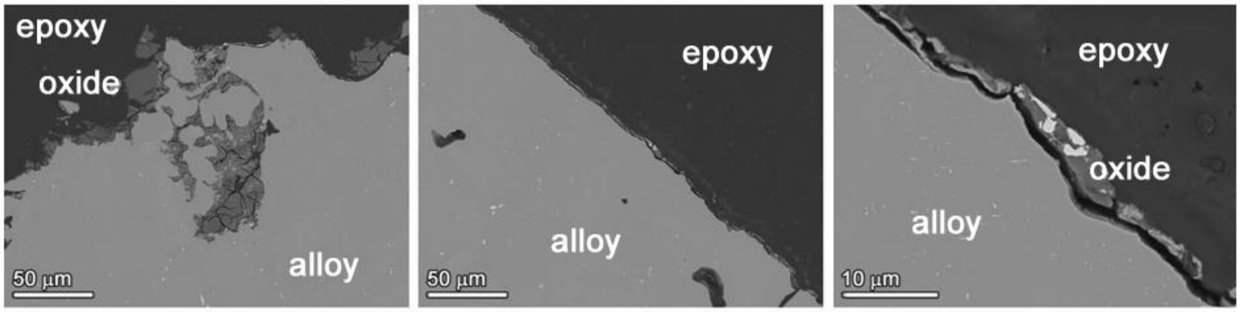

Figure 124: SEM(BSE) micrographs showing general surface corrosion of the Sand Cast with chill sample.

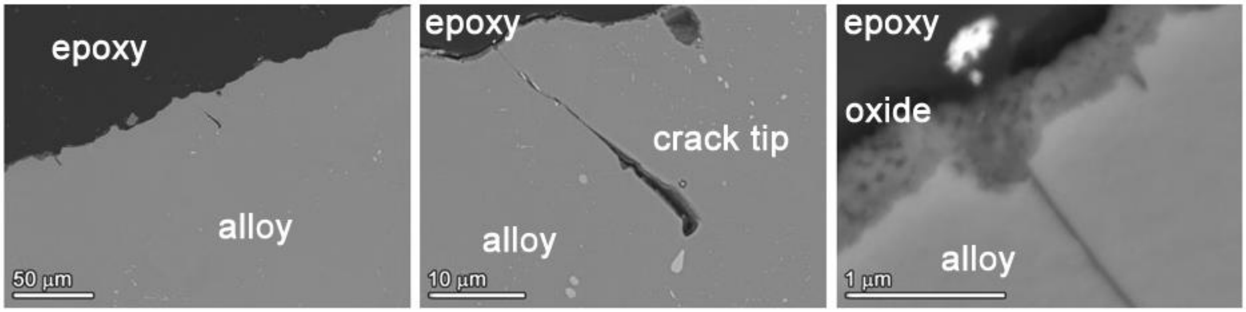

Figure 125: SEM(BSE) micrographs showing SCC cracking of the Sand Cast with chill sample.

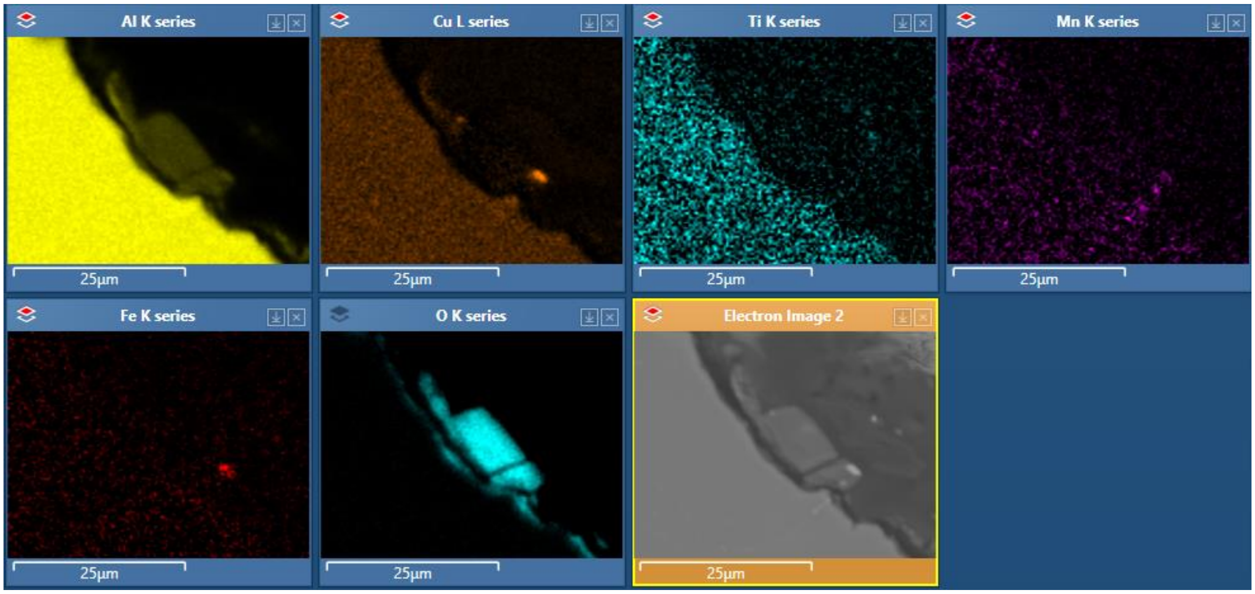

Figure 126: SEM(BSE) and EDS elemental maps of the corrosion surface of Sand Cast with chill sample.

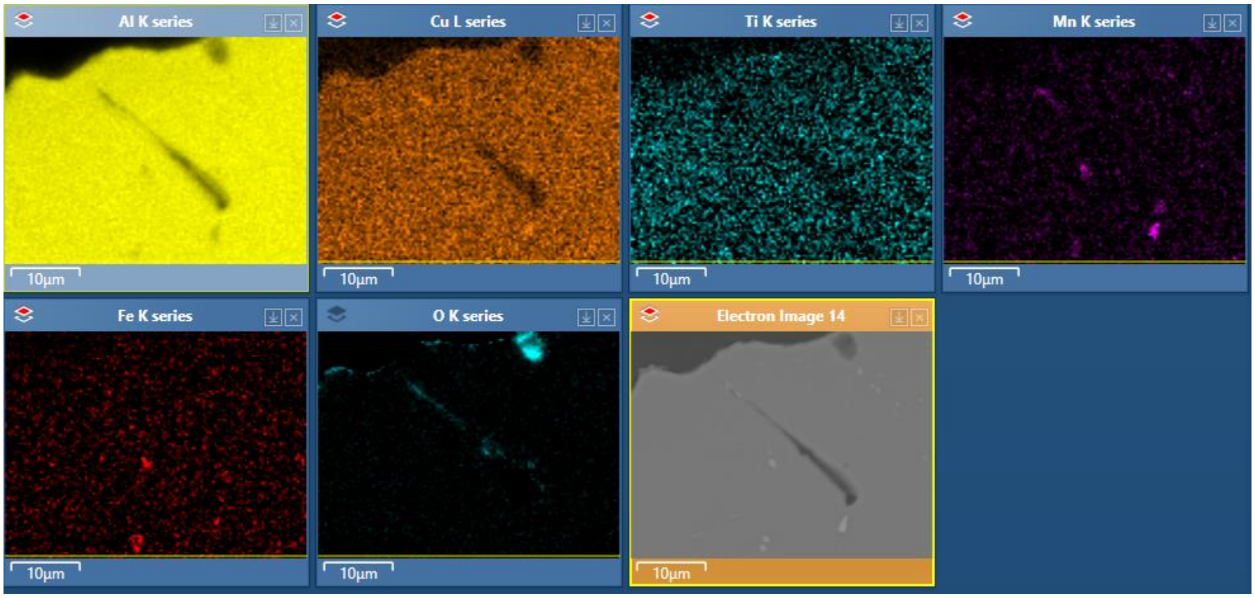

Figure 127: SEM(BSE) and EDS elemental maps of the corrosion surface of Sand Cast with chill sample.

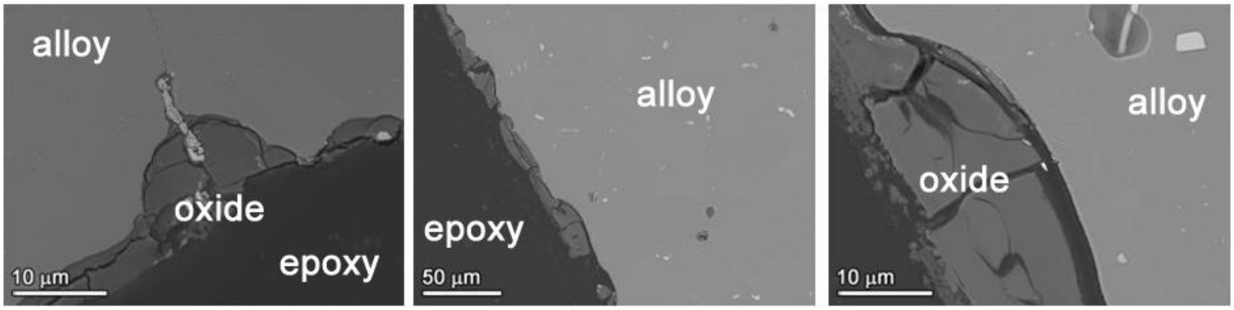

Figure 128: SEM(BSE) micrographs showing general surface corrosion of the Sand Cast with chill nano sample.

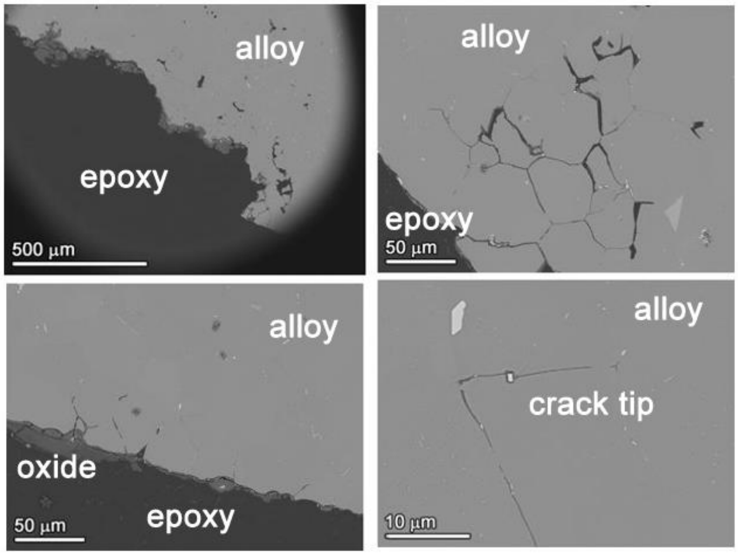

Figure 129: SEM(BSE) micrographs showing SCC cracking of the Sand Cast with chill nano sample.

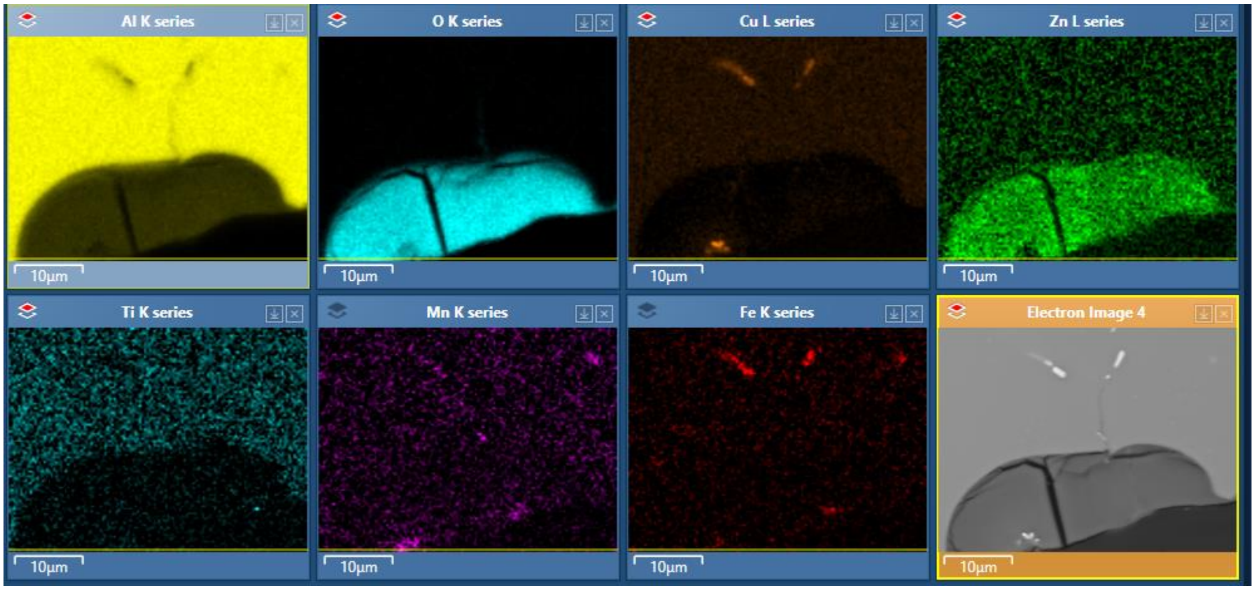

Figure 130: SEM(BSE) and EDS elemental maps of the corrosion surface of Sand Cast with chill nano sample.

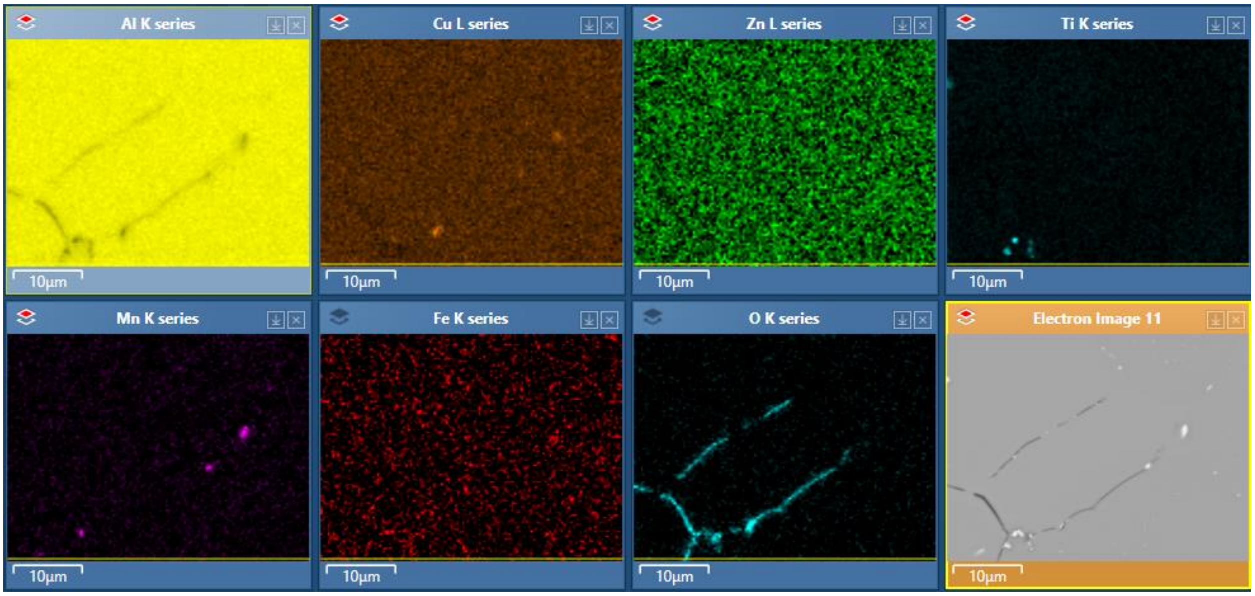

Figure 131: SEM(BSE) and EDS elemental maps of SCC cracks in the Sand Cast with chill nano sample.

7.3.2.10 SEM: Sand Cast No Chill (B, E)

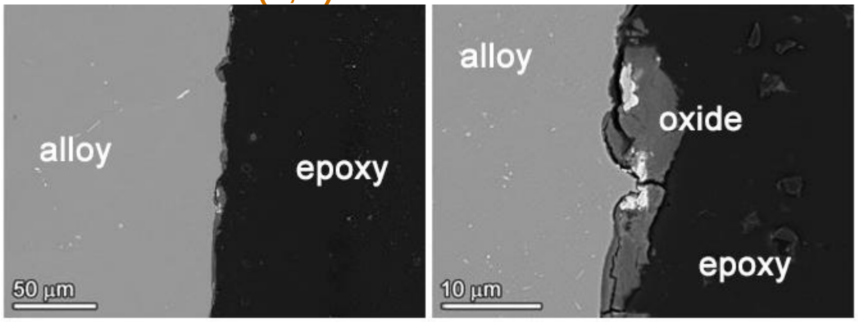

Figure 132: SEM(BSE) micrographs showing general surface corrosion of the Sand Cast no chill sample.

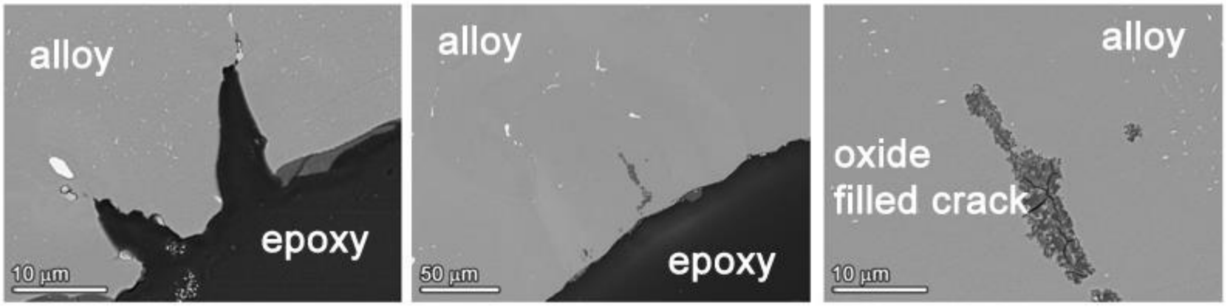

Figure 133: SEM(BSE) micrographs showing SCC cracking of the Sand Cast no chill sample.

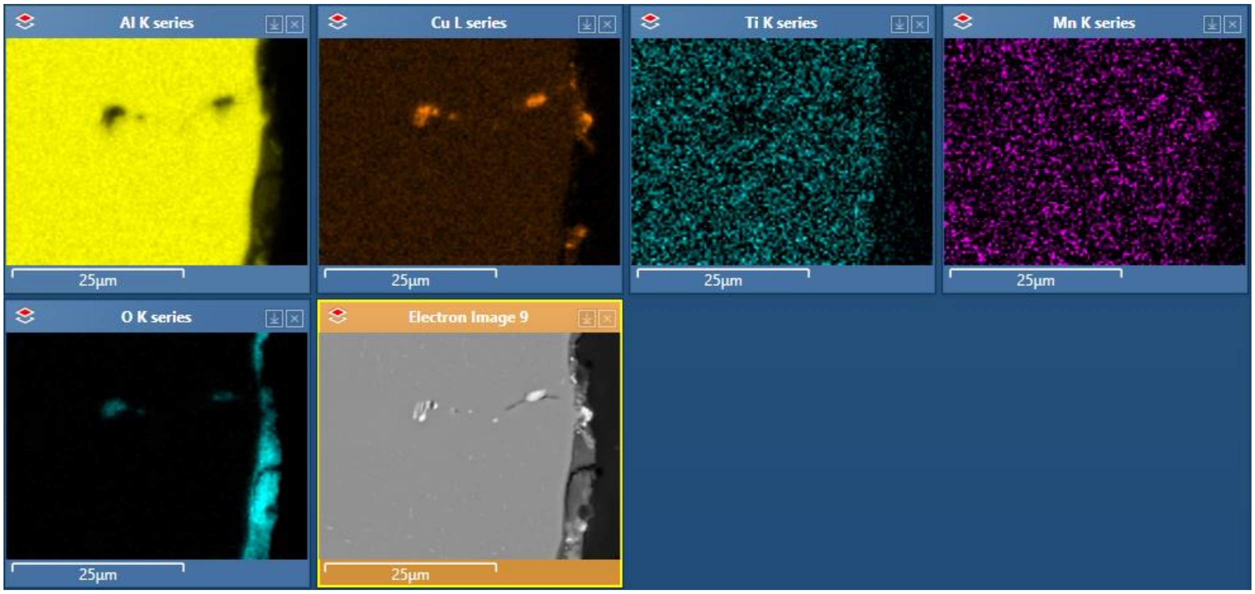

Figure 134: SEM(BSE) and EDS elemental maps of the corrosion surface of Sand Cast no chill sample.

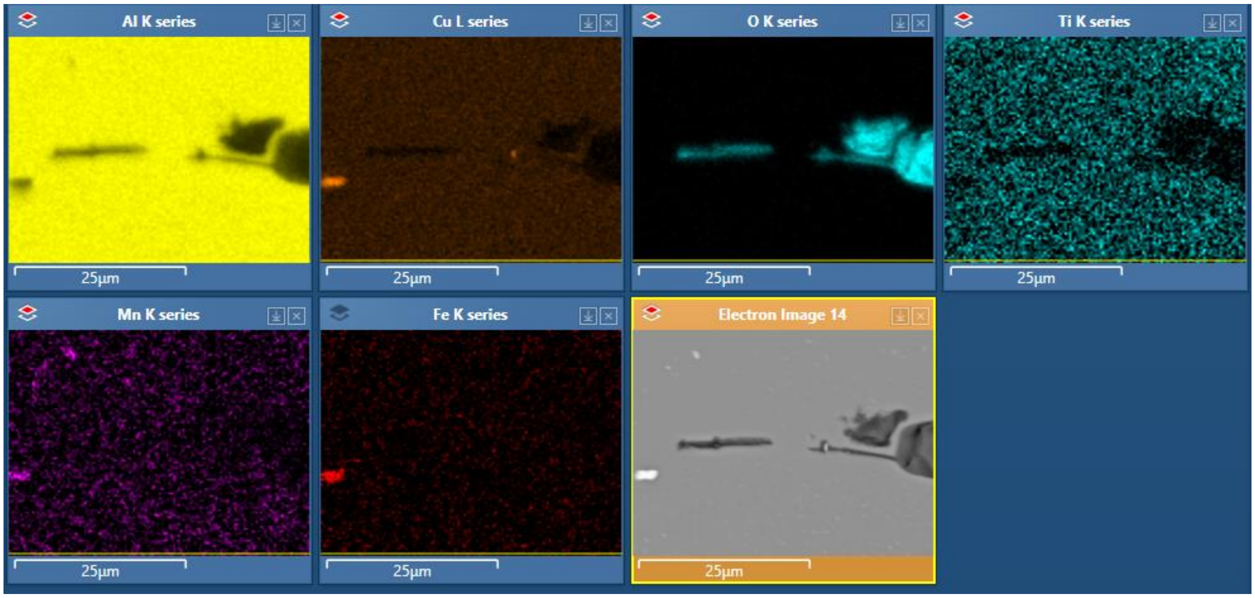

Figure 135: SEM(BSE) and EDS elemental maps of SCC cracks in the Sand Cast no chill sample.

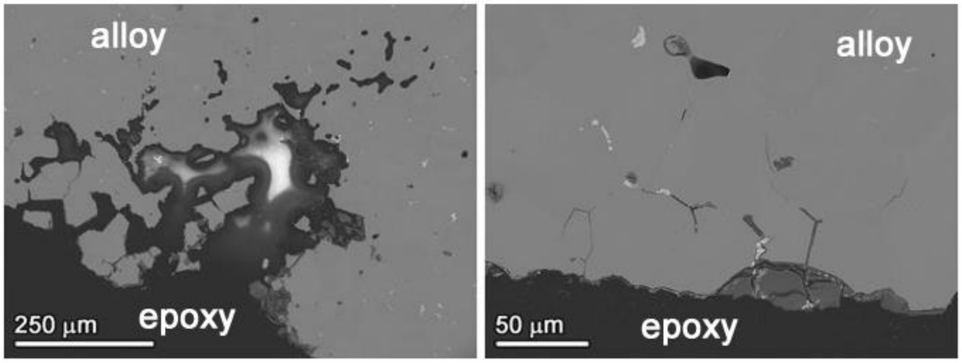

Figure 136: SEM(BSE) micrographs showing general surface corrosion of the Sand Cast no chill/nano sample.

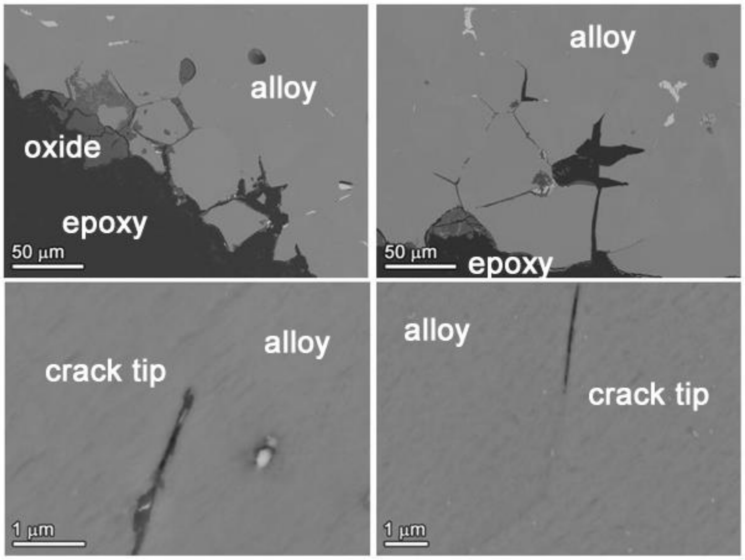

Figure 137: SEM(BSE) micrographs showing SCC cracking in the Sand Cast no chill nano sample.

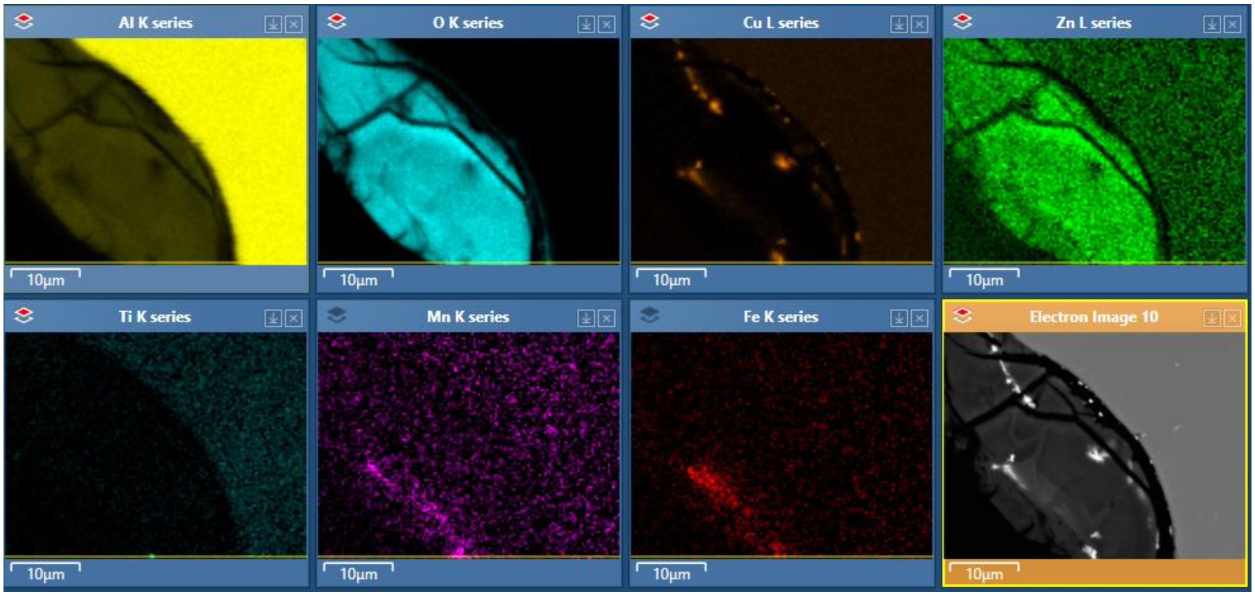

Figure 138: SEM(BSE) and EDS elemental maps of the corrosion surface of Sand Cast no chill nano sample.

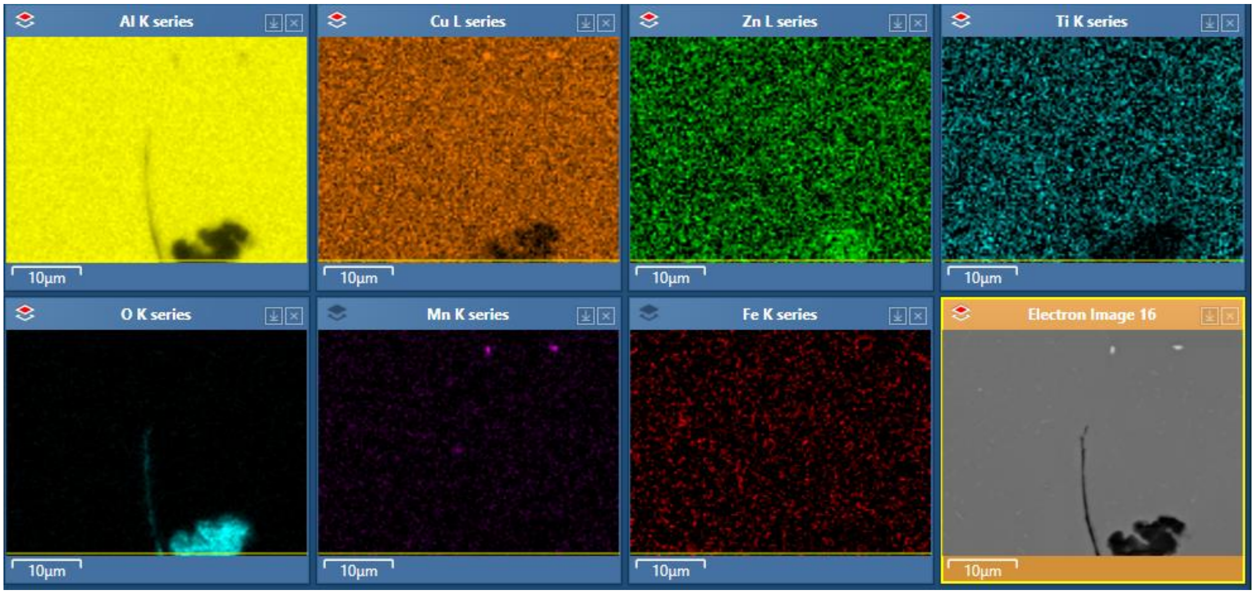

Figure 139: SEM(BSE) and EDS elemental maps of SCC cracking in the Sand Cast no chill nano sample.

8.0 References

[1] I.N. Fridlyander, V.G. Sister, O.E. Grushko, V.V. Berstenev, L.M. Sheveleva, L.A. Ivanova, Aluminum Alloys: Promising Materials in the Automotive Industry, Metal Science and Heat Treatment 44(9) (2002) 365-370.

[2] J. Hirsch, T. Al-Samman, Superior light metals by texture engineering: Optimized aluminum and magnesium alloys for automotive applications, Acta Materialia 61(3) (2013) 818-843.

[3] J.C. Benedyk, 3 - Aluminum alloys for lightweight automotive structures, in: P.K. Mallick (Ed.), Materials, Design and Manufacturing for Lightweight Vehicles, Woodhead Publishing2010, pp. 79-113.

[4] S.K. Das, J.A.S. Green, J.G. Kaufman, The development of recycle-friendly automotive aluminum alloys, JOM 59(11) (2007) 47-51.

[5] Z. Cerovsky, P. Mindl, Hybrid electric cars, combustion engine driven cars and their impact on environment, 2008 International Symposium on Power Electronics, Electrical Drives, Automation and Motion, 2008, pp. 739-743.

[6] L.B. Lave, C.T. Hendrickson, F.C. McMichael, Environmental Implications of Electric Cars, Science 268(5213) (1995) 993-995.

[7] S. Bakker, J. Jacob Trip, Policy options to support the adoption of electric vehicles in the urban environment, Transportation Research Part D: Transport and Environment 25 (2013) 18-23.

[8] J. Cartner, W. Haggard, J. Ong, J. Bumgardner, Stress corrosion cracking of an aluminum alloy used in external fixation devices, Journal of biomedical materials research. Part B, Applied biomaterials 86 (2008) 430-7.

[9] M. Olszta, D.K. Schreiber, L.E. Thomas, S. Bruemmer, High-Resolution Crack Imaging Reveals Degradation Processes in Nuclear Reactor Structural Materials, Advanced Materials & Processes 170 (2012).

[10] S.M. Bruemmer, V.Y. Gertsmann, L.E. Thomas, High-Resolution Comparison of Primary- and Secondary-Side Intergranular Degradation in Alloy 600 Steam Generator Tubing, CORROSION 2000, NACE International, Orlando, Florida, 2000, p. 14.

[11] B.K. Mathan, P.K. Shukla, Stress corrosion cracking (SCC) of copper and copper-based alloys, Stress corrosion cracking: Theory and practice (2011) 409-426.

[12] U.K. Chatterjee, Stress corrosion cracking and component failure: Causes and prevention, Sadhana 20(1) (1995) 165-184.

[13] R. Braun, Environmentally assisted cracking of aluminium alloys, Materialwissenschaft und Werkstofftechnik 38(9) (2007) 674-689.

[14] R. Braun, On the stress corrosion cracking behaviour of 6XXX series aluminium alloys, International Journal of Materials Research 101 (2010) 657-668.

[15] R.N. Parkins, Significance of pits, crevices, and cracks in environment-sensitive crack growth, Materials Science and Technology 1(6) (1985) 480-486.

[16] A.C.U. Rao, V. Vasu, M. Govindaraju, K.V.S. Srinadh, Stress corrosion cracking behaviour of 7xxx aluminum alloys: A literature review, Transactions of Nonferrous Metals Society of China 26(6) (2016) 1447-1471.

[17] D.G. Eskin, L. Katgerman, A Quest for a New Hot Tearing Criterion, Metallurgical and Materials Transactions A 38(7) (2007) 1511-1519.

[18] S. Li, D. Apelian, Hot Tearing of Aluminum Alloys, International Journal of Metalcasting 5(1) (2011) 23-40.

[19] S. Li, D. Apelian, K. Sadayappan, Hot Tearing in Cast Al Alloys: Mechanisms and Process Controls, International Journal of Metalcasting 6(3) (2012) 51-58.

[20] M. Kok, Production and mechanical properties of Al2O3 particle-reinforced 2024 aluminium alloy composites, Journal of Materials Processing Technology 161(3) (2005) 381-387.

[21] J. Lan, Y. Yang, X. Li, Microstructure and microhardness of SiC nanoparticles reinforced magnesium composites fabricated by ultrasonic method, Materials Science and Engineering: A 386(1) (2004) 284-290.
[22] K.B. Nie, X.J. Wang, K.K. Deng, X.S. Hu, K. Wu, Magnesium matrix composite reinforced by nanoparticles – A review, Journal of Magnesium and Alloys (2020).
[23] H.M. Vishwanatha, J. Eravelly, C.S. Kumar, S. Ghosh, Microstructure and Mechanical Properties of Aluminum-Alumina Bulk Nanocomposite Produced by a Novel Two-Step Ultrasonic Casting Technique, Metallurgical and Materials Transactions A 47(11) (2016) 5630-5640.
[24] C.-S. Kim, K. Cho, M.H. Manjili, M. Nezafati, Mechanical performance of particulate-reinforced Al metal-matrix composites (MMCs) and Al metal-matrix nano-composites (MMNCs), Journal of Materials Science 52(23) (2017) 13319-13349.
[25] ASTM, G44-99, Standard Practice for Exposure of Metals and Alloys by Alternate Immersion in Neutral 3.5 % Sodium Chloride Solution, American Society for Testing and Materials, West Conshohocken, PA, 2013.
[26] G.M. Ugiansky, C.E. Johnson, D.S. Thompson, E.H. Gillespie, Slow Strain-Rate Stress Corrosion Testing of Aluminum Alloys, in: G.M. Ugiansky, J.H. Payer (Eds.), ASTM International, West Conshohocken, PA, 1979, pp. 254-265.
[27] R.J. Bucci, Brazill, R.L., Sprowls, D.O., Ponchel, B.M., Bretz, P.E., in: G. V.S. (Ed.) Corrosion Cracking, American Society for Metals, 1986.
[28] ASTM, G139-5, Standard Test Method for Determining Stress-Corrosion Cracking Resistance of Heat-Treatable Aluminum Alloy Products Using Breaking Load Method, American Society for Testing and Materials, West Conshohocken, PA, 2015.
[29] L. Schra, F.F. Groep, The ASCOR Test: A Simple Automated Method for Stress Corrosion Testing of Aluminum Alloys, Journal of Testing and Evaluation 21(1) (1993) 44-50.

Pacific Northwest
National Laboratory

902 Battelle Boulevard
P.O. Box 999
Richland, WA 99354
1-888-375-PNNL (7665)

www.pnnl.gov